Symmetry-Based Double Quantum Recoupling in Solid State NMR

Marina Carravetta

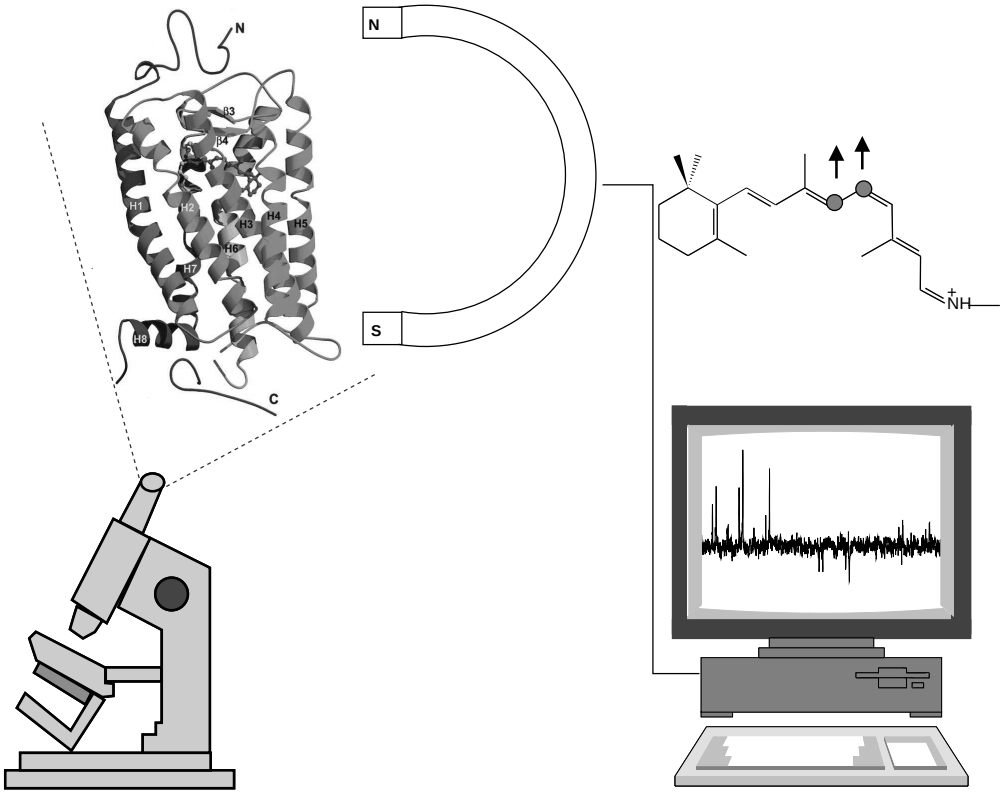

Physical Chemistry Division
Arrhenius Laboratory
Stockholm University
2002

Abstract

This thesis deals with developments and applications of new solid-state NMR experiments on rotating solids, with particular attention to biological systems for which NMR spectroscopy can be an invaluable analysis tool, in conjunction with other techniques. After an introduction to NMR spectroscopy and to some basic experiments, a rigorous description of symmetry-based pulse sequences is given.

The emphasis is put on applications of such sequences for the establishment of an accurate methodology to measure bond lengths between carbon pairs. The technique is demonstrated on model systems of known structure and then applied to the investigation of the chemical bonding in the membrane protein rhodopsin, in which the retinylidene chromophore is selectively labelled for this purpose. The experimental results on the dark state of rhodopsin are compared with the latest theoretical models and a possible mechanism for the conformation change after light absorption is proposed.

A new method for excitation of triple-quantum coherences in multiply-labelled ^{13}C-spin systems under magic angle spinning is presented.

Contents

List of Papers

I Symmetry Principles for the Design of Radiofrequency Pulse Sequences in the Nuclear Magnetic Resonance of Rotating Solids,
M. Carravetta, M. Edén, A. Brinkmann, X. Zhao and M. H. Levitt
Chem. Phys. Lett. **321**, 205 (2000)

II Estimation of Carbon-Carbon Bond Lengths and Medium-Range Internuclear Distances by Solid-State Nuclear Magnetic Resonance
M. Carravetta, M. Edén, O. G. Johannessen, H. Luthman, P. J. E. Verdegem, J. Lugtenburg, A. Sebald and M. H. Levitt
J. Am. Chem. Soc. **123**, 10628 (2001)

III Towards dipolar recoupling in macroscopically oriented samples of membrane proteins rotating at the magic angle
C. Glaubitz, **M. Carravetta**, M. Edén and M. H. Levitt
in "Perspectives on Solid State NMR in Biology",
S. Kiihne and H. J. M. de Groot, eds., Kluwer, Dordrecht, The Netherlands, pages 83-92 (2001).

IV Enhanced Triple-Quantum Excitation in Solid-State MAS NMR
M. Carravetta, J. Schmedt auf der Günne and M. H. Levitt
submitted to *J. Magn. Res.*

V Bond distance measurements on bovine rhodopsin via solid state MAS NMR
M. Carravetta, X. Zhao, S. Kiihne, M. Verhoeven, P. J. E. Verdegem, H. Luthman, P. Bovee-Geurts, J. Lugtenburg, H. J. M. de Groot and M. H. Levitt
in manuscript

Chapter 1

Why Solid-State NMR ?

1.1 What is NMR ?

Nuclear magnetic resonance (NMR) is a spectroscopy that involves the interaction between certain nuclei and magnetic fields. Normally, there is a strong, static magnetic field that splits the energy levels and a modulated magnetic field capable to induce transitions between these levels and generate and observable response. NMR spectroscopy is a powerful technique for investigating structural and dynamical properties of molecules in a variety of physical states. NMR was developed as a technique for studying the magnetic properties of nuclei and their interactions and, as such, was mainly used by physicists. Nonetheless, a widespread of NMR in several fields of science and medicine took place due to the strong correlation between the NMR response and the environment surrounding the nuclei, i.e, the molecular bonds, proximities between specially chosen groups and the lattice.

In the liquid state, NMR is used as a standard tool in the research and industry world and is now well established. The information provided by magnetic resonance in different physical states are quite different and sometimes complementary. In the general case, structure investigation is supported by data coming from other methodologies.

All spectroscopies involve an interaction between electromagnetic radiation and matter. To be effective, the energy of the radiation must match the energy difference between two energy levels within the matter and this is known as the resonance condition. NMR is rather special, since the observed spectra can be manipulated to accentuate some features and suppress others by a proper sequence of low-energy radio-frequency (rf) pulses, a pulse sequence, while the spin system under investigation can often be considered as a perturbation. The structure of the internal energy levels depends upon the physical state and the chemical environment and makes NMR very useful for chemical investigation. In NMR the energy levels can also depend upon the applied rf field, as for the case of spin decoupling.

The form of the NMR Hamiltonian (energy operator) for model systems can often be simplified enough to allow analytical calculation at least up to first order, giving insight in what is happening very clearly. On the other hand, numerical simulation is a invaluable tool for developing new sequences and in many cases it is essential for investigating complex issues. Of course no NMR spectroscopist

Table 1.1: a selection of NMR active nuclei and their properties

Species	Nuclear Spin	Nat. Abundance	γ_I (10^6 rad $T^{-1}s^{-1}$)
^{1}H	1/2	99.985	267.522
^{13}C	1/2	1.1	67.283
^{15}N	1/2	0.366	-27.126
^{31}P	1/2	100	108.3
^{19}F	1/2	100	251.665
^{79}Br	3/2	50.69	67.023
^{2}H	1	0.015	41.063
^{14}N	1	99.634	19.338
^{17}O	5/2	0.038	-36.264

expects to get the final answer just from a simulation. In many real cases there can still be discrepancy between simulations and experiments because the real system is frequently too idealized and oversimplified in the computer analysis, i.e, intermolecular interactions, non-ideal decoupling and relaxation are often neglected. Moreover, the precise structure is often unknown and the assumptions made have to be tested and verified experimentally.

This thesis focuses on certain aspects of NMR applied to solid powders and biomolecules with the aim of structural investigation of biologically relevant samples.

1.2 Nuclear Spin

From classical physics, we are familiar with the concepts of angular momentum and magnetic moment. A charge carrier moving on a loop has both an orbital angular momentum and a magnetic angular momentum associated with it, which originates from its movement. In quantum mechanics there is an additional form of angular momentum, known as spin angular momentum, which is not associated with any motion in real space but it is an intrinsic property of fundamental particles and has no macroscopic counterpart. The existence of the spin was first derived theoretically for electrons: the spin angular momentum comes naturally out from a relativistic treatment of the electrons using the Dirac equation and is at the heart of modern quantum elecrodynamics.[1]

The building blocks of atoms, electrons and nucleons, all possess spin-1/2. The overall nuclear spin results from a combination of all angular momentum contributions from its components. It is quantized and the total spin quantum number can be any integer or half-integer. In NMR, each nucleus is labelled according to its nuclear spin, its natural abundance and its gyromagnetic ratio γ_I, which determines the resonance frequency of the nucleus I in an external static magnetic field. The properties of some common nuclei are listed in Table 1.1 and they are of direct impact for the absolute receptivity of each species. The nuclear structure is rather complex. Even though a satisfactory model for the nucleus has

been developed, the potential function that appears in the nuclear Hamiltonian makes the equations intractable by analytical means and so no closed expression for the nuclear energies is available.[2] This makes the prediction of the ground-state energy levels, and therefore of the nuclear spin, rather challenging in the general case and the deduction *a priori* of the nuclear spin may rely on the knowledge of other nuclear properties. Nevertheless, it is an empirical fact that all nuclei with an even number of protons and neutrons have spin 0 in their ground state. As far as the NMR spectroscopist is concerned, the detailed structure of the nuclear levels can be ignored and all excited states for stable nuclei are so far up in energy that their population is negligible and they can not be reached under usual experimental conditions.

The nuclei of interest in NMR spectroscopy all have at least one unpaired proton and/or one unpaired neutron: in order for a nucleus to be NMR observable, it must have a non-vanishing total spin. As a consequence, different isotopes can differ completely in behavior from the NMR point of view. This is quite a unique feature of NMR, which allows to easily distinguish certain classes of isotopomers, which are hardly distinguishable from the chemical point of view in most cases.

1.3 Overview over Spin Interactions

A typical system of interest in NMR can seldom be described in terms of isolated spins. A spin can interact with electric and magnetic fields.

The only electric interaction involves nuclei with spin greater than 1/2, which possess an intrinsic quadrupole moment. The quadrupole moment can couple with an external electric field gradient, giving rise to the so-called quadrupole interaction. It is therefore dependent upon the symmetry around the nucleus. For quadrupolar nuclei, this is often the dominant interaction.

For spins-1/2, all interactions are magnetic. Spin-1/2 interactions can be divided into two groups: (i) external interaction, i.e., the magnetic field is created from outside the sample; (ii) internal interaction, i.e., the magnetic field originates from the sample itself.

In the first group we have the Zeeman term (Sect. 2.7), which accounts for the splitting between spin energy levels in the presence of a strong, static field, and the interaction with a transverse rf-field (Sect. 2.8), inducing transitions between such levels and generating an observable response. Additionally, each spin experiences a slightly different field depending upon its chemical environment and upon the way that the surrounding electrons are affected by the external magnetic field. This is known as the chemical shift (Sect. 2.9), as it reflects the electronic structure of the molecules.

There are two forms of spin coupling. The scalar coupling (J-coupling, Sect. 2.10) is mediated by the bonding electrons and is usually significant only for nuclei lying a few bonds apart, at least in the case of non-conjugated systems. The direct coupling (dipolar or though-space coupling, Sect. 2.11) is proportional to the product of gyromagnetic ratios of the coupled spins and depends upon their distance as r^{-3}. This term can be very large between nuclei and unpaired electrons, affecting in many ways the spin-system and its relaxation. Heteronuclear spin coupling terms

are important for the understanding of magnetization transfer between different spin species.

The importance of different terms is very much dependent upon the nucleus and the physical state of the sample. In isotropic liquids, quadrupolar and dipolar couplings as well as the anisotropic parts of chemical shifts are averaged out due to fast isotropic molecular motions. In anisotropic systems, such as liquid crystals or solids, molecular motion is much reduced and so the spectrum has a structure which heavily depends upon these interactions and on the allowed molecular motions.

1.4 NMR of Powders

There is a wide interest towards solid-state physics in many fields of research involved with materials as ceramics, glasses, polymers and some biomolecules, to mention a few. Solid-state NMR has always been popular between physicists, while it has spread in the chemistry and biochemistry communities much later than NMR in isotropic or partially oriented phases. This is probably due to the very broad features of solid-state spectra of non-crystalline samples, which makes the data interpretation a challenging task in many cases.

In NMR, the solid under investigation is often not a perfect crystal, but rather a powder or a glass and as such is not suitable for diffraction studies, where the current technology requires well shaped and medium sized crystals. On the one hand, solid-state NMR does not suffer from this limitation, being quite flexible for the structural analysis of powder samples. On the other hand, many NMR experiments require isotopic labelling and sometimes the production of several samples, labelled in different positions, while diffraction studies can provide the entire information from one good crystal.

A crystalline powder is made up of millions of crystallites randomly oriented. In such a system, the anisotropic part of the spin interactions (described by a second-rank tensor) does not vanish and the spectrum arising from each crystallite depends upon its own orientation with respect to the surroundings and the external field.[3,4]

The overall spectrum is the sum of all these contributions and is generally very broad, not easy to analyze and computationally heavy to simulate. NMR is intrinsically a low-sensitivity technique, in part because the acquired NMR signal is proportional to the small population difference between energy levels, corresponding to a small equilibrium magnetization (see Sect. 2.7). To compensate for this limitation, NMR samples need to be much more massive than samples used in other forms of spectroscopy in which the energy levels involved in the transitions are several order of magnitude bigger, and so correspond to a greater population difference. This limit is even more evident in solid-state NMR, where the signal coming from different crystallites is spread over a wide spectral range, due to the anisotropic nature of spin interactions.

In many ways, some biological solids are rather similar to powder samples and most techniques developed for powders can be extended to them. The lack of sensitivity in NMR is a serious limitation for biological samples, given that the

portion of system which is to be investigated by NMR can be a tiny fraction of the available sample, reducing the observed spin-system to just a fraction of a μmole. As a consequence, much effort has been put into developing methods to increase the resolution and the sensitivity in NMR.

1.5 Sensitivity and Resolution Enhancement

In anisotropic phases, an increase in resolution can be achieved by suppressing the orientation dependence of spin interactions, as well as the interactions between spins. In this way, every spin with a particular local environment would ideally give an NMR signal at its isotropic chemical shift, in analogy with a spin-decoupled liquid-state spectrum.

A uniform rotation of the solid sample about an axis at the magic angle to the field, $\beta_m = \tan^{-1}\sqrt{2}$, can be shown to remove the anisotropic effects due to second-rank tensors if the spinning frequency exceeds in magnitude all the anisotropic interactions. This is known as Magic-Angle-Spinning (MAS),[5] as discussed in Sect 2.13.1. In reality, even state-of-the-art technology does not allow this condition to be completely fulfilled, but a considerable resolution enhancement is nevertheless observed. Other forms of spatial averaging have been exploited in the case of quadrupolar nuclei in order to increase the resolution, as discussed in Sect. 2.12.

While MAS is the result of a purely spatial averaging process, the spin Hamiltonian can also be manipulated to improve the resolution by using pulse sequences which, for instance, decouple spins (see Sect 2.13.3) and which enhance the signal by magnetization transfer between different spin species, often using the cross-polarization (CP) method (see Sect 2.13.5).

It is important to stress that the sample rotation and the pulse sequences must be analysed together since in some cases they interfere with each other.

1.6 Recoupling of Spin Interactions

A static spectrum is rich in information about the system under investigation but such information is very difficult to extract due to the broad features of the spectrum. On the other hand, fast MAS has an averaging effect over the anisotropic interactions and a great deal of structural information is lost. The goal of many solid-state NMR experiments is to re-introduce some spin interactions selectively, while averaging out undesired terms.[6–12] This is called recoupling. Chapter 3 describes the basis for developing symmetric, rotor-synchronized pulse sequences which achieve this task to a first approximation.

One important application of recoupling techniques is homonuclear dipolar recoupling. For a sample containing a pair of well-chosen, labelled, rare nuclei, it is possible to get detailed information about the spin pair and its surroundings while filtering out the signal from natural abundance nuclei of the same species in the rest of the sample, using a so-called double-quantum (DQ) filter.[13] In the case of spins-1/2, the concept of spin coherence is connected to the existence of a

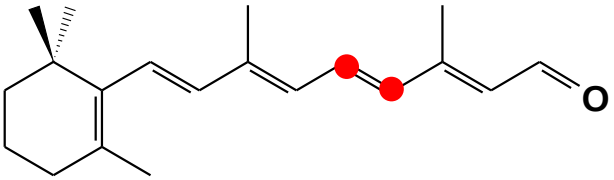

Figure 1.1: [11,12-$^{13}C_2$]-all-*E*-retinal. The label positions are marked by a solid circle

correlated state between a certain set of spins. In very loose terms, the coherence order reflects directly the number and state of the correlated spins. For instance, a DQ coherence can be made up of two spins such that each individual spin has a random orientation with respect to the external field, but it has a preferential orientation with respect to the other spin participating in the DQ state. A more mathematical definition of the coherence order is given in Sect. 2.14.1. This feature is quite important when dealing with biological samples. A demonstration of this idea is given in Fig. 1.2 for a simple spin system, where the cross-polarization[14,15] spectrum of [11,12-$^{13}C_2$]-all-*E*-retinal, diluted in a 10-fold excess of non enriched all-*E*-retinal (Fig. 1.1), is compared with the corresponding DQ filtered signal. Another application of recoupling sequences is given in Fig. 1.3. In this case the dipole-dipole interaction between the labelled nuclei in [11,12-$^{13}C_2$]-all-*E*-retinal is recoupled and the observed signals are modulated with a frequency which can be related to the strength of the dipole-dipole coupling constant and, hence, to the internuclear distance. The determination of ^{13}C-^{13}C bond length is one of the key subjects of this thesis.

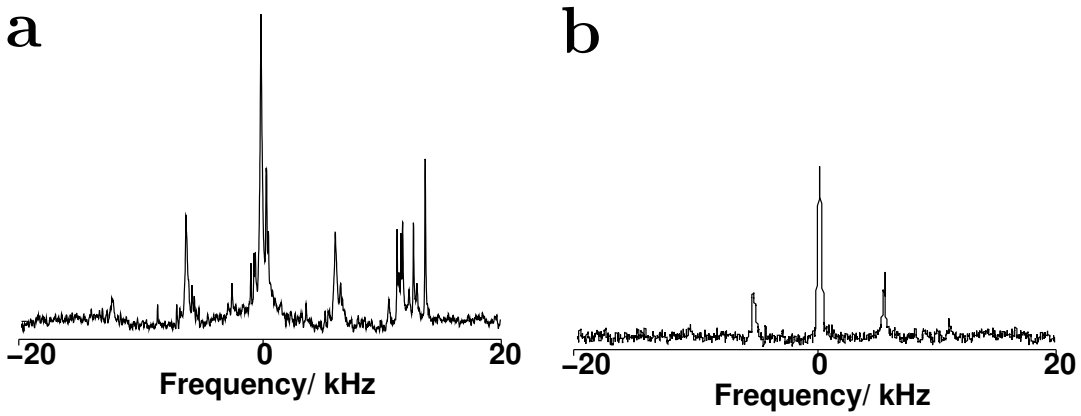

Figure 1.2: (a) ^{13}C spectrum of 10%-[11,12-$^{13}C_2$]-all-*E*-retinal at 9.4 T and a spinning frequency of $\omega_r/2\pi$=5.5 kHz. (b) Double quantum filtered ^{13}C spectrum using the pulse sequence $R14_2^6$ (see Paper II). Only the peaks from the $^{13}C_2$ pairs are visible.

1.7 NMR in Biology

The techniques briefly described in the previous paragraphs are essential tools for working with many biologically-relevant samples in the solid-state. A thorough

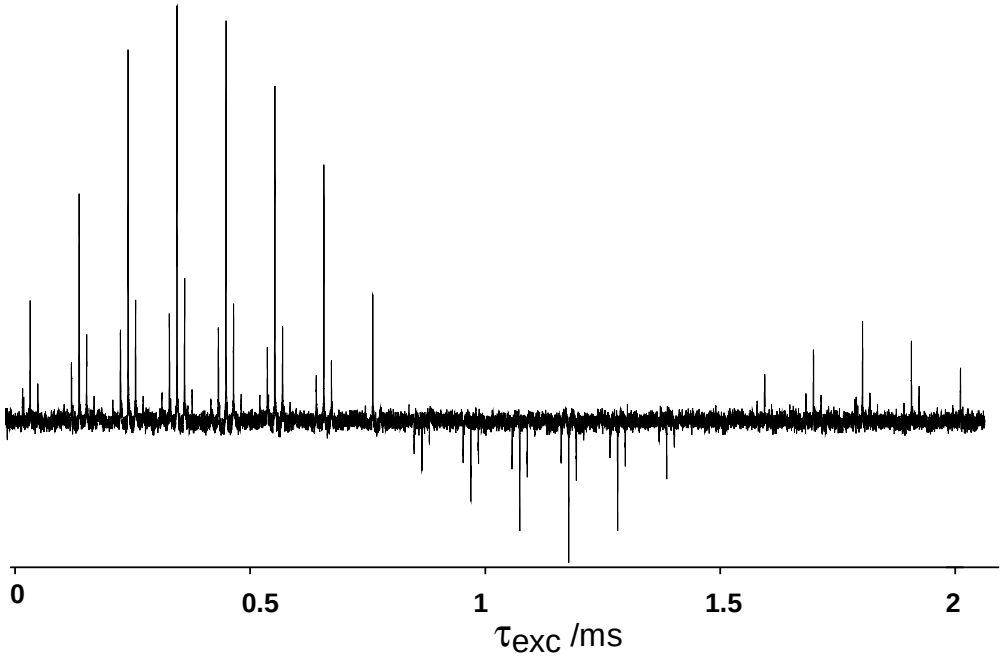

Figure 1.3: ^{13}C DQF spectra of [11,12-$^{13}C_2$]-all-*E*-retinal at a static magnetic field of 9.4 T and $\omega_r/2\pi$=5.5 kHz as a function of DQ excitation time. The oscillation reveals the dipole-dipole interaction between the ^{13}C spins.

description of spin interactions will be given in the following chapter. For the time being it suffices to stress that there is a noticeable wealth of information within different spin interactions, in terms of the electronic environment (CS), the geometry (DD) and orientation (anisotropic terms) of key fragments.

Some more insight into how NMR can be of help for studying biological system can be found in recent reviews.[16,16,17] As stressed already, the information provided by NMR is related to the physical state of the system and by the mobility of the molecules under investigation. Liquid-state NMR is widespread as a tool for general investigation of structure and conformation of rather big systems (up to approximately 30 kDa) with relatively low resolution, normally of the order of Ångström (Å). Nowadays solid-state NMR is a competitive technique for studying macromolecules, but it also provides localized information with higher precision and this aspect will be emphasized in what follows.

The structural information obtained from liquid-state NMR studies are often obtained from relaxation studies, for which the dipolar interaction is of great importance and lead to distances and relative orientations (i.e., giving insight into the protein secondary structure). The presence of paramagnetic centers within the biosystem can increase the range of the techniques up to several tens of Å. Therefore, liquid-state techniques can give a general overview about the molecular structure, without defining clearly the details. The data obtained from NMR are used together with simulations to get a series of optimized structures and the set of structures with energy lower than a certain threshold is the final result, but it is not easy to specify exactly the precision of these data. Roughly speaking, the

best structures are superimposed and the structural variations provide a measure of the uncertainty in the geometry.

NMR in anisotropic phases can provide geometrical information in a more direct way. The anisotropy can be induced by dissolving the molecules of interest in an orienting medium, like liquid crystals or micelles, and the extent of orientation determines the range of information that can be extracted. Many recent developments rely on the presence of very weak orienting media which allow for a small portion of the residual dipolar couplings to be visible without degrading the spectral resolution: this simplifies the spectral analysis by just allowing the largest anisotropic interactions to be clearly visible and therefore reducing drastically the number of parameters to be extracted.[18,19]

When applied to abundant nuclei, i.e., ^{31}P, ^{19}F or ^{1}H, solid state NMR can give insight into structure and proximities without much synthetic effort. As such, it is an invaluable tool for materials science.

On the other hand, few examples of complete structural determination by solid-state NMR of medium-sized organic samples (i.e., small peptides and so on) are so far available using fully labelled samples (for instance, Refs. 20–22). Until recently, such studies have required the synthesis of many different samples, specifically labelled in key positions with ^{13}C or ^{15}N. For instance, C^{α} chemical shifts and ^{15}N-^{1}H couplings/^{15}N chemical shifts are of invaluable importance in proteins since they can be related to the backbone secondary structure.[23,24]

A completely different philosophy is behind other types of NMR studies, in which solid-state NMR of biological molecules is used to answer very specific questions about the system, while the less-detailed background knowledge is obtained from other methods. A good example of this is the investigation of chemical bonding and atomic short-range interaction, for instance Van der Walls interactions, hydrogen bonding, bond-length determinations, torsion angle measurements and refinement of the hydrogen positions (which is only reliably provided by neutron diffraction).

In the context of this thesis, we will focus on one particular class of biomolecules, the trans-membrane G protein coupled receptors, for which solid-state NMR can be of great use. After a general description of the functionality of these proteins, we will shift our attention to one specimen of this class, rhodopsin, and demonstrate how solid state NMR can aid the understanding of its function.

Chapter 2

The Tools of Solid State NMR

To understand NMR in rotating solids, some introductory concepts about quantum mechanics and angular momentum theory are necessary, together with some other mathematical tools to treat the spin system evolution under general space-spin rotations. More information about the operator formalism and the Dirac notation are to be found in Appendix A.2.

2.1 Definition of Angular Momentum Operators

In classical physics, angular momentum is associated with the rotational properties of a system and we want to understand the role of the angular momentum operator in quantum mechanics in this respect.

Let $R(\mathbf{n}, \theta)$ be a rotation operator by an angle θ about some direction $\mathbf{n}$ in the three-dimensional space. When acting on the wavefunction ψ it will rotate it into a new state $\psi^{'}$, i.e.,

$$\psi^{'} = R(\mathbf{n}, \theta)\psi \tag{2.1}$$

The rotation operator is unitary by definition, so it can be expressed as

$$R(\mathbf{n}, \theta) = e^{-i\, S(\mathbf{n},\theta)} \tag{2.2}$$

without loss of generality, with the only constraint that $S(\mathbf{n}, \theta)$ is Hermitian. Let $\mathbf{J}$ be the vector operator associated with the angular momentum and let J_x, J_y J_z be its components along the Cartesian axes. It can be shown[25] that $S(\mathbf{n}, \theta)$ is the rotation angle times the angular momentum operator component in the direction of the rotation axis $\mathbf{n}$, $S(\mathbf{n}, \theta) = \theta(\mathbf{n} \cdot \mathbf{J})$, or

$$R(\mathbf{n}, \theta) = e^{-i\theta(\mathbf{n}\cdot\mathbf{J})} \tag{2.3}$$

As known from standard quantum mechanics, the angular momentum of a system is quantized. J^2 commutes with each individual component, therefore a good set of quantum numbers for the system is the set of eigenvalues of J^2 and *one* of the components, which is taken to be J_z by convention. The common set of eigenfunctions of J^2 and J_z constitutes a complete basis set. The angular

momentum components do not commute with each other but are related by the relationship

$$[J_i, J_j] = i\epsilon_{ijk} J_k \tag{2.4}$$
$$\left[J^2, J_i\right] = 0 \tag{2.5}$$

where ϵ_{ijk} is the totally asymmetric tensor. Operators following these commutation rules are known as Casimir operators.[26,27] It is possible to obtain the complete set of eigenvalues for the angular momentum operators (App. A.3) by exploiting the above definitions and commutation rules. Let the eigenvalues of J^2 and J_z be j and m respectively and $|j,m\rangle$ be the corresponding eigenfunctions in Dirac's notation (see appendix A.2), then

$$J^2 |j,m\rangle = \hbar^2 \, j(j+1) \; |j,m\rangle \tag{2.6}$$
$$J_z |j,m\rangle = \hbar \, m \; |j,m\rangle \tag{2.7}$$

The eigenvalue derivation does not rely on the assumption that j is an integer and so this result holds for both orbital and spin angular momentum. Let us define rising and lowering operators as

$$J_+ = J_x + iJ_y \tag{2.8}$$
$$J_- = J_x - iJ_y \tag{2.9}$$

The eigenvalue problem for the rising and lowering operator has the solution

$$J_\pm |j,m\rangle = \hbar\sqrt{j(j+1) - m(m\pm 1)} \, |j, m\pm 1\rangle \tag{2.10}$$

The eigenbasis $|j,m\rangle$ is useful to give a matrix representation of operators relevant in NMR. For integer j values, the eigenfunction set is given by the so-called spherical harmonics,

$$Y_{lm}(\theta,\phi) = P_l(\cos\theta) \, e^{im\phi} \tag{2.11}$$

where P_l are the Legendre polynomials.[28] The symmetry of the spherical harmonics reflects the symmetry of atomic orbitals and represents faithfully the transformation properties of spherical tensors.

2.2 Wigner Matrices and Euler Angles

Many different ways to describe general rotations are available. In NMR it is convenient to decompose a rotation about $R(\mathbf{n},\theta)$ about an arbitrary axis $\mathbf{n}$ by θ into a set of three rotations. If we label the starting reference frame axes as $\{x,y,z\}$ and put primes on the axes to mark rotated frames, then the rotation $R(\mathbf{n},\theta)$ can be decomposed as

- rotation about the z-axis by an angle α
- rotation about the y'-axis by an angle β

- rotation about the z''-axis by an angle γ

and each rotation is performed in a different frame than the others. The same effect can be achieved by performing all rotation in the initial frame in inverted order, i.e.,

$$\begin{aligned} \exp\{-i\theta(\mathbf{n}\cdot\mathbf{J})\} &= \exp\{-i\gamma J_{z''}\}\,\exp\{-i\beta J_{y'}\}\,\exp\{-i\alpha J_z\} && (2.12)\\ &= \exp\{-i\alpha J_z\}\,\exp\{-i\beta J_y\}\,\exp\{-i\gamma J_z\} && (2.13)\end{aligned}$$

The set of angles $\Omega = \{\alpha, \beta, \gamma\}$ is known as Euler angles. The matrix representation of rotation operators associated with it is expressed in the spherical basis of the angular momentum, $\{|j, m\rangle\}$, and is known as the Wigner matrix

$$\begin{aligned} D^j_{m'm}(\Omega) &= \left\langle jm' \left| e^{-i\alpha J_z}\, e^{-i\beta J_y}\, e^{-i\gamma J_z} \right| jm \right\rangle = e^{-im'\alpha} \left\langle jm' \left| e^{-i\beta J_y} \right| jm \right\rangle e^{-im\gamma} \\ &= e^{-im'\alpha}\, d^j_{m'm}(\beta)\, e^{-im\gamma} && (2.14)\end{aligned}$$

where $d^j_{m'm}(\beta)$ is the reduced Wigner matrix element. The size of the matrix depends on the j value as $(2j+1)$. The reduced matrix elements for $j = 0, 1, 2$ and some useful properties of the Wigner matrices are given in Appendix B.1.

2.3 Tensors and Spherical Tensors

The physical properties of a system can be described in terms of entities of different dimensionality. For instance, the electric charge is a scalar quantity, because it is orientation independent and it can be fully described by a number. The magnetic field generated in the vacuum by a moving charge can not be fully defined by a number, in fact a full description requires the knowledge of its magnitude *and* direction. The magnetic field is a three-dimensional vector quantity.

There is a third class of object, tensors, which manifest different behavior in different directions and which can be fully represented in a matrix form. A tensor is defined by its transformation properties under a transformation of the coordinate system (i.e., rotation and inversion). The magnetic susceptibility, conductivity, compressibility belong to the class of tensorial properties, just to mention a few.

In general, all three quantities can be considered as tensor of different rank. The rank of a tensor is given by the number of indices of the tensor, so a rank-0 tensor is a scalar, a rank-1 tensor is a vector and a rank-2 tensor is a matrix. Tensors of order higher than 2 can be defined as well, but they are not needed in the context of this thesis.

In the description of NMR interactions, it is common to start from a description of the physical property in tensor form within a Cartesian frame. Even though it is easy to visualize the meaning of different terms clearly in this basis, it is not an ideal choice from the mathematical point of view since the Cartesian representation is reducible.[25] A Cartesian tensor T contains nine real components and it can be decomposed into three irreducible tensors: a rank-0 tensor, proportional to the trace of T, an asymmetric rank-1 tensor and a symmetric rank-2 tensor. Even though such decomposition is possible without any basis change, it is more

convenient to use the spherical coordinate representation in order to obtain quantities which transform simply under rotation. The matrix expressing the basis transformation between Cartesian and spherical basis is conventionally denoted $\mathbb{T}$ (App. B.2) and tensors of ranks 1 and 2 transform as

$$A^{(1)}_{\text{sph}} = A^{(1)\dagger}_{\text{Cart}}\,\mathbb{T} \tag{2.15}$$

$$A^{(2)}_{\text{sph}} = \mathbb{T}^{\dagger} A^{(2)}_{\text{Cart}}\,\mathbb{T} \tag{2.16}$$

In its irreducible representation, a tensor of rank J possesses $(2\,J+1)$ components which transform under the $(2\,J+1)$-dimensional representation of the rotation as

$$R(\mathbf{n},\theta)\,T_{JM}R(\mathbf{n},\theta)^{-1} = \sum_{M'} D^{J}_{MM'}(\Omega)T_{JM'} \tag{2.17}$$

or in other words, an irreducible spherical tensor operator (ISTO) is defined by its transformation under a rotation of the reference frame from F to $F^{'}$ as

$$[T_{JM}]^{F'} = \sum_{M'} D^{J}_{MM'}(\Omega_{FF'})\,[T_{JM'}]^{F} \tag{2.18}$$

where the tensors' components in a specified frame are indicated witin square brackets. In its principal axis frame (PAS), i.e., in the frame that makes the symmetric part of Cartesian tensor diagonal, a rank-2 ISTO can be expressed as

$$\left\langle T^{(2)}\right| = \sqrt{\frac{3}{2}}(T^{P}_{zz} - T_{iso})\left(-\frac{1}{\sqrt{6}}\eta, 0, 1, 0, -\frac{1}{\sqrt{6}}\eta\right) \tag{2.19}$$

where we define

$$T_{iso} = \frac{1}{3}\sum_{i} T_{ii} = \frac{1}{3}\text{Tr}(T) \tag{2.20}$$

$$\eta = \frac{T^{P}_{xx} - T^{P}_{yy}}{T^{P}_{zz} - T_{iso}} \tag{2.21}$$

This formulae will be used in what follows in the context of spin interactions. More informations on spherical tensors are in Appendix B.2 and in Ref 25.

2.4 Secular Approximation

Before discussing the spin interactions in details, it is worth introducing the secular, or high-field, approximation. The Zeeman Hamiltonian is several order of magnitude bigger than all other spin interactions in fields of a few Tesla (with the exclusion of the quadrupolar interaction, in some cases). As a consequence, it is possible to treat the spin interactions as a perturbation of the Zeeman term and calculate the new energy levels by considering only the first-order time-independent perturbation theory correction.[28] If we decompose the interaction Hamiltonian $\mathcal{H}_Q$ into two terms,

$$\mathcal{H}_Q = \mathcal{H}^{\text{com}}_Q + \mathcal{H}^{\text{ncom}}_Q \tag{2.22}$$

Table 2.1: Classification of interactions in terms of their ranks in terms of spin (λ), space (l) and field ($\mathbf{B}$).

Interaction	$\mathcal{H}_Q$	$[A_{l0}]\, T^{\text{int}}_{\lambda\mu}$	λ	l	$\mathbf{B}$
Zeeman	$\mathcal{H}^j_Z$	$\omega^j_0 T^j_{10}$	1	0	1
RF-Field	$\mathcal{H}_{\text{rf}}(t)$	$\omega^S_{\text{nut}}(t) R_z(\phi) I_x R_z(-\phi)$	1	0	1
Spin-Spin	$\mathcal{H}^{ij}_{J,iso}$	$2\pi J_{ij} T^{ij}_{00}$	0	0	0
	$\mathcal{H}^{ij}_{anti}$	$\left\langle A^{(1)}_{ij} \middle\vert T^{(1)}_{ij} \right\rangle$	1	1	0
	$\mathcal{H}^{ij}_{aniso}$	$\sqrt{6} b_{ij}\, d^2_{00}(\beta^{ij}_{PL})\, T^{ij}_{20} + \mathcal{H}^{ij}_{J,aniso}$	2	2	0
Chemical	$\mathcal{H}^{\sigma,iso}_j$	$-\omega^j_0\, \delta^j_{\text{iso}}\, T^j_{10}$	1	0	1
Shift	$\mathcal{H}^j_{CS,anti}$	0	1	1	1
	$\mathcal{H}^j_{CSA}$	$\sum_m \left[A^{CSA}_{2m}\right]^P D^2_{m0}\left(\Omega^j_{PL}\right) I_{jz}$	1	2	1

such that

$$\left[\mathcal{H}^{\text{com}}_Q, \mathcal{H}_{\text{Zeeman}}\right] = 0 \tag{2.23}$$

$$\left[\mathcal{H}^{\text{ncom}}_Q, \mathcal{H}_{\text{Zeeman}}\right] \neq 0 \tag{2.24}$$

only the portion of which commutes with the Zeeman Hamiltonian need to be considered to calculate the perturbed energy levels and therefore determines the positions of the resonances in the spectrum. Given an interaction described by a tensor $\mathbb{A}$, this corresponds to taking just the tensor component in the direction of the Zeeman field, i.e., $\mathbb{A}_{zz}$. In terms of spherical tensors, this corresponds to the selection of all spin operators of the form $T_{\lambda 0}$. The non-commuting term affects the perturbed eigenfunctions, higher order energy corrections and the relaxation of the system,[4] thereby the lineshape.

2.5 Spin Interactions

Now all the tools for a detailed treatment of spin interactions are available. Each interaction is first compared to the corresponding classical interaction using the correspondence principle,[28] when possible, then the Hamiltonian is described in terms of spherical tensors and referred to its own principal axis frame. A list of the spin interactions is given in Table 2.1, where the emphasis is on their different space-spin-field ranks.

The NMR Hamiltonian for any interaction Q can always be expressed as a product of a tensor A^Q with two operators, one is a spin vector operator $\mathbf{I}$ while the other, labelled $\mathbf{R}$ here, can either be a field vector or a spin vector operator,[3,29,30]

i.e.,

$$\mathcal{H}_Q = c_Q \, \mathbf{I}^\dagger \, A^Q \, \mathbf{R} = \langle \mathbf{I} | \, A^Q \, | \mathbf{R} \rangle \tag{2.25}$$

where the term c_Q depends on the interaction under consideration. The equation above can be rewritten by condensing the $\mathbf{I}$ and $\mathbf{R}$ operators into a new field-spin tensor T (see Ref. 3 for more details)

$$\begin{aligned} \mathcal{H}_Q &= c_Q \sum_l \left\langle A^{Q(l)} | T^{Q(l)} \right\rangle \\ &= c_Q \sum_l \sum_{m=-l}^{l} (-1)^{l-m} \left[A^Q_{lm} \right] \left[T^Q_{l-m} \right] \end{aligned} \tag{2.26}$$

by expanding the scalar product between the two tensors[31] in terms of the tensor components. This separates the spatial part of the Hamiltonian (A^Q tensor) and the field-spin part (T tensor). The concept of a field-spin tensor is very convenient for calculation, but it is often easier to understand the physics behind the spin interactions by sepatating the field term from the spin term. In those cases, the tensor for spin j will be explitcitly labelled as T^j, while the field component will be indicated as B (see Sects. 2.7 and 2.8). For a sample rotating with spinning frequency ω_r (in angular units), the total spin Hamiltonian is denoted

$$\mathcal{H}_{Tot} = \sum_Q \sum_{\lambda,\mu,l,m} \mathcal{H}^Q_{lm\lambda\mu} e^{im\omega_r t} \tag{2.27}$$

In the high-field approximation

$$\mathcal{H}_Q = c_Q \sum_l [A^Q_{l0}] \, [T^Q_{l0}] \tag{2.28}$$

2.6 Reference Frame Transformations

It is always possible to write the NMR Hamiltonian as in Eq. 2.28 as long as *both* tensors are referred to the same reference frame. The discussion of many NMR properties relies on transforming the overall Hamiltonian, or portions of it, between different reference frames. It is useful to list some of the common reference frames relevant for describing the solid-state NMR Hamiltonian: the laboratory frame (L), the Molecular frame (M), the Rotor frame (R) and Principal axis frame (PAS, or P).[32] The relationships between them are illustrated in Fig. 2.1.

It is very common, but soon cumbersome, to use the notation defined above for tensors. In what follow we will drop the square brackets when dealing with tensors in the L frame, all tensor components will be assumed as components of a Bra, if not otherwise specified and in all scalar products defining the spin interactions the first spin or field tensor is intended to be a Bra and the second a Ket.

In practice, it is convenient to express the spin part of the interaction in the frame L (so we write $[T_{\lambda\mu}]^{(L)}$ as $T_{\lambda\mu}$) and the spatial part in a different frame,

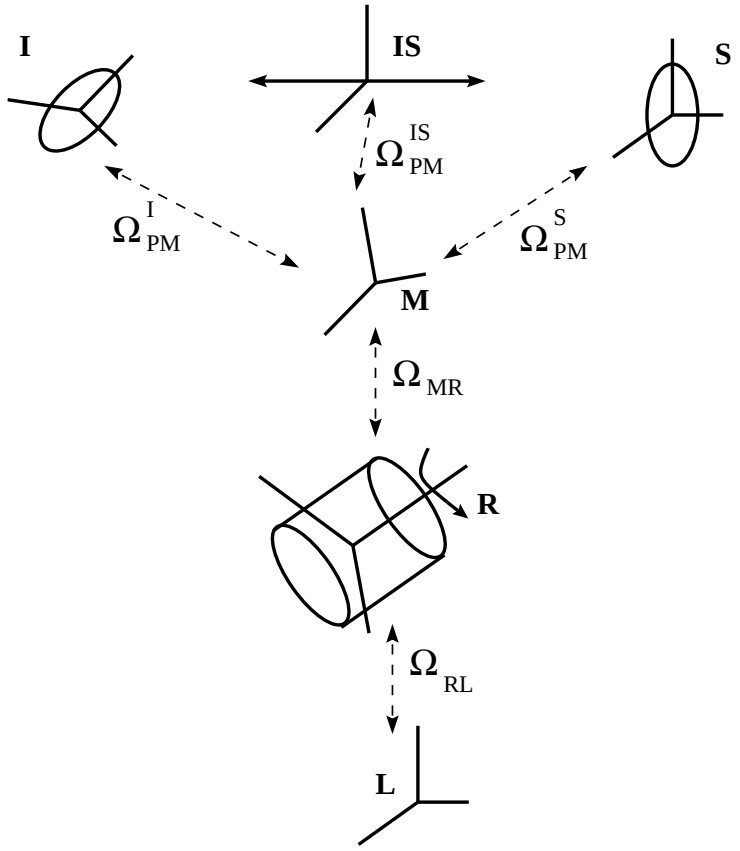

Figure 2.1: Important reference frames and their relationship. The frame L is the laboratory frame. The z axes of the rotor frame and the laboratory frame are at the magic-angle with respect to each other and rotates about z^R with a frequency matching the spinning frequency. R and L are related by the Euler angles Ω_{RL}. The molecular frame is expressed with respect to the rotor frame by Ω_{MR}. For each spin interaction we can define a different principal axis frame with respect to the molecular frame, i.e., Ω^I_{PM}, Ω^S_{PM} and Ω^{IS}_{PM} refer respectively to the orientation of two CSA tensors and the dipolar tensor.

i.e., R or P. Such transformation can be easily performed in terms of Wigner matrices,[25,33] as

$$\left\langle A^{(J)}\right|^{F_2} = \left\langle A^{(J)}\right|^{F_1} D^J\left(\Omega_{F_1F_2}\right) \tag{2.29}$$

where $\Omega_{F_1F_2}$ contains the Euler angles $\Omega_{F_1F_2} = (\alpha_{F_1F_2}, \beta_{F_1F_2}, \gamma_{F_1F_2})$ relating the two reference frames. It is important to take into account the way the spin part and the angular part of the Hamiltonian are affected by rotations. Let λ, μ, l, m be quantum numbers summarizing the transformation of the Hamiltonian under rotation: l is the spatial rotational rank and λ is the rank with respect to rotations of the spin polarizations by the resonant rf field. The component indices m and μ take values $m = -l, -l+1, ..., +l$ and $\mu = -\lambda, -\lambda+1, ... +\lambda$. It follows that

$$\mathcal{H}_{lm\lambda\mu} = [A_{lm}]^R \; D^l_{m\mu}\left(\Omega_{RL}\right) \; T_{\lambda\mu} \tag{2.30}$$

$$= [A_{lm}]^R \, e^{-i\alpha_{RL}m} \, d^l_{m\mu}\left(\beta_{RL}\right) \, e^{-i\gamma_{RL}\mu} \, T_{\lambda\mu} e^{im\omega_r t} \tag{2.31}$$

where $\Omega^{RL} = (\alpha_{RL} - \omega_r t, \beta_{RL}, \gamma_{RL})$ are the Euler angles relating R and L frames. In the high-field approximation, only the terms with $\mu = 0$ needs to be taken into account, so the value of γ_{RL} is irrelevant. Under conditions of fast-MAS we have

$$\beta_{RL} = \arctan\sqrt{2} \quad \Longleftrightarrow \quad d^2_{00}\left(\beta_{RL}\right) = 0$$

and the spin Hamiltonian simplifies to:

$$\mathcal{H}_{lm\lambda 0} = \left[A_{lm}\right]^R D^l_{m0}\left(\Omega^{RL}\right)\, T_{\lambda 0} \tag{2.32}$$

2.7 The Zeeman Interaction

We start analysing the NMR Hamiltonian from the simplest possible case, i.e., an ensemble of isolated spins of the same type. In the absence of an external field, all spin energy levels are degenerate and the spins are randomly oriented, with no net magnetization. A strong, static field breaks the degeneracy by giving a preferential direction to the nuclear spins, parallel to the applied field: this corresponds in the quantum world to unequally populated energy levels.

Classically, the one-spin ensemble is equivalent to a set of isolated magnetic dipole moments $\boldsymbol{\mu_j}$ in an external magnetic field $\mathbf{B}$. The classical energy for the magnetic dipole moment is

$$E_j = -\boldsymbol{\mu_j} \cdot \mathbf{B} \tag{2.33}$$

and its equation of motion can be obtained by considering the torque acting on it as

$$\frac{d\mathbf{J_j}}{dt} = \boldsymbol{\mu_j} \wedge \mathbf{B} \tag{2.34}$$

The angular momentum $\mathbf{J}_j$ is proportional to the magnetic moment $\boldsymbol{\mu_j}$ via

$$\boldsymbol{\mu_j} = \gamma_j \mathbf{J_j} = \gamma_j \hbar\, \mathbf{I_j} \tag{2.35}$$

where γ_j is the gyromagnetic ratio for the nucleus and $\mathbf{I_j}$ is an adimensional quantity proportional to the angular momentum through $\hbar$. For a constant magnetic field, the equation of motion for the magnet is a rotation around the direction of the magnetic field along a conical trajectory with angular frequency $\omega_0 = -\gamma_j B_0$, known as the Larmor frequency. Since energy is conserved, the magnet maintains its initial angle with respect to the applied field. In reality, friction or relaxation act on the magnet by gradually reducing the angle between the dipole and the external magnetic field.

The classical results coincide with the quantum mechanical picture for the spin ensemble, with the Zeeman Hamiltonian for a spin labelled j given, in units of $\hbar$, as

$$\mathcal{H}^j_Z = -\gamma_j B_0 I_{jz} = \omega_0 I_{jz} \tag{2.36}$$

$$= \omega_0 T^j_{10} \tag{2.37}$$

where B_0 is the magnitude of the magnetic field in the z-direction, I_{jz} is the z-component of the spin operator, ω_0 is the energy spacing between adjacent levels in rad/s and equals the Larmor frequency. In terms of ISTOs, T^j_{10} is a first-rank ISTO for one spin j. The eigenvalues and eigenfunctions of the Zeeman Hamiltonian can be deduced by noticing that $\mathcal{H}^j_Z$ is proportional to I_{jz}, i.e.,

$$\mathcal{H}^j_Z \, |l, m\rangle = -\gamma_j B_0 \, m \; |l, m\rangle \tag{2.38}$$

The thermal equilibrium condition corresponds to a set of equally-spaced energy levels whose population follows the Boltzmann distribution as

$$p_k = \frac{\exp\{-E_k/k_B T\}}{\sum_n \exp\{-E_n/k_B T\}}$$

where E_k is energy for the k-th energy level, k_B is Boltzmann's constant, T is the temperature in Kelvin and the sum is extended over all possible levels. The presence of a static field gives rise to a macroscopic spin magnetization, $\mathbf{M}$, proportional both to the field B_0 and to the gyromagnetic ratio γ_j for the nucleus. This amounts to a very small population difference in the normal temperature range, i.e., above 10 K, and is the main reason for the intrinsically low sensitivity of NMR spectroscopy.

2.8 Interaction with a Radio-Frequency Field

In order to observe an NMR spectrum, it is necessary to use electromagnetic radiation with frequency close to the Larmor frequency to excite transitions in the spin system. In general, the interaction between the spin and an external magnetic field is given by

$$\mathcal{H}^j(t) = -\gamma_j \mathbf{I_j} \cdot \mathbf{B}(t)$$

The oscillating radio-frequency (rf) field has the form

$$\mathbf{B}_{\mathrm{rf}}(t) = B^{\mathrm{peak}}_{\mathrm{rf}} \cos(\omega_1 t + \phi)\mathbf{e_x} \tag{2.39}$$

where $B^{\mathrm{peak}}_{\mathrm{rf}}$ is the amplitude, ω_1 is the frequency and ϕ is its phase. This can be decomposed into two components rotating in opposite directions: only the component rotating in the same direction as the spins is effective in inducing transitions. The situation is best described after a transformation from the laboratory frame L to a frame R whose z-axis coincides with $z^{(L)}$ and whose x-axis rotates in the same direction as the resonant rf field component. The rotation angle of the magnetization vector away from $z^{(L)}$ depends on the duration and intensity of the rf perturbation, expressed as

$$\beta_p = \omega^j_{\mathrm{nut}} \tau_p \tag{2.40}$$

where τ_p is the pulse duration, β_p is the flip-angle and $\omega^j_{\mathrm{nut}}/2\pi$ is the nutation frequency of the rf field, defined as

$$\omega^j_{\mathrm{nut}} = \frac{1}{2} \left| \gamma_j B^{\mathrm{peak}}_{\mathrm{rf}} \right| \tag{2.41}$$

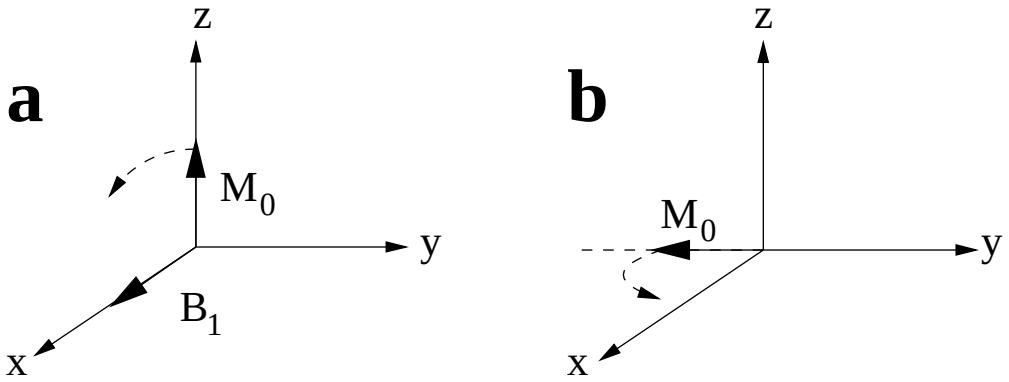

Figure 2.2: 90_x pulse on a system in thermal equilibrium: (a) $\mathbf{M}$ is along z and the rf field B_1 induces a x-rotation. (b) after a 90_x pulse, $\mathbf{M}$ is along the $-y$ direction in the rotating frame and starts precessing around z.

In the rotating frame, the rf Hamiltonian becomes time independent and can be written as

$$\mathcal{H}_{\mathrm{rf}} = \omega^j_{\mathrm{nut}}(I_{jx}\cos\phi + I_{jy}\sin\phi) \tag{2.42}$$

For isolated spins, the effect of the static field and of a resonant rf field on the spin magnetization can be described by a vector representation. Fig 2.2 demonstrates the effect of a 90_x pulse on a system in equilibrium.

2.9 Chemical Shift

When molecules are immersed in an external magnetic field, the nuclei feel not only the effect of the external field but also an induced field, dependent on the local environment. The chemical shift interaction for one spin j can be expressed as

$$\mathcal{H}^j_{CS} \;=\; \gamma_j \mathbf{I}\,\sigma^j\,\mathbf{B} = -\gamma_j \mathbf{I}\,\delta^j\,\mathbf{B} \tag{2.43}$$

where δ^j is the chemical shift (CS) tensor following the deshielding convention and $\mathbf{B}$ is the applied field. After the secular approximation, only the portion of $\mathcal{H}^j_{CS}$ in the z-direction needs to be considered. As for all spin interactions, it is convenient to decompose the CS interaction in terms of spherical tensors of several orders (see Sect. 2.3) in order to separate terms with different orientation dependence.

The rank 0 interaction is the isotropic chemical shift and is related to the trace of the matrix representation of the CS tensor (in any basis)

$$\delta^j_{\mathrm{iso}} = \frac{1}{3}\mathrm{Tr}(\delta^j) \tag{2.44}$$

This term is normally expressed together with the Zeeman term to form a chemically-shifted Larmor frequency

$$\mathcal{H}^{j,\mathrm{iso}}_{CS} = \omega_0(1+\delta^j_{\mathrm{iso}})\,I_{jz} = \omega^j_0\,I_{jz} \tag{2.45}$$

The rank 1 part of the tensor is known as the antisymmetric CS; this term is purely non-secular and is usually neglected from the analysis. The rank 2 tensor is the so-called chemical shift anisotropy (CSA) and is of great importance for many nuclei. The magnitude and orientation of the CSA tensor contain information about the bond nature *and* geometry around the nucleus and can give strong indication for the orientation of the molecular fragment with respect to some reference direction within the molecular system.[3] As for all second-rank tensors, the orientation dependence of this term contributes significantly to the broadness of the NMR signal from solid, static samples. The convention used here for CSA tensors relies on the following definitions:

$$\begin{aligned} \eta &= \frac{\delta^j_{xx} - \delta^j_{yy}}{\delta^j_{zz} - \delta^j_{\mathrm{iso}}} \\ \delta^j_{\mathrm{aniso}} &= \delta^j_{zz} - \delta^j_{\mathrm{iso}} \end{aligned} \tag{2.46}$$

where the three components, expressed in the PAS, are arranged as

$$|\delta^j_{zz} - \delta^j_{\mathrm{iso}}| \geq |\delta^j_{xx} - \delta^j_{\mathrm{iso}}| \geq |\delta^j_{yy} - \delta^j_{\mathrm{iso}}| \tag{2.47}$$

The CSA frequency is given by $\omega^j_{\mathrm{aniso}} = \omega^j_0\, \delta^j_{\mathrm{aniso}}$. This is called the deshielding convention, and coexists with many others.[30,34] A full agreement about it has not been achieved within the NMR community. In terms of ISTOs, the chemical shift and Zeeman Hamiltonian have the form

$$\mathcal{H}^j_{CS} = \omega^j_0 T^j_{10} + \sum_{m=-2}^{2} \omega^j_{\mathrm{aniso}} [A^{CS}_{2m}]^L T^j_{10} \tag{2.48}$$

where A^{CS}_{2m} here indicates in an implicit way the components of the second rank tensor, defined according to Eq. 2.19.

2.10 *J*-coupling

The indirect, or J, coupling is a coupling between nuclear spins which is mediated by the bonding electrons. Its properties and magnitude are therefore strongly dependent upon the nature of the chemical bond and on the orbitals involved in such interaction. Recently J-couplings have been observed mediated by hydrogen bonds.[35] The Hamiltonian for a J-coupling between spins i and j can be expressed in the form

$$\mathcal{H}^{ij}_J = \mathbf{I_i}\, \mathbb{J}\, \mathbf{I_j} \tag{2.49}$$

where $\mathbb{J}$ is the scalar coupling tensor and $\mathbf{I_i}$ and $\mathbf{I_j}$ are the spin operators associated with the interacting nuclei. After decomposition into spherical tensors, the rank 0 interaction is

$$\mathcal{H}^{ij,\mathrm{iso}}_J = 2\pi J_{ij}\, \mathbf{I_i} \cdot \mathbf{I_j} \tag{2.50}$$

$$= 2\pi J_{ij} (I_{zi} I_{zj} + \frac{I_{i+} I_{j-} + I_{i-} I_{j+}}{2}) \tag{2.51}$$

where J_{ij} is the indirect coupling constant in Hertz, corresponding to the isotropic part of the tensor, called the scalar coupling. This is the interaction determining the multiplet patterns well-known in liquid-state NMR spectroscopy. This contribution, even though still present in solid state spectra, is often hidden within wide lines. The rank 1 tensor is usually neglected since it is purely non-secular. The J-anisotropy, even though present, has the same transformation properties of the through-space dipolar coupling (Sect. 2.11) and it is difficult to distinguish from it. In tensor form, the J-coupling can be expressed as

$$\mathcal{H}^{ij}_{J,\text{homo}} = 2\pi J_{ij} T^{ij}_{00} + J^{\text{aniso}}_{ij} T^{ij}_{20} \tag{2.52}$$

In practice, for light nuclei the J-anisotropy is much smaller than the through-space coupling.

For cases in which the coupled spins have very different isotropic chemical shifts, or in the case of heretonuclear J-couplings, the Hamiltonian is further semplified. The second term in Eq. 2.51, known as flip-flop operator, can be removed according to the same ideas behind the secular truncation.

2.11 Through-Space Dipolar Coupling

The through-space, or direct, dipolar coupling Hamiltonian can be obtained by applying the correspondence principle to the expression defining the energy for the interaction between two magnetic dipoles,

$$E = -\frac{\mu_0 \hbar}{4\pi r^3_{ij}} \left[3(\boldsymbol{\mu_i} \cdot \boldsymbol{e_{ij}})(\boldsymbol{\mu_j} \cdot \boldsymbol{e_{ij}}) - (\boldsymbol{\mu_i} \cdot \boldsymbol{\mu_j})\right] \tag{2.53}$$

where r_{ij} is the distance between the dipoles and $\boldsymbol{e_{ij}}$ is a unitary vector in the direction of the vector joining the nuclei i and j. This can be written in terms of the dipolar tensor as

$$\mathcal{H}^{ij}_D = \mathbf{I_i}\, \mathbb{D}\, \mathbf{I_j} \tag{2.54}$$

or, in a more explicit form, after the secular truncation

$$\mathcal{H}^{ij}_D = -\frac{\mu_0 \hbar}{4\pi} \frac{\gamma_i \gamma_j}{r^3_{ij}} \frac{3\cos^2 \Theta_{ij} - 1}{2} (3\, I_{zi} I_{zj} - \mathbf{I_i} \cdot \mathbf{I_j}) \tag{2.55}$$

$$= b_{ij}\, d^2_{00}(\Theta_{ij})(3\, I_{zi} I_{zj} - \mathbf{I_i} \cdot \mathbf{I_j}) \tag{2.56}$$

$$= d_{ij}\, T^{ij}_{20} \tag{2.57}$$

where

$$b_{ij} = -(\mu_0/4\pi)\gamma^2 \hbar / r^3_{ij} \tag{2.58}$$

is the dipolar coupling constant, expressed in angular units, and Θ_{ij} accounts for the orientation of the dipolar vector with respect to the external magnetic field. The dipolar tensor has a vanishing 0-th rank component and so does not have any direct effect on isotropic-phase spectra (neglecting relaxation) and only the rank-2

component is important for spectra in anisotropic phases. This interaction is of great importance for many purposes and the geometrical information content is evident.

For the heteronuclear case, the dipolar Hamiltonian is further semplified

$$\mathcal{H}^{ij}_{D,\text{hetero}} = 2d_{ij}T^i_{10}T^j_{10} \tag{2.59}$$
$$= 2d_{ij}I_{zi}S_{zj} \tag{2.60}$$

by removing the flip-flop term from the homonuclear Hamiltonian. A few ways to exploit the dipolar interaction for structural investigations will be discussed in the chapters to follow.

2.12 Quadrupolar Interaction

For nuclei with spin higher than 1/2, the nucleus has a non-spherical charge distribution, which gives rise to a coupling with an external electric field gradient. The quadrupolar interaction for a spin j can be expressed in the form

$$\mathcal{H}^j_Q = \mathbf{I_j}\,\mathbb{Q}\,\mathbf{I_j} \tag{2.61}$$

where $\mathbb{Q}$ is the quadrupolar tensor. The truncated Hamiltonian after the high-field approximation can be expressed as

$$\mathcal{H}^j_Q = \omega^j_Q(3I^2_{jz} - \mathbf{I_j}\cdot\mathbf{I_j}) \tag{2.62}$$

where ω^j_Q is the nuclear quadrupolar frequency. However the size of the quadrupole coupling is such that higher order effects can be significant. In this case Eq. 2.62 is not sufficient to describe the system. The spatial dependence of quadrupolar terms is such that only the first order terms, described by the second order Legendre polynomial, are averaged out by MAS. A better averaging would require a removal of the second order terms whose dependence follow Legendre polynomials of fourth order. Unfortunately P_2 and P_4 have no common zeroes and more complicated schemes are required in order to remove both.

The quadrupolar interaction is usually more than a small perturbation of the Zeeman Hamiltonian. A full spectroscopy branch, known as nuclear quadrupolar resonance (NQR), consists in performing NMR experiments in zero field, under the effect of the quadrupolar Hamiltonian as the main interaction instead of the Zeeman field. On the other hand, it is advantageous to work in very high magnetic field when dealing with quadrupolar nuclei because the size of the second order terms decreases with the field as ω_0^{-2}.

2.13 Experimental Tools

2.13.1 Magic-Angle-Spinning

A widespread method of increasing resolution in solid state NMR is known as Magic-Angle-Spinning (MAS)[5,31] and consists of rotating the sample rapidly about

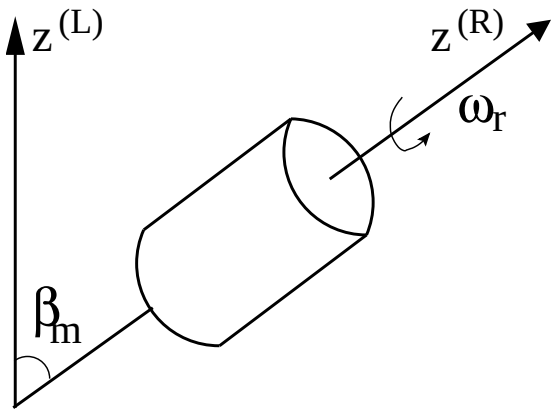

Figure 2.3: Rotor position under MAS. ω_R is the spinning frequency in angular units, $z^{(L)}$ defines the z direction of the laboratory frame while $z^{(L)}$ gives the direction of the rotor-fixed frame.

an axis subtending the 'magic angle' $\beta_m = \arctan\sqrt{2}$ with respect to the main field (see Fig 2.3). The understanding of MAS requires an analysis of the signal coming from a rotating solid. Depending on the spinning speed used and the magnitude of the anisotropic interactions, it is possible to increase resolution by averaging out chemical shift anisotropies (CSA) and through-space dipole-dipole couplings, i.e., all the terms whose anisotropic part can be described by a second rank irreducible spherical tensor.[25] If the angular spinning frequency ω_r exceeds the magnitude of *all* the anisotropic interactions, then the NMR spectrum reduces to the isotropic spectrum with sharp lines at the isotropic chemical shift of each nucleus, while all orientation information disappears (fast-MAS).

An important classification of Hamiltonians is due to Maricq and Waugh,[31] who distinguish two classes: (i) a homogeneous Hamiltonian which does not commute with itself at different times (i.e., homonuclear dipolar interaction), (ii) an inhomogeneous Hamiltonian commutes with itself at different times (i.e., chemical shift). Under MAS, the behaviour of spin interaction belonging to these two groups is very different. In fact, moderate MAS (i.e., not sufficiently fast to average completely all rank 2 tensors) can increase the spectral resolution significantly for cases where the spectrum is dominated by inhomogeneous interactions, while very fast-MAS is needed in the case of homogeneous interactions. This is illustrated in Fig. 2.4, where the cross-polarization spectra of U-^{13}C-glycine are shown at several spinning speeds. In Fig. 2.4a, the static spectrum presents two broad, partly overlapped signals. In Fig. 2.4b the sample is spun at the magic-angle at moderate speed and the broad patterns are broken up into a set of relatively narrow peaks. The fast-MAS condition is not fulfilled, but the resolution still increases. In addition to the main peak (central band) there are some extra peaks, known as spinning sidebands, positioned at a frequency separation equal to multiples of the spinning frequency and whose amplitude is dominated by homogeneous anisotropic interactions, in this case the ^{13}C CSA. In Fig. 2.4c the fast-MAS condition is nearly fullfilled are two small spinning sidebands are just about visible.

2.13.2 Rotational Resonance

The phenomenon of rotational resonance[32,36] is revealed as a peakshape distortion which occurs when the spinning frequency matches the isotropic chemical shift

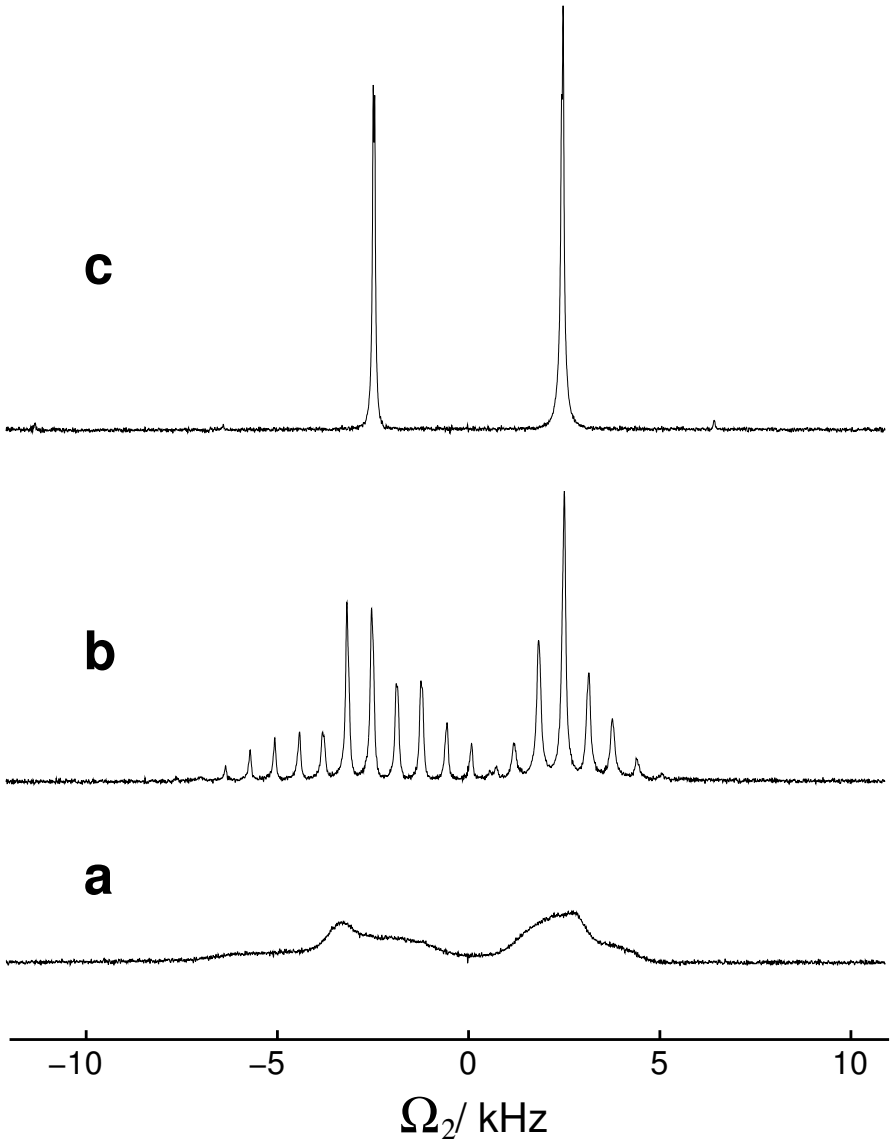

Figure 2.4: (a) Static spectrum of [1,2-$^{13}C_2$]-glycine, 99% labelled, at 4.7 T. (b) MAS spectrum acquired with a spinning frequency of $\omega_r/2\pi$=870 Hz. Notice that the broad pattern is split into many narrow lines whose intensity envelope mimicks the static spectrum (c) MAS spectrum acquired with a spinning frequency of $\omega_r/2\pi$=8 kHz. The fast-MAS regime is achieved and only two narrow lines at the ^{13}C-isotropic chemical shifts are left.

difference between a pair of coupled spins according to the rule

$$n\omega_r = \omega_\Delta^{iso} = \left|\omega_i^{iso} - \omega_j^{iso}\right| \tag{2.63}$$

The $n = 1$ rotational resonance condition is commonly used for the extraction of structural information. A full lineshape analysis at $n = 1$ can lead to geometrical information, due to its strong dependence upon the dipolar coupling between the coupled nuclei. An analysis of magnetization exchange experiments also provides distance information and these are most useful for long distance measurement (the lineshape can be dominated by stronger interactions than the dipolar). In general, contributions from other terms, such as CSA, T_2^{ZQ} and inhomogeneous ZQ lineshape, make the parameters' extraction more difficult but different modifications of the basic RR experiment reduce this dependence and facilitate the parameters' extraction.[37] The situation gets more complicated in the case of high order rotational resonance, $n > 1$. Nevertheless, this method has been successfully applied to measure distances up to 6Å for ^{13}C-pairs and for determining CSA magnitude and orientation.[38,39] Another advantage of RR recoupling is that the anisotropic interactions are reintroduced without the need of rf fields, with an advantage in terms of experimental setup (often quite easy) and with a significant reduction of rf heating problems. Among the many applications of rotational resonance, it is worth mentioning the distance measurements performed in rhodopsin[40] and bacteriorhodopsin.[41]

2.13.3 Heteronuclear Spin Decoupling

In protonated samples such as most organic compounds, the spectral lines are never as narrow as in liquid state even under fast MAS conditions, unless proton decoupling is applied as well. In fact, proton couplings are usually too high to be averaged out completely at accessible speeds and so some kind of radio-frequency decoupling method must be used. The simplest form of heteronuclear decoupling involves irradiation near the ^{1}H Larmor frequency with a continuous, unmodulated rf field. This is called continuous-wave (CW) decoupling. In simple terms, this process can be understood by monitoring the variation of the heteronuclear coupling Hamiltonian term, proportional to $I_z S_z$, under the action of the continuous field on the I channel. The state of the S spin is unchanged, while the rf field causes the I term to rotate and the dipolar term is averaged out every 2π rotation.

It is possible to modulate the proton rf field in terms of its phase, frequency or amplitude. Proper tuning of these parameters according to certain schemes,[3,42–46] known to give better decoupling performance than a continuous irratiation without any modulation. The better the decoupling between the observed nuclei and ^{1}H, the narrower the lines.

Most modulation schemes involve the experimental optimization of one or more parameters and in our experience their performance is appreciably better than conventional CW decoupling only for spinning frequencies above 7 kHz. Therefore all experiments we performed at moderate spinning frequencies involve CW throughout the sequence. All data referred to spinning frequencies above $\omega_r/2\pi > 10$ kHz combine intervals of time-proportional phase modulation[43] (TPPM) decoupling with intervals of CW decoupling.

The problem of decoupling in solid state NMR (both homo- and heteronuclear) is very open and, even though much progress has been made, there is still lots of room for improvement.

2.13.4 Homonuclear Spin Decoupling

As stated before, proton couplings are hardly averaged out by MAS and for many applications it is desirable to remove the homonuclear proton coupling for certain length of time, while maintaing the couplings between the protons and other spin species. This offers a tool for measuring not only internuclear distances but also to correlate the direction of dipolar vectors to provide torsion angles, as discussed briefly in Sect. 4.5.

Some homonuclear decoupling schemes have been known for many years.[47,48] Many of the most common sequences for homonuclear decoupling derive from the Lee-Goldburg (LG) scheme,[47] where the rf field on the proton channel is applied off-resonance so as to produce an effective field tilted at the magic angle with respect to the external static magnetic field. Modifications of the basic LG decoupling by frequency shifts[44] (FSLG) or phase modulation[49,50] (PMLG) lead to improved performance. Other approaches for suppressing the homonuclear couplings have been recently proposed, making use of symmetry-based sequences.[51]

2.13.5 Cross Polarization

Frequently, sensitivity is the main constraint on the feasibility of an experiment, especially when dealing with biological samples. From Eq. 2.39, it is clear that, for a given temperature and field, the observable magnetization is proportional to the gyromagnetic ratio of each nucleus. The sensitivity problem is critical for nuclei with low abundance and low gyromagnetic ratio, called from now on 'rare' nuclei. A clever method to increase the amount of signal consists of using cross polarization (CP)[14] to transfer spin polarization from 'abundant' nuclei to the rare species, according to the scheme shown in Fig. 2.5.

To start with, the I magnetization is flipped into the xy-plane by a $\pi/2$ pulse and then spin-locked for a certain interval of time, known as the contact time, during which an rf field is applied on the S channel as well. A proper choice of the nutation frequencies of the two fields leads to enhanced transverse S magnetization. For static samples the nutation frequencies on the two channels must be tuned to match the Hartmann-Hahn condition, $\omega^I_{\rm nut} = \omega^S_{\rm nut}$. Under fast MAS the CP condition becomes $\omega^I_{\rm nut} = \omega^S_{\rm nut} + k\omega_r$, with k integer. In the standard CP this matching condition is quite stringent and the performance of the sequence in case of mismatch decreases steeply, expecially for high spinning speed.

In many experiments it is routine to have some improved, broader form of CP[15] from spin I to spin S as a first step and the increase in signal is expected to be the ratio γ_I/γ_S in theory. In the case of a ^{13}C-^{1}H system, the ^{13}C-signal usually increases by a factor of around 3.

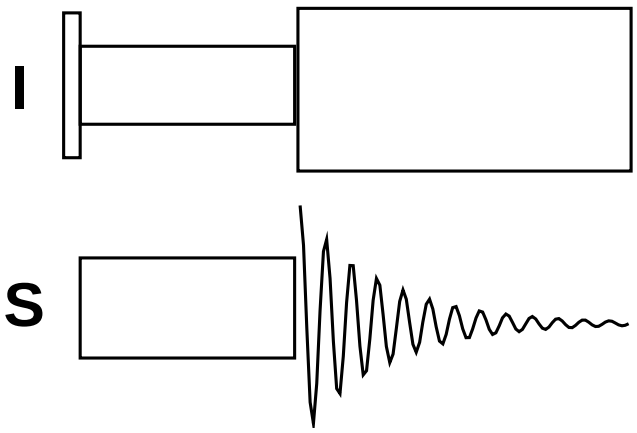

Figure 2.5: Cross-polarization from spin species I to S: the rf nutation frequencies are carefully tuned to achieve polarization transfer from I to S, followed by acquisition of the FID under heteronuclear spin decoupling

2.14 Theoretical Tools

2.14.1 Density Operator

A macroscopic sample is made up of a huge number of interacting spins but its description is simplified if the system can be considered as a multitude of independent systems of just N interacting spins. Properties can be studied over individual spin systems and then statistical arguments can be invoked to describe the overall system.[4,52] Let $|r\rangle$ be a basis set, i.e., any state function can be described as a linear combination of the basis functions according to

$$|\psi\rangle = \sum_r c_r |r\rangle , \qquad c_r \in \mathbb{C} \tag{2.64}$$

and each coefficient c_r gives the amplitude for a contribution from $|r\rangle$ to the overall wave function. The density operator is defined as

$$\rho = \sum_{r,s} \overline{c_r c_s^*} |r\rangle \langle s| \tag{2.65}$$

where the bar denotes averaging over an ensemble of spin systems. Each element of the density matrix (i.e., the matrix representation of the density operator) gives information about how different states are related to one another. Diagonal elements of the density matrix, ρ_{rr}, are the populations of the corresponding states. Off-diagonal elements, ρ_{rs}, are known as coherences and are non-zero only when the states $|r\rangle$ and $|s\rangle$ are statistically correlated. A convenient basis set is given by the angular momentum eigenfunctions and in such basis the coherence order of the state ρ_{rs} is given by $p_{rs} = M_r - M_s$.

The evolution of the spin system under any pulse sequence can be followed by using the density matrix formalism. Two things are needed: a good description for the starting condition of the system and a law to predict its evolution. The answer to the first problem is simple: the status of the system at thermal equilibrium in the presence of a strong magnetic field can be obtained using the Boltzmann distribution:

$$\rho_{\text{eq}} = \frac{1}{2}\left(\mathbb{I} + \beta \hat{I}_z\right) \rightarrow \hat{I}_z \tag{2.66}$$

where $\mathbb{I}$ is the identity operator and β is a factor related to universal constants and to the specific nuclear isotope, field and temperature. In practice, the only term which needs to be considered in calculations is $\hat{I}_z$, since $\mathbb{I}$ is always constant. In what follows we will drop the $\hbar$ symbol to simplify the notation and all energies will be expressed in frequency units, if not otherwise stated. The evolution of the density operator under the effect of a time dependent perturbation $\mathcal{H}(t)$ can be described by

$$\frac{d\rho}{dt} = i\,[\rho, \mathcal{H}] \tag{2.67}$$

which is known as the Liouville-Von Neumann equation and derives directly from the time dependent Schrödinger equation. If the perturbation described by the Hamiltonian $\mathcal{H}$ is time independent, the Liouville-Von Neumann equation simplifies to

$$\rho(t) = e^{-i\mathcal{H}(t-t_0)}\rho(t_0)\, e^{i\mathcal{H}(t-t_0)} \tag{2.68}$$

which relates the density operator at a time t with its value at t_0 and defines the propagator operator $U(t, t_0)$ associated to the Hamiltonian $\mathcal{H}$ as

$$U(t, t_0) = e^{-i\mathcal{H}(t-t_0)} \tag{2.69}$$

For time dependent Hamiltonians is possible to define the propagator U as a unitary operator which relates the evolution of the system between two time points as

$$\rho(t) = U(t, t_0)\, \rho(t_0)\, U^{\dagger}(t, t_0) = \hat{\hat{U}}(t, t_0)\, \rho(t_0) \tag{2.70}$$

The notation is simplified by defining a superoperator[53] $\hat{\hat{A}}$ as

$$\hat{\hat{A}}\ B = A\, B\, A^{\dagger} \tag{2.71}$$

2.14.2 Average Hamiltonian Theory

It is generally not straightforward to relate the original Hamiltonian with the corresponding propagator. It is common to perform a transformation into the so-called interaction frame, in order to put the problem into a form which is easier to handle. If an exact solution is still not possible, average Hamiltonian theory[54] or other approaches[13] can be used to get an approximate solution.

Suppose the total Hamiltonian can be written as

$$\mathcal{H}_{tot}(t) = \mathcal{H}_A(t) + \mathcal{H}_B(t)$$

where, generally, $[\mathcal{H}_A, \mathcal{H}_B] \neq 0$. A transformation to the interaction frame is aimed at factorizing the propagator associated with the whole Hamiltonian into two parts: a term which is easy to calculate, U_A, and a term which can be computed in an approximate form, so that we get:

$$U \;=\; U_A \tilde{U}_B \qquad \text{with} \qquad \tilde{\mathcal{H}}_B = \hat{\hat{U}}_A^{\dagger} \mathcal{H}_B \tag{2.73}$$

The transformation into the interaction frame is denoted by the symbol ˜. The interaction frame Hamiltonian can be expanded according to the Magnus series expansion,[55] defined as:

$$\bar{\mathcal{H}}(t_b, t_a) = \sum_{k=0}^{\infty} \bar{\mathcal{H}}^{(k)}(t_b, t_a)$$

The first terms in the expansion are:

$$\bar{\mathcal{H}}^{(1)} = T^{-1} \int_0^T \tilde{\mathcal{H}}(t) dt \tag{2.74}$$

$$\bar{\mathcal{H}}^{(2)} = (2iT)^{-1} \int_0^T dt' \int_0^{t'} \left[\tilde{\mathcal{H}}(t'), \tilde{\mathcal{H}}(t)\right] dt \tag{2.75}$$

$$\bar{\mathcal{H}}^{(3)} = (6T)^{-1} \int_0^T dt'' \int_0^{t''} dt' \int_0^{t'} \left\{ \left[\tilde{\mathcal{H}}(t''), \left[\tilde{\mathcal{H}}(t'), \tilde{\mathcal{H}}(t)\right]\right] + \left[\left[\tilde{\mathcal{H}}(t''), \tilde{\mathcal{H}}(t'')\right], \tilde{\mathcal{H}}(t)\right] \right\} dt \tag{2.76}$$

This approach is convenient only if the series converges quickly. The Magnus expansion of an operator $\mathcal{H}$ over a time interval τ_{ba} is convergent if

$$\|\mathcal{H}\tau_{ba}\| \ll 1$$

The norm of $\mathcal{H}$ can be taken to be its biggest eigenvalue. For a periodic Hamiltonian it suffices to prove the thesis over one period. For solid state MAS-NMR, it is common to assume that $\mathcal{H}_A = \mathcal{H}_{\text{rf}}$ and $\mathcal{H}_B = \mathcal{H}_{\text{spin}}$.

2.14.3 Other Effective Hamiltonian Theories

The average Hamiltonian thoery is not the only approach to analyze the Hamiltonian describing the system. In particular, Floquet theory[56] is also used by many researchers. Additionally, very recently a new approach has been unveiled and is the so-called exact effective Hamiltonian theory. For a detailed treatment we refer to Ref. 57. The idea behind this exact treatment is that, given a finite operator basis set, it must be also possible to express the effective Hamiltonian for the system as a finite series of terms with at most the same dimensionality as the basis itself.

2.15 Computer Simulation

The state of a spin system can be fully described using the density matrix formalism. The time evolution of the density operator under the effect of a time dependent perturbation $\mathcal{H}(t)$ can be described by Eq. 2.67. In general we deal with time dependent Hamiltonians and it is possible to define the propagator U as a unitary operator which relates the evolution of the system between two time points as

$$\rho(t) = U(t, t_0)\, \rho(t_0)\, U^{-1}(t, t_0) \tag{2.77}$$

Any pulse sequence can be decomposed into a series of pulses and delays, each associated with a time dependent propagator. Once the final density matrix $\rho(t_{\text{final}})$ is obtained, it can be used to evaluate the observable signal $s(t)$, associated with the operator Q_{obs}, as

$$s(t) =< Q_{\text{obs}} > (t) = Tr\{\rho(t)Q_{\text{obs}}\} \tag{2.78}$$

The NMR observable is the transverse magnetization and conventionally the signal is associated with the operator $Q_{\text{obs}} = I_+$.

2.15.1 Powder Averaging

In a powder sample, the final response does not only depend on time but also on orientation parameters, best expressed in terms of Euler angles and summarized as $s(t, \Omega)$, with $\Omega = (\alpha, \beta, \gamma)$. Each crystallite is subject to a slightly different perturbation throughout the sequence due to the orientation dependence in the anisotropic part of the Hamiltonian and so the final signal is the result of a powder average over all relevant orientations

$$\bar{s}(t) = \frac{1}{8\pi^2} \int_0^{2\pi} d\alpha \int_0^{\pi} d\beta \sin\beta \int_0^{2\pi} d\gamma \; s(t, \Omega) \tag{2.79}$$

The powder average defined in Eq. 2.79 can sometimes be simplified by separating the γ-angle averaging from the rest, so that

$$\bar{s}(t) = \frac{1}{4\pi} \int_0^{2\pi} d\alpha \int_0^{\pi} d\beta \sin\beta \; s(t, \alpha, \beta) \tag{2.80}$$

The integral is evaluated as a weighted sum over an ensemble of orientations

$$\bar{s}(t) = \sum_{i=1}^{N} \sum_{j=1}^{M} w_{ij} \; s(t, \alpha_{ij}, \beta_{ij}) \tag{2.81}$$

where the integers N, M depend on the model chosen to generate the angular distribution. The weight of each orientation is proportional to the solid angle it subtends. One of the goals in designing powder averaging schemes is to produce a distribution of weighted crystallite orientations as homogeneous as possible over a unit sphere with the least number of terms. Some popular schemes are, for instance, the Zaremba-Conroy-Wolfsberg scheme (ZCW)[58,59] and REPULSION.[60] A full simulation must be able to evaluate the density matrix *and* the powder averages efficiently. Several approaches are available for simulating solid state NMR experiments and they all are based on the evaluation of Eq. 2.77 and of the powder average in order to get the observable signal, but there is no unique way to do this in practice and the fastest calculation approach may depend on the type of experiment under consideration.

All of the simulation described in the chapters to follow are performed using the ZCW angle distribution, using typically a set of 144 orientations for the $\{\alpha, \beta, \gamma\}$ angles. In general, a comparison of the simulation output using angle distributions of different size should be performed in order to ascertain that the ensemble of orientations is covered with sufficient accuracy.

2.15.2 The Direct Method

The direct method is the implementation of the equation of motion for the density matrix, integrated numerically. The time dependent Hamiltonian $\mathcal{H}(t)$ over an interval τ is divided into N sufficiently small intervals $\Delta\tau$, with $\tau = N\,\Delta\tau$, such that each Hamiltonian $\mathcal{H}(t_i)$ is approximately constant within each interval $\Delta\tau_i$,

$$(i-1)\Delta\tau \leq t_i \leq i\Delta\tau \tag{2.82}$$

The propagator associated with a time independent Hamiltonian is given by Eq. 2.69, otherwise the full propagator is computed numerically as a time-ordered product of all individual propagators on $\Delta\tau_i$

$$e^{i\mathcal{H}(t_N^*)\,(t_N-(N-1)\Delta\tau)} \ldots e^{i\mathcal{H}(t_2^*)\,(t_2-\Delta\tau)} e^{i\mathcal{H}(t_1^*)\,t_1} \tag{2.83}$$

where t_i^* here indicates the time-point in the middle of $\Delta\tau_i$. In the general case, when $[\mathcal{H}(t_i), \mathcal{H}(t_j)] \neq 0$, the time order is essential because the exponential operators do not commute. This approach is easily implementable and is certainly valid, as long as the chosen time segment $\Delta\tau$ is small enough to satisfy the hypothesis. On the other hand, the direct method can be computationally heavy. As in a real experiment, the spectral resolution is related to the overall acquisition time, which implies that the necessary number of sampled points rapidly increases with an increase in the desired frequency resolution, leading to extensive calculations. The direct method is not the best choice when the problem under investigation has some periodicity and this is often the case when dealing with rotating samples. Alternative procedures have been developed for fast calculation of the spectral response under periodic perturbations (e.g. COMPUTE,[61] γ-COMPUTE[62]).

Even though in recent years some rather general simulation packages for solid state NMR experiments have become available,[63] the work presented here uses programs developed within our group, written for simulating rotor-synchronized sequences and based on the COMPUTE algorithm.

Chapter 3

Symmetry-Based Recoupling Sequences

3.1 Introduction

Solid-state NMR has the potential of providing detailed information on molecular structure and electron distribution, but in order to obtain reliable results it is necessary to distinguish different contributions and study the property of interest with as little perturbation as possible from all other interactions. For this reason many solid-state NMR experiments are specific towards the recoupling of certain spin interactions. Selective recoupling reduces the number of parameters that influence the data set and makes the results more precise.

For the case of static samples, the internal Hamiltonian contains the full structural information and is time independent, therefore easier to manipulate; on the other hand, the resolution is quite poor and it may be difficult to identify the property of interest. In rotating samples, MAS at common spinning speeds (up to 30kHz) partly averages out all Hamiltonian terms described by a rank 2 spatial tensor, so it is essential to devise experiments which reintroduce some terms only, while aiding the rotor-driven averaging effect of other interactions and providing high-resolution spectra as well as geometrical information. This implies that the evolution in the spin space and in the real space can *not* be treated separately.

It is a challenging task to select certain spin interactions while suppressing others. Here we aim at investigating spin interactions and molecular structure by using sequences derived on the basis of symmetry arguments.[64] In MAS NMR, spin interactions differ in their transformation properties under rotation both in real space and in spin space. The interactions are distinguished on the basis of their rank with respect to different sorts of rotations (see Table 2.1). So far, the two major classes of symmetry-based recoupling sequences are known with the names of $\mathrm{C}N_n^{\nu}$[8,65] and $\mathrm{R}N_n^{\nu}$[9,66] sequences.

3.2 Definitions for Symmetry-Based Sequences

In order to analyse a symmetry-based sequence unambiguously, one must establish the notation for times and propagators during the sequence, as this convention will be used in what follows. See Ref. 66 for more details

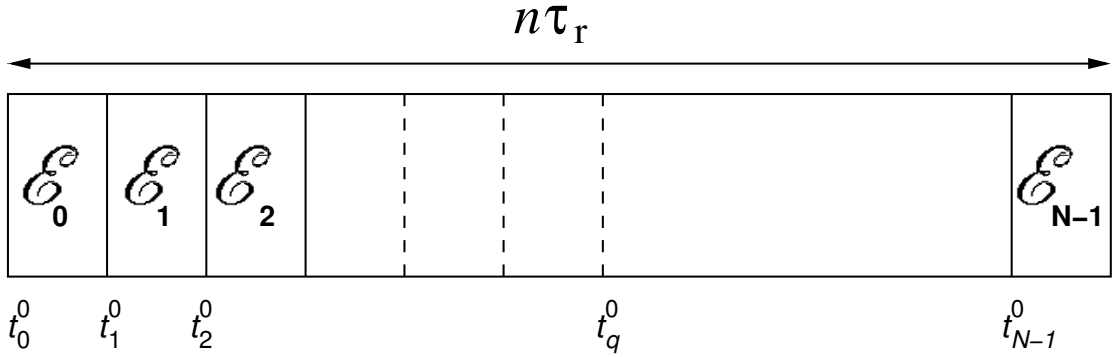

Figure 3.1: Example of a rotor-synchronized pulse sequence fitting N element of equal duration τ_E within n rotor periods, τ_r. The pulse sequence has no gaps with free evolution between pulses.

The symbol "t" is reserved to indicate time points while "τ" is a time interval. The time-point at which the k-th element starts is denoted t_k^0, t_k is the time variable within the k-th element and τ_k is a time interval within the k-th element. An rf propagator $U(t, t_0^0)$ can always be described in terms of three time dependent Euler angles $\Omega(t) = \{\alpha(t), \beta(t), \gamma(t)\}$ as

$$U(t, t_0^0) = R_z(\alpha(t))R_y(\beta(t))R_z(\gamma(t)) \tag{3.1}$$

Given a periodic, rotor-synchronized sequence consisting of a continuous series N elements within n rotor periods, according to the scheme and numbering shown in Fig. 3.1. The general element is $\mathscr{E}_q$ where $q = 0, 1, \ldots, N-1$ and its duration τ_E is such that $T = N\tau_E = n\tau_r$. Without any detail on a particular class of sequences, according to the notation introduced in ref. 66, we can define

- S_q as the rf propagator from t_q^0 to a time t_q within $\mathscr{E}_q$

$$S_q \;=\; U(t_q, t_q^0) \tag{3.2}$$

- E_q as the propagator over one complete $\mathscr{E}_q$

$$E_q \;=\; U(t_{q+1}^0, t_q^0) \tag{3.3}$$

- A_q as the accumulated propagator from t_0^0 to t_q

$$A_q \;=\; U(t_q, t_0^0) = S_q E_{q-1} \ldots E_0 \tag{3.4}$$

Similarly, the time dependence in the Euler angles can be expressed as

$$\{\alpha_q, \beta_q, \gamma_q\} = \{\alpha(t_q), \beta(t_q), \gamma(t_q)\} \tag{3.5}$$

Sequences can be built around desirable symmetry property of the Euler angles, without the need of specifying further details about the exact sequence. This approach is quite general, because there might be different sequences obeying the same symmetry ideas in the Euler angles. We will consider sequences made up of elements $\mathscr{E}_q$ obtained from a basic element $\mathscr{E}^0$, which does not have to coincide with any of the elements $\mathscr{E}_q$, even though all $\mathscr{E}_q$ derive from it. All properties related to $\mathscr{E}^0$ will be labelled with an superscript '0'.

3.3 $\mathbf{CN_n^\nu}$-sequences

The Euler angle symmetry defining CN_n^ν sequences[8,64–66] is given by:

$$\begin{aligned} \beta_q &= \beta_0 \\ \gamma_q &= \gamma_0 - \frac{2\pi\nu}{N}q \end{aligned} \tag{3.6}$$

where symbols N, n and ν are three integers defining the properties of the CN_n^ν sequence. The above transformation is achieved by choosing as $\mathscr{E}^0$ a propagator such that

$$E^0 = R_x(Z_g\pi), \qquad Z_g = \text{even integer} \tag{3.7}$$

which is an rf cycle (indicated C), i.e., E^0 returns the spin to their initial state, if all other interactions are ignored. A possible choice is to use a cycle with phase given by $2\pi\nu q/N$,

$$\mathscr{E}_q^c = \mathrm{C}_{2\pi\nu q/N} \tag{3.8}$$

with $S_0 = S_0^0$ and

$$S_q = R_z\left(\frac{2\pi\nu}{N}q\right) S_0\, R_z\left(-\frac{2\pi\nu}{N}q\right) \tag{3.9}$$

$$E_q = E^0 \tag{3.10}$$

This leads to the interaction Hamiltonian symmetry

$$\tilde{\mathcal{H}}_{lm\lambda\mu}(t_q) = \tilde{\mathcal{H}}_{lm\lambda\mu}(t_0)\exp\left\{i\frac{2\pi q}{N}(-\mu\nu + mn)\right\}$$

The interaction frame Hamiltonian can be derived[66] and leads to the following selection rule for the first order average Hamiltonian:

$$\bar{\mathcal{H}}^{(1)}_{lm\lambda\mu} = 0 \qquad \text{if} \qquad mn - \mu\nu \neq NZ \tag{3.11}$$

where Z is any integer. This implies that pulse sequences selective for specific interactions can be devised by careful choice of the three symmetry numbers N, n and ν. Many CN_n^ν sequences have been designed for a variety of purposes. Examples include torsion angle measurements,[67] multiple-quantum coherence excitation,[68,69] heteronuclear dipolar recoupling,[70] heteronuclear decoupling[45] and shift correlation,[71] to mention a few.

3.4 $\mathbf{RN_n^\nu}$-sequences

A general discussion of RN_n^ν sequences and a set of possible applications are given in Paper I and in refs.[9,64,66] The Euler angle symmetry defining RN_n^ν sequences is given by:

$$\begin{aligned} \beta_q &= \beta_0 + q\pi \\ \gamma_q &= \gamma_0 - \frac{2\pi\nu}{N}q \end{aligned} \tag{3.12}$$

This can be achieved by choosing as $\mathscr{E}^0$ a propagator such that

$$\mathrm{R} = E^0 = R_x(Z_u\pi), \qquad Z_u = \text{odd integer} \tag{3.13}$$

which means that the basic element must be an effective π rotation, indicated R. The $\mathrm{R}N_n^\nu$ sequences can be built by using as basic elements R and $\mathrm{R}^{'}$, where the primed element is given by

$$\mathrm{R}^{'} = E^{0'} = \Pi_x E^0 \Pi_x^\dagger \tag{3.14}$$

The $\mathrm{R}N_n^\nu$ sequence is built by concatenating $N/2$ pair of elements of the form $\mathrm{R}_{\phi_0}\mathrm{R}^{'}_{-\phi_0}$, i.e.,

$$\mathscr{E}_q = (\Pi_x)^q \mathrm{R}_{\phi_0} \, (\Pi_x^\dagger)^q \tag{3.15}$$

with a proper choice of ϕ_0. Define S_q as the rf propagator at a generic time t_q within $\mathscr{E}_q$, starting from the beginning of the element, E_q as the propagator over one complete $\mathscr{E}_q$ and A_q as the accumulated propagator from t_0^0 to t_q, given by

$$A_q = (\Pi_x)^q \, S_0 R_z(-2q\phi_0) \tag{3.16}$$

The next step is to consider the action of such an rf field on the spin Hamiltonian. We want to evaluate the effective Hamiltonian during one full period $T = N \times \tau_R = n \times \tau_r$ of the rf sequence. This requires the evaluation of the spin Hamiltonian in the interaction frame, followed by an Average Hamiltonian Theory treatment over one period. The interaction frame Hamiltonian can be obtained using Eq. 2.73. Let us consider first only the spin-operator part of the spin Hamiltonian, i.e., $T_{\lambda 0}$

$$\hat{A}_q^\dagger T_{\lambda 0} = \hat{\hat{R}}_z(2q\phi_0)\hat{\hat{S}}_0^\dagger \left(\hat{\hat{\Pi}}_x^\dagger\right)^q T_{\lambda 0} = e^{i\pi\lambda q} \sum_\mu T_{\lambda\mu} e^{-i2q\mu\phi_0} D^\lambda_{\mu 0}\left(\Omega_{\mathrm{rf}}\left(t_0\right)\right) \tag{3.17}$$

The interaction frame Hamiltonian is given by terms of the form:

$$\begin{aligned} \tilde{\mathcal{H}}_{lm\lambda\mu}(t_q) &= [A_{lm}]^R \; d^l_{m0}\left(\beta^{RL}\right) e^{-im(\alpha_{RL}+\omega_r t_0^0 - \omega_r t_0)} \, T_{\lambda\mu} D^\lambda_{\mu 0}\left(\Omega_{\mathrm{rf}}\left(t_0\right)\right) \times \\ &\qquad \exp\left\{iq(\pi\lambda - 2\mu\phi_0 + m\omega_r\tau_R)\right\} \\ &= \tilde{\mathcal{H}}_{lm\lambda\mu}(t_0) \exp\left\{i\frac{2\pi q}{N}(\pi\lambda - \mu\nu + mn)\right\} \end{aligned} \tag{3.18}$$

This can be separated into two parts: (i) a term dependent upon the nature of the spin interaction and the form of the pulse sequence element R over the first τ_R interval and (ii) a complex exponential dependent upon both the quantum numbers and the number of R elements, q, defining A_q. The first-order Average Hamiltonian over one period (Eq. 2.74) is given by:[9,72]

$$\bar{\mathcal{H}}^{(1)}_{lm\lambda\mu} = [A_{lm}]^R \, \kappa_{lm\lambda\mu} e^{-im\left(\alpha_{RL}+\omega_r t_0^0\right)} T_{\lambda\mu} \, \mathcal{S} \tag{3.19}$$

with

$$\kappa_{lm\lambda\mu} = d^l_{m0}\left(\beta^{RL}\right) \tau_R^{-1} \int_{t_0^0}^{t_0^0+\tau_R} D^\lambda_{\mu 0}(\Omega_{\mathrm{rf}}(t)) e^{im\omega_r t} dt \tag{3.20}$$

$$\mathcal{S} = \frac{1}{N}\sum_{q=0}^{N-1} \exp(iq\left\{\pi\lambda - 2\mu\phi_0 + m\omega_r\tau_R\right\}) \tag{3.21}$$

were $\kappa_{lm\lambda\mu}$ is the so-called scaling factor.[72] It depends upon the symmetry numbers N, n and upon the basic element and it measures how efficiently the sequence builds up the desired state. It is possible to rewrite $\phi_0 = \frac{\pi\nu}{N}$, $\nu \in \mathbb{R}$, without loss of generality. Moreover, $\omega_r \tau_R = 2\pi n/N$, which gives

$$\mathcal{S} = \frac{1}{N} \sum_{q=0}^{N-1} \exp\left\{ \frac{i2\pi q}{N} \left(\frac{\lambda N}{2} - \mu\nu + mn \right) \right\} \tag{3.22}$$

therefore $\mathcal{S}$ is zero, unless the argument of the exponential function is equal to an integer multiple of $2\pi i$. If we define Z_λ as any integer with the same parity as λ it follows that

$$\bar{\mathcal{H}}^{(1)}_{lm\lambda\mu} = 0 \qquad \text{if} \qquad mn - \mu\nu \neq \frac{N}{2} Z_\lambda \tag{3.23}$$

The $\mathrm{R}N_n^\nu$ first-order selection rules, Eq. 3.23, depend upon the spin rotational rank λ, while the $\mathrm{C}N_n^\nu$ selection rules (3.11) do not. This allows $\mathrm{R}N_n^\nu$ sequences to discriminate between spin interactions on the basis of the parity of the spin rotational rank λ, which creates many new possibilities.

As for the $\mathrm{C}N_n^\nu$-sequences, it is possible to visualize the $\mathrm{R}N_n^\nu$ selection rules in the form of a space-spin selection diagram (SSSD), in which the selection rule itself is represented as a wall, with holes corresponding to the allowed space-spin terms and spacings given by the winding numbers. As an example, Fig. 3.2 shows the SSSD for the symmetry $\mathrm{R}14_2^6$ both for even and odd λ values. This symmetry produces a pure dipolar DQ Hamiltonian, to first order, while suppressing all other interactions, including the CSA terms. Additionally, the fact that only the average Hamiltonian terms $\bar{\mathcal{H}}_{2-122}$ and $\bar{\mathcal{H}}_{212-2}$ are recoupled to first order implies that the DQ signal depends on the γ Euler angle only as a complex exponential, so that the intensity of the DQ signal does not depend on it. All such sequences are labelled as γ-encoded. The full powder average for this class of symmetries leads to an upper limit for DQ filtering efficiencies of 73%. On the other hand, sequences which recouple more than one spin tensor terms for each m value are not γ-encoded and are generally expected to have lower theoretical efficiencies, even though some counter examples are available from simulations.[73]

Paper I gives the theoretical basis for the $\mathrm{R}N_n^\nu$ sequences, together with first and second-order selection rules for the average Hamiltonian. A discussion of the improved performance of $\mathrm{R}N_n^\nu$ sequences with respect to other well-established sequences is accounted for by comparison between the number of terms in the second-order average Hamiltonian. Several symmetries are demonstrated experimentally for a variety of cases, i.e. for homonuclear double-quantum and zero-quantum recoupling, heteronuclear decoupling and heteronuclear recoupling. A list of symmetries for selecting different spin interactions is also given.

Soon after their demonstration on a few test samples in Paper I, the $\mathrm{R}N_n^\nu$ sequences have been successfully implemented for a variety of tasks, including high-resolution ^{1}H-spectroscopy,[51] hereronuclear recoupling,[66,74,75] zero-quantum recoupling,[76] homonuclear dipolar recoupling[77] and correlation spectroscopy.[78]

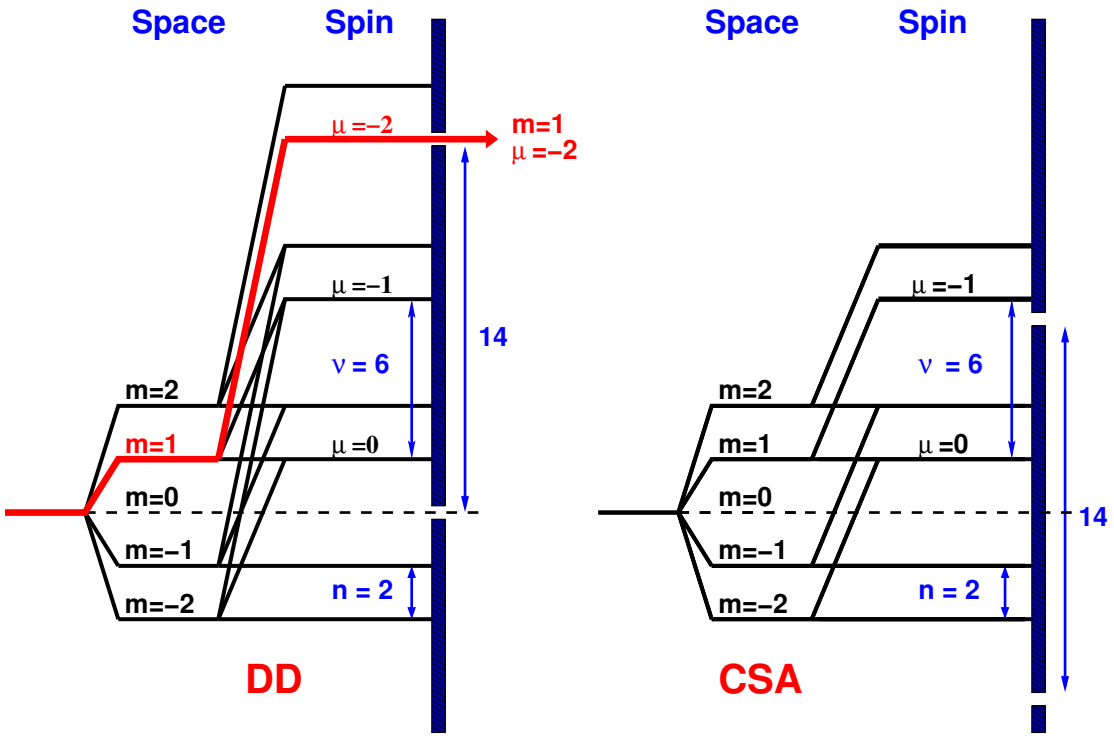

Figure 3.2: SSSD for $\mathrm{R14}^{6}_{2}$. (a) The spin rank $\lambda = 2$ corresponds to even Z_λ the gaps in the selection-rule wall come at $0, \pm N, \pm 2N, \ldots$. (b) The spin rank $\lambda = 1$ corresponds to odd Z_λ values and the gaps in the selection-rule wall come at $\pm N/2, \pm 3N/2, \pm 5N/2, \ldots$

3.5 Time-Phase Relationship

In the discussion above, we considered a windowless series of pulses. The presence of a time delay between two blocks can be accounted for by monitoring the dependence of the Hamiltonian term $\mathcal{H}_{lm\lambda\mu}$ to phase and time variations. Let τ be a generic time interval and ϕ an arbitrary phase, then

$$\mathcal{H}_{lm\lambda\mu}(\tau,\phi) = \mathcal{H}_{lm\lambda\mu}(0,0)\exp\{-i(\mu\phi - m\omega_r\tau)\} \tag{3.24}$$

Time and phase shifts can both be explained in terms of an overall phase shift of the Hamiltonian. For $\mu \neq 0$, it is always possible to compensate for the presence of a time interval by phase adjustements, chosing a phase ϕ such that the argument of the exponential vanishes,

$$\phi = \frac{m\omega_r\tau}{\mu} \tag{3.25}$$

This relationship is used in many 2D experiments and applies not only to symmetry-based sequence.

3.6 Second-Order Average Hamiltonian

The selection of certain interaction is facilitated by symmetry rules for obtaining sequences with the desired first order average Hamiltonian. However, the first order average Hamiltonian is often not sufficient to fully describe the spin system evolution on its own. Unwanted interactions can still give significant contributions if all conditions for truncating the Magnus expansion are not satisfied. Therefore higher order average Hamiltonian terms can discriminate between "good" sequences and "bad" sequences, even though $\bar{\mathcal{H}}^{(1)}_{lm\lambda\mu}$ is the same. Unfortunately, when dealing with $\bar{\mathcal{H}}^{(k)}$, with $k \geq 2$ the formulae tend to get much more complicated than in the $\bar{\mathcal{H}}^{(1)}$ case. It is convenient to make all equations as compact as possible, so we use the following abbreviations (following the notation in Ref.[45]):

$$\begin{aligned}
M_j &= m_j n - \mu_j \nu + \frac{\lambda_j N}{2} && (3.26)\\
x_j &= \exp\{i2\pi M_j/N\} && (3.27)\\
f(t_2,t_1) &= \left[\tilde{\mathcal{H}}_{l_2m_2\lambda_2\mu_2}(t_2), \tilde{\mathcal{H}}_{l_1m_1\lambda_1\mu_1}(t_1)\right] && (3.28)\\
&= d^{l_2}_{m_20}\left(\beta^{RL}\right) D^{\lambda_2}_{\mu_20}\left(\Omega_{\mathrm{rf}}(t_2)\right)\; d^{l_1}_{m_10}\left(\beta^{RL}\right) D^{\lambda_1}_{\mu_10}\left(\Omega_{\mathrm{rf}}\left(t_1\right)\right) e^{i(m_1t_1+m_2t_2)\omega_r} \times \\
&\quad \left[A_{l_1m_1}\right]^R \left[A_{l_2m_2}\right]^R e^{-i(m_1+m_2)(\alpha_{RL}+\omega_r t_0^0)}\; \left[T_{\lambda_2\mu_2}, T_{\lambda_1\mu_1}\right] \\
\left[T_{\lambda_2\mu_2}, T_{\lambda_1\mu_1}\right] &= \sum_{\lambda=|\lambda_1-\lambda_2|}^{\lambda_1+\lambda_2} c_\lambda T_{\lambda(\mu_2+\mu_1)} && (3.29)
\end{aligned}$$

where the c_λ are related to the Clebsch-Gordan coefficients.[25] The time relationship between R element is translated in the form

$$f(t_2 + q_2\tau_R, t_1 + q_1\tau_R) = (x_1)^{q_1}(x_2)^{q_2} f(t_2,t_1) \tag{3.30}$$

Apart from multiplicative constants, the second order Average Hamiltonian is

$$\bar{\mathcal{H}}^{(2)}_{l_2m_2\lambda_2\mu_2;l_1m_1\lambda_1\mu_1} = (2iT)^{-1}\int_0^T dt_2\int_0^{t_2} f(t_2,t_1)dt_1 \propto \mathcal{S}^{(2)}_{\square}\,\mathcal{A}^{(2)}_{\square} + \mathcal{S}^{(2)}_{\triangle}\,\mathcal{A}^{(2)}_{\triangle} \tag{3.31}$$

where

$$\mathcal{S}^{(2)}_{\square} = \sum_{q_2=1}^{N-1} x_2^{q_2}\sum_{q_1=0}^{q_2-1} x_1^{q_1} \tag{3.32}$$

$$\mathcal{A}^{(2)}_{\square} = \int_{t_0^0}^{t_0^0+\tau_R} dt_2\int_{t_0^0}^{t_0^0+\tau_R} f(t_2,t_1)dt_1 \tag{3.33}$$

$$\mathcal{S}^{(2)}_{\triangle} = \sum_{q=0}^{N-1} x_2^q\, x_1^q \tag{3.34}$$

$$\mathcal{A}^{(2)}_{\triangle} = \int_{t_0^0}^{t_0^0+\tau_R} dt_2\int_{t_0^0}^{t_2} f(t_2,t_1)dt_1 \tag{3.35}$$

$\mathcal{S}^{(2)}$ terms depend upon symmetry-based rules. Second order rules and size of the symmetry allowed terms for $\mathrm{R}N_n^\nu$ sequences can be estimated using symmetry arguments.[73]

3.7 Supercycles

Given a well-behaved first order average Hamiltonian obtained through symmetry arguments, it may be desirable to improve its performance by simple modification of the basic sequence. This is often achieved by building up a so-called supercycle. One of the goal of supercyling is to invoke some higher symmetry to get rid of undesired high-order terms and thereby to achieve better performance. In what follows we will explore two different kind of supercycles and consider their effects to first and second order in average Hamiltonian theory.

3.7.1 π-supercycles

Let us consider as an example the supercycle $\mathcal{C}\bar{\mathcal{C}}$, where $\mathcal{C}$ corresponds to a set of N contiguous elements of any $\mathrm{R}N_n^\nu$ sequence and $\bar{\mathcal{C}}$ denotes the same block but with a global phase shift of π. The accumulated propagator is

$$A_q = (\Pi_x)^q\, S_0 R_z(-2q\phi_0) \qquad 0 \le q \le N-1 \tag{3.36}$$

$$\begin{aligned} A_q &= \Pi_z\,(\Pi_x)^q\, S_0 R_z(-2(q-N)\phi_0)\Pi_z^\dagger\,\mathbb{I} \\ &= \Pi_z\,(\Pi_x)^q\, S_0 R_z(-2q\phi_0)\Pi_z^\dagger \qquad N \le q \le 2N-1 \end{aligned} \tag{3.37}$$

If we consider the effect of such terms on the equilibrium density operator, $T_{\lambda 0}$, there is an additional π phase-shift, depending if we are in the first block or in the second. If we define k to be 0 for the first block and 1 for the second, then

$$\hat{\bar{A}}_q^\dagger T_{\lambda 0} = e^{i\pi\lambda q}\sum_\mu D^\lambda_{\mu 0}\left(\Omega_{\mathrm{rf}}\left(t_0\right)\right) e^{-i2q\mu\phi_0}\, T_{\lambda\mu}\times(-1)^{k\mu} \tag{3.38}$$

It follows that the interaction frame Hamiltonian is

$$\begin{aligned}\tilde{\mathcal{H}}_{lm\lambda\mu}(t_q) &= [A_{lm}]^R\, d^l_{m0}\left(\beta^{RL}\right) e^{-im(\alpha_{RL}+\omega_r t_0^0)} e^{im\omega_r t_0}\, T_{\lambda\mu} D^{\lambda}_{\mu 0}\left(\Omega_{\mathrm{rf}}\left(t_0\right)\right) \times \\ &\qquad \exp\left\{iq(\pi\lambda - 2\mu\phi_{_0} + m\omega_r\tau_R)\right\}\,(-1)^{k\mu}\end{aligned}$$

and, recalling Eqs. 3.20 and 3.21, the average Hamiltonian is

$$\bar{\mathcal{H}}^{(1)}_{lm\lambda\mu} = [A_{lm}]^R\, \kappa_{lm\lambda\mu} e^{-im\left(\alpha_{RL}+\omega_r t_0^0\right)}\, T_{\lambda\mu}\, \mathcal{S}\, \mathcal{S}' \qquad \text{with} \tag{3.39}$$

$$\mathcal{S}' = \frac{1}{2}\sum_{k=0}^{1}(-1)^{k\mu} = \begin{cases} 0 & \mu = \text{odd} \\ 1 & \mu = \text{even} \end{cases} \tag{3.40}$$

Terms with odd μ values are forbidden by the selection rule $\mathcal{S}'$, even though they might be allowed from $\mathcal{S}$ alone.

The behaviour of $\bar{\mathcal{H}}^{(2)}$ with this two-step supercycle can be related to the basic block by

$$\begin{aligned}\mathcal{S}^{(2)}_{\square,2} &= \sum_{q_2=1}^{N-1} x_2^{q_2} \sum_{q_1=0}^{q_2-1} x_1^{q_1} + (-)^{\mu_2} \sum_{q_2=N}^{2N-1} x_2^{q_2} \sum_{q_1=0}^{N-1} x_1^{q_1} + (-)^{\mu_2+\mu_1} \sum_{q_2=N+1}^{2N-1} x_2^{q_2} \sum_{q_1=N}^{q_2-1} x_1^{q_1} \\ &= \left(1+(-1)^{\mu_2+\mu_1}\right) \sum_{q_2=1}^{N-1} x_2^{q_2} \sum_{q_1=0}^{q_2-1} x_1^{q_1} + (-1)^{\mu_2} \sum_{q_2=0}^{N-1} x_2^{q_2} \sum_{q_1=0}^{N-1} x_1^{q_1} \\ &= \left(1+(-1)^{\mu_2+\mu_1}\right) \mathcal{S}^{(2)}_{\square} + (-1)^{\mu_2} \mathcal{S}^{(1)}_1 \mathcal{S}^{(1)}_2 \end{aligned} \tag{3.41}$$

$$\mathcal{S}^{(2)}_{\triangle,2} = \left(1+(-1)^{\mu_2+\mu_1}\right) \sum_{q=0}^{N-1} x_2^q\, x_1^q = \left(1+(-1)^{\mu_2+\mu_1}\right)\, \mathcal{S}^{(2)}_{\triangle} \tag{3.42}$$

The first term in $\mathcal{S}^{(2)}_{\square,2}$, as well as $\mathcal{S}^{(2)}_{\triangle,2}$, resemble what we had for the basic sequence and the multiplicative factor makes them vanish if $(\mu_1+\mu_2)$ is odd; the second term in $\mathcal{S}^{(2)}_{\square,2}$ is related to the first order selection rule $\mathcal{S}^{(1)}$ and it exists only if both terms are allowed in $\bar{\mathcal{H}}^{(1)}$; its sign is μ-dependent and might affect the way that different terms in $\bar{\mathcal{H}}^{(2)}$ add together, but has no direct effect on a single term. Similarly for 4-step supercycle $\mathcal{C}\bar{\mathcal{C}}\bar{\mathcal{C}}\mathcal{C}$ we get

$$\begin{aligned}\mathcal{S}^{(2)}_{\square,4} &= 2\left(1+(-)^{\mu_2+\mu_1}\right)\mathcal{S}^{(2)}_{\square} + \mathcal{S}^{(1)}_1\mathcal{S}^{(1)}_2\left(1+(-)^{\mu_2+\mu_1}+2(-)^{\mu_1}+2(-)^{\mu_2}\right) \\ \mathcal{S}^{(2)}_{\triangle,4} &= 2\left(1+(-1)^{\mu_2+\mu_1}\right)\,\mathcal{S}^{(2)}_{\triangle}\end{aligned}$$

The only difference is that another factor vanishes when $(\mu_1+\mu_2)$ is odd (and has different values if both terms are odd or even). If we consider γ-encoded sequences for pure DQ dipolar recoupling, the number of terms in $\bar{\mathcal{H}}^{(2)}$ varies but there is a subset of terms which remain. For any sequence, $\bar{\mathcal{H}}^{(2)}$ can be simplified by supercycling and for *all* sequences this leads to the same minimum number of terms. The fact that the sequence performance does not always improve might depend on: (i) higher order terms, (ii) increase in the period of pulse sequence and its consequence in terms of average Hamiltonian theory, (iii) scaling factor.

3.7.2 ν-inverted supercycles

For $(\mathrm{R}N_n^{\nu})(\mathrm{R}N_n^{-\nu})$, the accumulated propagator in the second block is

$$A_q = \Pi_x \left(\Pi_x\right)^q S_0 R_z(-2(q-N)\phi_0)\Pi_x^{\dagger}\,\mathbb{I} = \left(\Pi_x\right)^{q+1} S_0\, R_z(-2q\phi_0)\Pi_x^{\dagger} \quad (3.43)$$

As before, we can define a block counter k and write the effect of A_q on the equilibrium density operator, $T_{\lambda 0}$, in a general way as

$$A_q = \left(\Pi_x\right)^{q+k} S_0\, R_z(-2q\phi_0)(\Pi_x^{\dagger})^k \quad (3.44)$$

$$\hat{\tilde{A}}_q^{\dagger} T_{\lambda 0} = e^{i\pi\lambda q} \sum_{\mu} D_{\mu 0}^{\lambda}\left(\Omega_{\mathrm{rf}}\left(t_0\right)\right) e^{-i2q\mu\phi_0}\, T_{\lambda(-)^k\mu} \quad (3.45)$$

The interaction frame Hamiltonian is

$$\begin{aligned}\tilde{\mathcal{H}}_{lm\lambda\mu}(t_q) = {} & [A_{lm}]^R\; d_{m0}^{l}\left(\beta^{RL}\right) e^{-im(\alpha_{RL}+\omega_r t_0^0)} e^{im\omega_r t_0}\, T_{\lambda(-)^k\mu} D_{\mu 0}^{\lambda}\left(\Omega_{\mathrm{rf}}\left(t_0\right)\right) \times \\ & \exp\left\{iq(\pi\lambda - 2\mu\phi_0 + m\omega_r\tau_R)\right\}\end{aligned} \quad (3.46)$$

and now the block dependence is in the tensor, instead of being in the complex exponential. The selection rule coincides with normal $\mathrm{R}N_n^{\nu}$ sequences in the case $\mu = 0$. For the general case, it is better to take into account all together terms associated with opposite μ values. Recalling Eqs. 3.20 and 3.21, the average Hamiltonian is

$$\bar{\mathcal{H}}_{lm\lambda\mu}^{(1)} = \frac{1}{2}\left[A_{lm}\right]^R \kappa_{lm\lambda\mu} e^{-im\left(\alpha_{RL}+\omega_r t_0^0\right)}\left(T_{\lambda\mu} + T_{\lambda-\mu}\right)\mathcal{S} \quad (3.47)$$

which doesn't look particularly nice. Let's remove k from the tensor and redefine it in terms of a blending of μ values and blocks, as

$$\begin{aligned}\tilde{\mathcal{H}}_{lm\lambda\mu}(t_q) = {} & [A_{lm}]^R\; d_{m0}^{l}\left(\beta^{RL}\right) e^{-im(\alpha_{RL}+\omega_r t_0^0)} e^{im\omega_r t_0}\, T_{\lambda\mu} D_{\mu 0}^{\lambda}\left(\Omega_{\mathrm{rf}}\left(t_0\right)\right) \times \\ & (-)^{k\mu} e^{i2k\mu\phi_0} \exp\left\{iq(\pi\lambda - 2(-)^k\mu\phi_0 + m\omega_r\tau_R)\right\}\end{aligned}$$

leading to

$$\begin{aligned}\bar{\mathcal{H}}_{l\pm m\lambda\mu}^{(1)} = {} & \bar{\mathcal{H}}_{lm\lambda\mu,0}^{(1)} + \bar{\mathcal{H}}_{lm\lambda-\mu,1}^{(1)} = \frac{1}{2}\left[A_{lm}\right]^R e^{-im\left(\alpha_{RL}+\omega_r t_0^0\right)} \kappa_{lm\lambda\mu} T_{\lambda\mu} \times \\ & \left(\mathcal{S}_+ + (-)^{\mu}\, e^{i2\mu\phi_0}\mathcal{S}_-\right) \\ \mathcal{S}_+ = {} & \frac{1}{N}\sum_{q=0}^{N-1} \exp\left\{\frac{i2\pi q}{N}\left(\frac{\lambda N}{2} - \mu\nu + mn\right)\right\} \\ \mathcal{S}_- = {} & \frac{1}{N}\sum_{q=0}^{N-1} \exp\left\{\frac{i2\pi q}{N}\left(\frac{\lambda N}{2} + \mu\nu + mn\right)\right\}\end{aligned}$$

The selection rule 3.21 still holds, but this supercycle leads to the loss of γ encoding: given a specific tensor element $T_{\lambda\mu}$, $\pm m$ components are selected. If we use Eq. 3.46 for the interaction Hamiltonian, we decompose $\bar{\mathcal{H}}^{(2)}$ in a convenient way, as

$$\begin{aligned} f(t_2,t_1) = {} & \left[\tilde{\mathcal{H}}_{l_2m_2\lambda_2\mu_2,\,k_2}(t_2), \tilde{\mathcal{H}}_{l_1m_1\lambda_1\mu_1,\,k_1}(t_1)\right] = g(t_2,t_1)\left[T_{\lambda_2(-)^{k_2}\mu_2}, T_{\lambda_1(-)^{k_1}\mu_1}\right] \\ \mathcal{A}_{\square,2}^{(2)} = {} & \int_{t_0^0}^{t_0^0+\tau_R} dt_2 \int_{t_0^0}^{t_0^0+\tau_R} g(t_2,t_1)dt_1 \\ \mathcal{A}_{\triangle,2}^{(2)} = {} & \int_{t_0^0}^{t_0^0+\tau_R} dt_2 \int_{t_0^0}^{t_2} g(t_2,t_1)dt_1 \end{aligned}$$

and the second order selection rules become

$$\begin{aligned}
\mathcal{S}^{(2)}_{\square,2} &= \sum_{q_2=1}^{N-1}\sum_{q_1=0}^{q_2-1} x_2^{q_2}\, x_1^{q_1}\,[T_{\lambda_2\mu_2}, T_{\lambda_1,\mu_1}] + \sum_{q_2=N}^{2N-1}\sum_{q_1=0}^{N-1} x_2^{q_2}\, x_1^{q_1}\,[T_{\lambda_2-\mu_2}, T_{\lambda_1,\mu_1}] \\
&\quad + \sum_{q_2=N+1}^{2N-1}\sum_{q_1=N}^{q_2-1} x_2^{q_2}\, x_1^{q_1}\,[T_{\lambda_2-\mu_2}, T_{\lambda_1,-\mu_1}] \\
&= \mathcal{S}^{(2)}_{\square}\,([T_{\lambda_2\mu_2}, T_{\lambda_1,\mu_1}] + [T_{\lambda_2-\mu_2}, T_{\lambda_1,-\mu_1}]) + \mathcal{S}^{(1)}_1\mathcal{S}^{(1)}_2\,[T_{\lambda_2-\mu_2}, T_{\lambda_1,\mu_1}] \qquad (3.48) \\
\mathcal{S}^{(2)}_{\triangle,2} &= \mathcal{S}^{(2)}_{\triangle}\,([T_{\lambda_2\mu_2}, T_{\lambda_1,\mu_1}] + [T_{\lambda_2-\mu_2}, T_{\lambda_1,-\mu_1}]) \qquad (3.49)
\end{aligned}$$

I have verified numerically that

$$[T_{\lambda_2\mu_2}, T_{\lambda_1,\mu_1}] + [T_{\lambda_2-\mu_2}, T_{\lambda_1,-\mu_1}] = 0 \qquad \text{if} \qquad \mu_2 + \mu_1 = 0 \qquad (3.50)$$

which eliminates the z-rotation perturbation, as expected. Unfortunately, this condition does not hold for any λ_1, λ_2 but only for certain cases, i.e. it always holds when the tensors refer to the same interaction **and** order and it holds sometimes for some cross-terms between different interactions, but not generally. All cross-term between $+1$ and -1 components of the CSA tensor disappear.

3.8 Field Imperfections

Sometimes the discrepancy between experimental results and simulation is quite evident. In the case of pulse sequences made up by a series of continuous pulses, with no windows, some interference between neighboring pulses might affect the experiment. Such effects can be minimised by designing sequences with good compensation of these problems.

3.8.1 RF Field Inhomogeneity

In Table 2.1 are summarized the transformation properties of several interactions, including rf terms. In presence of rf field inhomogeneity, crystallites occupying different positions might experience at a certain time point slightly different rf fields. The effective Hamiltonian in Eq. 3.19 is derived for a system with an initial Hamiltonian whose spin part is simply $T_{\lambda 0}$. That is not the case for rf inhomogeneities, for which the spin part is $T_{1\pm1}$. Therefore the rf term must be treated separately and can be included in the average Hamiltonian treatment by transforming to the interaction frame not only the spin Hamiltonian but also the difference between the nominal amplitude and the actual value as follows

$$\mathcal{H}_B(t) = \mathcal{H}_{lm\lambda 0}(t) + \Delta\omega^S_{\text{nut}}(t,\mathbf{r})\, R_z(\phi) I_{x_{tot}} R_z(-\phi) = \mathcal{H}_{lm\lambda 0}(t) + \mathcal{H}_\epsilon(t) \qquad (3.51)$$

It is customary to write rf inhomogeneities in a form which assumes that the additional term describing the imperfection is proportional to the "nominal" rf Hamiltonian at any time:

$$\mathcal{H}_\epsilon(t) = \epsilon \mathcal{H}_{\text{rf}}(t) \qquad (3.52)$$

where $\epsilon(\mathbf{r})$ accounts for the position dependence. As for the main rf field,

$$\mathcal{H}_\epsilon\left(t_q\right) = \left(\hat{\bar{\Pi}}_x\right)^q \mathcal{H}_\epsilon\left(t_0\right) \tag{3.53}$$

We have already calculated the first term of Eq. 3.51 in the interaction frame and its average over one period and the results in Eq. 3.23 still apply. For the second term, the interaction frame Hamiltonian is given by

$$\begin{aligned}
\tilde{\mathcal{H}}_\epsilon(t_q) &= \hat{A}_q^\dagger \mathcal{H}_\epsilon\left(t_q\right) = \hat{\bar{R}}_z(2q\phi_0)\hat{S}_0^\dagger(\hat{\bar{\Pi}}_x^\dagger)^q \left(\hat{\bar{\Pi}}_x\right)^q \mathcal{H}_\epsilon\left(t_0\right) \\
&= \hat{\bar{R}}_z(2q\phi_0)\,\hat{\bar{S}}_0^\dagger\,\mathcal{H}_\epsilon\left(t_0\right) \\
&= \hat{\bar{R}}_z(2q\phi_0)\,\tilde{\mathcal{H}}_\epsilon(t_0) \\
&= \sum_{\mu=-1}^{1} \tilde{\omega}_{1\mu}^\epsilon\left(t_0\right) T_{1\mu} \times \exp\left\{-\frac{i2\pi\, q}{N}\,\mu\nu\right\}
\end{aligned} \tag{3.54}$$

where the exact form of $\tilde{\omega}_{1\mu}^\epsilon\left(t_0\right)$ depends on the form of the R element. If $[\mathcal{H}_{\rm rf}(t_q), S_q] = 0$, this simplifies to

$$\tilde{\mathcal{H}}_\epsilon(t_q) = \hat{\bar{R}}_z(2q\phi_0)\,\mathcal{H}_\epsilon\left(t_0\right) = \sum_{\mu=\pm1} \omega_{1\mu}^\epsilon\left(t_0\right) T_{1\mu} \times \exp\left\{-\frac{i2\pi\, q}{N}\,\mu\nu\right\} \tag{3.55}$$

$$\text{with} \qquad \omega_{1\mu}^\epsilon\left(t_0\right) = \epsilon\,\omega_{\rm nut}^S(t_0)\, e^{-i\mu\phi_0}$$

since $\mathcal{H}_\epsilon\left(t\right)$ is proportional to the main rf term. Eq. 3.55 is fulfilled if the pulse sequence element R consists of pulses whose representation Hamiltonians commute with one another, as when the individual pulses within R are rotations around the same axis, i.e. with relative phase shift equal either 0 or π. This situation is indicated in the following as the *amplitude-modulation* (AM) case. In this case the $\mu = 0$ component of the $T_{1\mu}$ tensor is absent. Introducing a $\lambda' = 0$ for convenience, we get

$$\bar{\mathcal{H}}_{00\lambda'\mu}^\epsilon = \tau_R^{-1} T_{1\mu} \int_{t_0^0}^{t_0^0+\tau_R} \tilde{\omega}_{1\mu}^\epsilon\left(t\right) dt \times \mathcal{S}' \tag{3.56}$$

$$\text{with} \qquad \mathcal{S}' = \frac{1}{N}\sum_{q=0}^{N-1} \exp\left\{-\frac{i2\pi\, q}{N}\,\mu\nu\right\} \tag{3.57}$$

It follows that

$$\mathcal{S}' = \begin{cases} 0 & \mu\nu \neq \frac{N}{2} Z_{\lambda'} \\ 1 & \mu\nu = \frac{N}{2} Z_{\lambda'} \end{cases} \tag{3.58}$$

where $Z_{\lambda'}$ is an even integer, while the real spin rank is $\lambda = 1$. This analysis shows that rf field inhomogeneity may be represented in the selection rule 3.23 by including a term with an *even* effective spin rank.

3.8.2 RF Transients

There are two kinds of rf transients: real transients (same phase as the generating pulse) and quadrature transients (90° phase shifted with respect to the pulse). Both give rise to symmetric (leading and falling transients have same sign) and asymmetric transients (leading and falling transients have opposite sign). I define a rise and a fall coefficient respectively as $b_\uparrow(t)$ and $b_\downarrow(t)$, containing the combined effect of symmetric and asymmetric part. These coefficients do not depend upon the q-interval, i.e.,

$$b_\uparrow(t_q) = b_\uparrow(t_0) = b_\uparrow \tag{3.59}$$

and their time dependence will be made implicit. The rf transients can be expressed as

$$\mathcal{H}^\epsilon_{\rm rf}(t_q) \;\; = \mathcal{H}^\epsilon_{\rm rf,real}(t_q) + \mathcal{H}^\epsilon_{\rm rf,quad}(t_q) \tag{3.60}$$

For relatively long rf pulses it is reasonable to assume that the transient effect from one pulse dies out within the next one. The form of the rf field at each time point depends on the amplitude and phase of the current pulse and on amplitude and phase of the previous pulse. To start with a simple case, let R= Π_x. The ideal rf Hamiltonian is constant thoughout each pulse

$$\mathcal{H}_{\rm rf}(t_q) = \hat{\hat{R}}_z(\phi_q) H^0_0 = H_q \tag{3.61}$$

where H^0_0 is proportional to I_x and H_q includes the $\pm\phi_0$ phase alternation and H_q indicates the Hamiltonian for the q-th element. For the real transients

$$\begin{aligned} \mathcal{H}^\epsilon_{\rm rf,real}(t_q) &= b_\uparrow\, H_q + \, b_\downarrow\, H_{q-1} \\ &= b_\uparrow (\hat{\hat{\Pi}}_x)^q\, H_0 + \, b_\downarrow (\hat{\hat{\Pi}}_x)^{q-1}\, H_0 \end{aligned} \tag{3.62}$$

leading to the interaction frame Hamiltonian

$$\begin{aligned} \tilde{\mathcal{H}}^\epsilon_{\rm rf,real}(t_q) &= \hat{\hat{R}}_z(2q\phi_0)\, \hat{\hat{S}}^\dagger_0 \left\{ b_\uparrow + b_\downarrow\, (\hat{\hat{\Pi}}^\dagger_x) \right\} H_0 \\ &= \sum_{\mu=-1}^{1} \left(b_\uparrow \omega^{\rm rf}_{1\mu} + b_\downarrow \tilde{\omega}^{b,{\rm rf}}_{1\mu} \right)\, T_{1\mu} \times \exp\left\{ -\frac{i2\pi q\, \mu\nu}{N} \right\} \end{aligned}$$

where $\omega^{\rm rf}_{1\mu}$ and $\tilde{\omega}^{b,{\rm rf}}_{1\mu}$ are coefficients accounting for the action of S_0, which commutes with the first term but not with the second, therefore the $\mu = 0$ component must be considered. The average Hamiltonian is given by

$$\bar{\mathcal{H}}^{\rm rf}_{00\lambda'\mu} = \tau_R^{-1} T_{1\mu} \int_{t^0_0}^{t^0_0+\tau_R} f(t)\, dt \times \mathcal{S}' \tag{3.63}$$

$$\text{with} \qquad \mathcal{S}' = \frac{1}{N} \sum_{q=0}^{N-1} \exp\left\{ -\frac{i2\pi\, q}{N}\, \mu\nu \right\} \tag{3.64}$$

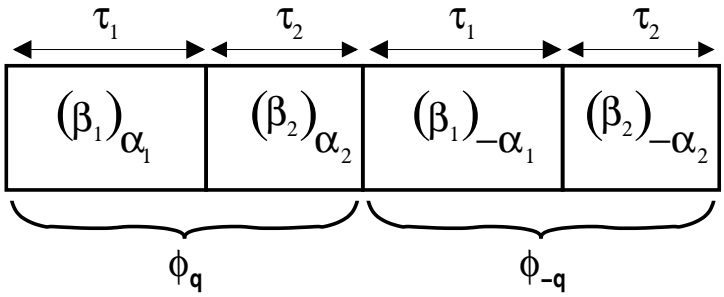

Figure 3.3: Sketch of two consecutive R elements, related to each other by complete phase inversion.

The selection rule follows Eq. 3.58. For the quadrature term we have

$$\begin{aligned}\mathcal{H}_{\mathrm{rf,quad}}(t_q) &= b_\uparrow' \hat{\hat{R}}_z(\pi/2) H_q + b_\downarrow' \hat{\hat{R}}_z(\pi/2) H_{q-1} \\ &= b_\uparrow' (\hat{\hat{\Pi}}_x)^q \hat{\hat{R}}_z\left((-)^q \pi/2\right) H_0 + b_\downarrow' (\hat{\hat{\Pi}}_x)^{q-1} \hat{\hat{R}}_z\left((-)^{q-1}\pi/2\right) H_0 \\ &= b_\uparrow' \hat{\hat{\Pi}}_x^q \hat{\hat{\Pi}}_z^q \mathcal{H}_{\mathrm{qd}} + b_\downarrow' \hat{\hat{\Pi}}_x^{q-1} \hat{\hat{\Pi}}_z^{q-1} \mathcal{H}_{\mathrm{qd}} \end{aligned} \tag{3.65}$$

with $\mathcal{H}_{\mathrm{qd}} = \hat{\hat{R}}_z(\pi/2) H_0$. This corresponds to the interaction frame Hamiltonian

$$\begin{aligned}\tilde{\mathcal{H}}_{\mathrm{rf,quad}}(t_q) &= \hat{\hat{R}}_z(2q\phi_0)\, \hat{\hat{S}}_0^\dagger \left\{ b_\uparrow' \hat{\hat{\Pi}}_z^q + b_\downarrow' (\hat{\hat{\Pi}}_x^\dagger) \hat{\hat{\Pi}}_z^{q-1} \right\} \mathcal{H}_{\mathrm{qd}} \\ &= \hat{\hat{R}}_z(2q\phi_0)\, \hat{\hat{S}}_0^\dagger \sum_{\mu=\pm 1} (-)^{q\lambda} \left\{ b_\uparrow' \omega_{1\mu}(t_0) + b_\downarrow' \omega_{1-\mu}(t_0) \right\} T_{1\mu} \\ &= \sum_{\mu=-1}^{1} \left\{ b_\uparrow' \tilde{\omega}_{1\mu}^{\mathrm{rf}}(t_0) + b_\downarrow' \tilde{\omega}_{1\mu}^{b,\mathrm{rf}}(t_0) \right\} T_{1\mu} \exp\left\{ -i \frac{2\pi q}{N} \left(\mu\nu + \lambda \frac{N}{2}\right) \right\} \end{aligned} \tag{3.66}$$

since the $\mu = 0$ component is missing in the second step and we replaced μ with λ in $(-)^{q\mu}$, so

$$\mathcal{S}' = \begin{cases} 0 & \mu\nu \neq \frac{N}{2} Z_\lambda \\ 1 & \mu\nu = \frac{N}{2} Z_\lambda \end{cases} \tag{3.67}$$

More generally, the effective π rotation can be described as $\mathrm{R} = (\beta_1)_{\alpha_1}(\beta_2)_{\alpha_2}$, with different flip angles and phases, constant amplitude and respectively of duration τ_1 and τ_2, as described in Fig. 3.3 (R elements containing three or more pulses can be described similarly).

The first of the two pulses in the q-th R element, whose Hamiltonian is labelled $H_q^{①}$, is influenced by the phase of the last pulse in the $(q-1)$-th R element, while the second (or any more) pulse in R_q, associated with $H_q^{②}$, is only influenced by the previous pulse in the same element, without any additional phase alternation: $H_q^{②}$ depends only upon H_q, while $H_q^{①}$ contains both H_q and H_{q-1}.

$$\mathcal{H}^{\epsilon}_{\mathrm{rf,real}}(t_q) = \begin{cases} H_q^{①} = \hat{\hat{\Pi}}_x^q \left\{ b_\uparrow \hat{\hat{R}}_z(\alpha_1) + b_\downarrow \hat{\hat{\Pi}}_x \hat{\hat{R}}_z(\alpha_2) \right\} H_0 \\ H_q^{②} = \hat{\hat{\Pi}}_x^q \left\{ b_\uparrow \hat{\hat{R}}_z(\alpha_2) + b_\downarrow \hat{\hat{R}}_z(\alpha_1) \right\} H_0 \end{cases}$$

For an R element made up of more than 2 pulses, all intervals after ① resemble ②. This can be simplified as

$$\tilde{\mathcal{H}}^{\epsilon}_{\mathrm{rf,real}}(t_q) \;=\; \begin{cases} H_q^{①} = \hat{\hat{R}}_z(2q\phi_0)\;\hat{\hat{S}}_0^{①,\dagger}\;\left\{b_\uparrow \hat{\hat{R}}_z(\alpha_1) + b_\downarrow \hat{\hat{\Pi}}_x \hat{\hat{R}}_z(\alpha_2)\right\} H_0 \\ H_q^{②} = \hat{\hat{R}}_z(2q\phi_0)\;\hat{\hat{A}}_0^{①,\dagger}\;\hat{\hat{S}}_0^{②,\dagger}\;\left\{b_\uparrow \hat{\hat{R}}_z(\alpha_2) + b_\downarrow \hat{\hat{R}}_z(\alpha_1)\right\} H_0 \end{cases}$$

The terms in curly brackets give rise to a z rotation of the spin operators in H_0 *and* affect its magnitude differently. Both terms can be written in closed form introducing a time dependent coefficient $f_{\mu,\alpha_1,\alpha_2}(t_0)$ which *only* depends on the specific time point considered within each R element but does not otherwise affect the selection rules:

$$\tilde{\mathcal{H}}^{\epsilon}_{\mathrm{rf,real}}(t_q) \;=\; \sum_{\mu=-1}^{1} f_{\mu,\alpha_1,\alpha_2}(t_0)\, T_{1\mu} \times \exp\left\{-\frac{i2\pi q\,\mu\nu}{N}\right\}$$

For the quad term,

$$\begin{aligned} \mathcal{H}^{\epsilon}_{\mathrm{rf,quad}}(t_q) \;&=\; \begin{cases} H_q^{①} = \hat{\hat{\Pi}}_x^q \hat{\hat{\Pi}}_z^q \left\{b'_\uparrow \hat{\hat{R}}_z(\alpha_1) + \; b'_\downarrow \hat{\hat{\Pi}}_x \hat{\hat{\Pi}}_z \hat{\hat{R}}_z(\alpha_2)\right\} \mathcal{H}_{\mathrm{qd}} \\ H_q^{②} = \hat{\hat{\Pi}}_x^q \hat{\hat{\Pi}}_z^q \left\{b'_\uparrow \hat{\hat{R}}_z(\alpha_2) + b'_\downarrow \hat{\hat{R}}_z(\alpha_1)\right\} \mathcal{H}_{\mathrm{qd}} \end{cases} \\ &=\; \begin{cases} H_q^{①} = \hat{\hat{R}}_z(2q\phi_0)\;\hat{\hat{S}}_0^{①,\dagger}\;(-)^{q\lambda}\left\{b'_\uparrow \hat{\hat{R}}_z(\alpha_1) + b'_\downarrow \hat{\hat{\Pi}}_x \hat{\hat{\Pi}}_z \hat{\hat{R}}_z(\alpha_2)\right\} \mathcal{H}_{\mathrm{qd}} \\ H_q^{②} = \hat{\hat{R}}_z(2q\phi_0)\;\hat{\hat{A}}_0^{①,\dagger}\;\hat{\hat{S}}_0^{②,\dagger}\;(-)^{q\lambda}\left\{b'_\uparrow \hat{\hat{R}}_z(\alpha_2) + b'_\downarrow \hat{\hat{R}}_z(\alpha_1)\right\} \mathcal{H}_{\mathrm{qd}} \end{cases} \\ &=\; \sum_{\mu=-1}^{1} f_{\mu,\alpha_1,\alpha_2}(t_0)\, T_{1\mu} \times \exp\left\{-i\frac{2\pi q}{N}(\mu\nu + \lambda\frac{N}{2})\right\} \end{aligned}$$

The interaction frame Hamiltonian obeys the same symmetry-based selection rules as we obtained with a simple Π_x pulse, Eqs. 3.64 and 3.67. The use of a composite AM pulses affects the size of the average Hamiltonian by removing some of the $\mu = 0$ components but does not change the first-order selection rules. Higher order effects may be important. Also the size and form of the transient will affect the actual performance of the sequence, but not its symmetry-based properties.

Fig. 3.4 shows a simulation of the amplitude and phase of the rf field in the coil during the first two R elements of the $\mathrm{R14}_2^6$ sequence and with the composite pulse $\mathrm{R}=90_0\;270_\pi$ using for a realistic case and are shown in Fig. 3.4(b) and (c). More details on these simulations are to be found in Paper II.

3.8.3 Phase Modulation Transients

Let us consider a different kind of transients which affect the way the the rf field is modulated, as

$$\phi(t) = \phi_0 + \phi^{(0)} \cos(m\omega_r t + \phi^{(1)}) \tag{3.68}$$

where ϕ_0 is the exact phase, ϕ^0 is a small, transient deviation (i.e., $\phi^0 < \pi/4$). This type of modulation has been shown to be responsible for certain artifacts in rotary

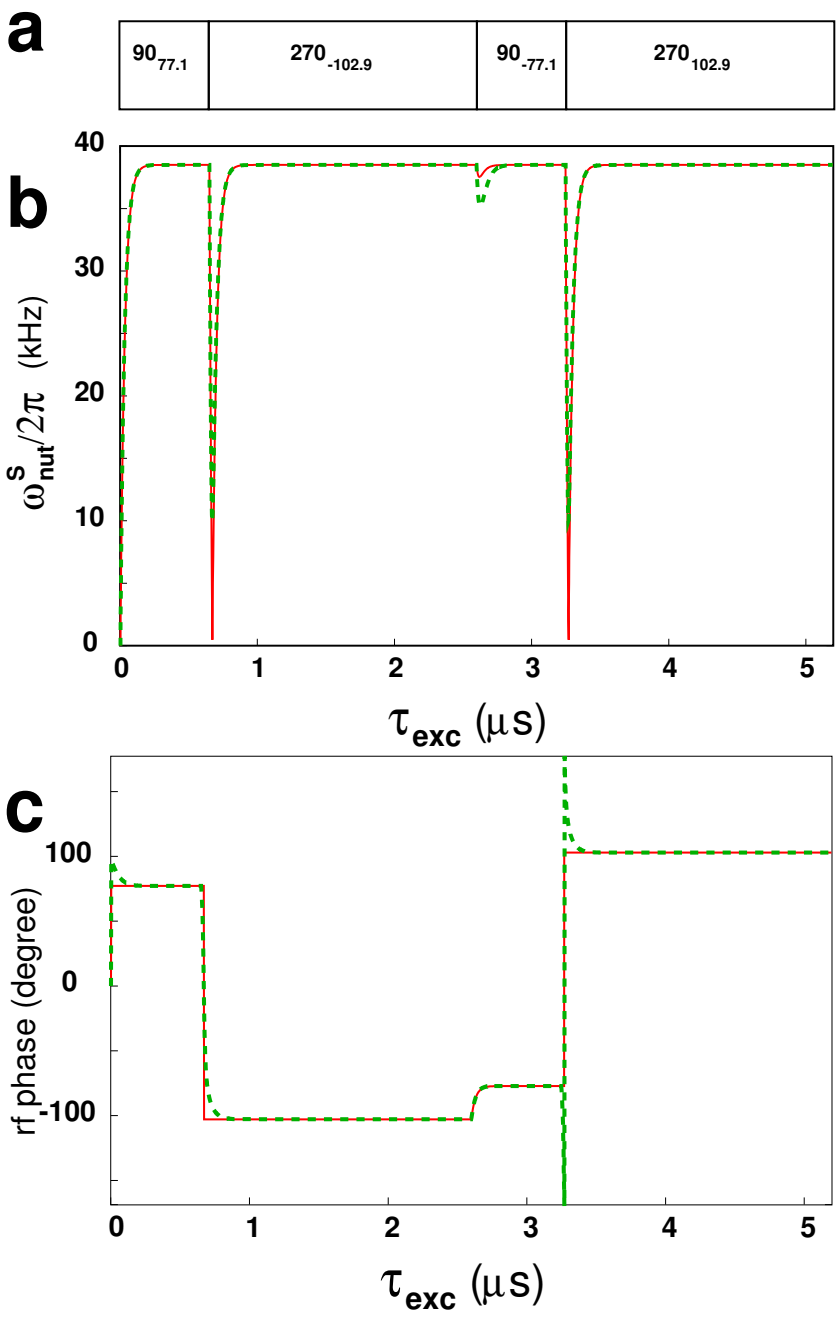

Figure 3.4: (a) The first two elements of a $R14_2^6$ sequence. (b) Rf field amplitude in the coil for an exact match of the coil natural oscillation frequency and the rf frequency (no quadrature transient, solid line) and for a tuning offset of 200 kHz (small quadrature transient, dashed line). (c) Phase of the rf field in the coil under the same conditions.

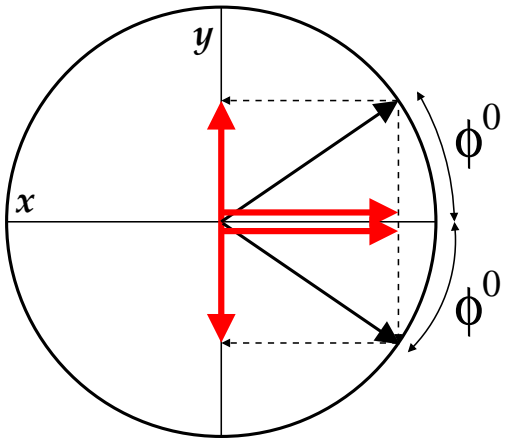

Figure 3.5: The x axis is defined as the expected direction of the rf field and the deviation from idealitity gives rise to a parallel component always positive and a negative component with zero average.

resonance recoupling experiments.[79] The rf field at any time can be decomposed as

$$\begin{aligned}\mathcal{H}_{\mathrm{rf}}(t_q) &= \hat{\hat{R}}_z(\phi^{(0)}\cos(m\omega_r t_q + \phi^{(1)}))\,\mathcal{H}^0_{\mathrm{rf}}(t_q) \\ &= \hat{\hat{R}}_z(\phi^{(0)}\cos(m\omega_r t_0 + \frac{2\pi nm}{N}q + \phi^{(1)}))\,\mathcal{H}^0_{\mathrm{rf}}(t_q)\end{aligned} \tag{3.69}$$

This can not be separated into two parts to apply average Hamiltonian theory, but the resulting field is still in the xy plane. As represented in Fig. 3.5, the "exact" direction is labelled as x for convenience and $\pm\phi^0$ gives the maximum deviation from it. If we project $\mathcal{H}_{\mathrm{rf}}$ onto the x axis, the parallel components is always reduced but always consistently positive, while the orthogonal component oscillates around zero between positive and negative values, therefore it has a vanishing average and we neglect it. Based on this approximation, we can put our problem into an easier form for analytical manipulation:

$$\begin{aligned}\mathcal{H}^{\mathrm{imp}}_{\mathrm{rf}}(t_q) &= -\phi^{(0)}\,e^{i(m\omega_r t_q+\phi^{(1)})}\,\mathcal{H}^0_{\mathrm{rf}}(t_q) \\ &= -\phi^{(0)}e^{i(m\omega_r t_0+\phi^{(1)})}\exp\left\{i\frac{2\pi mn}{N}q\right\}\left(\hat{\hat{\Pi}}_x\right)^q\mathcal{H}^0_{\mathrm{rf}}(t_0)\end{aligned}$$

corresponding to the interaction frame Hamiltonian

$$\begin{aligned}\tilde{\mathcal{H}}_{\mathrm{rf}}(t_q) &= \phi^{(0)}e^{i(m\omega_r t_0+\phi^{(1)})}\exp\left\{i\frac{2\pi mn}{N}q\right\}\hat{\hat{R}}_z(2q\phi_0)\hat{\hat{S}}_0^{\dagger}\mathcal{H}^0_{\mathrm{rf}}(t_0) \\ &= \phi^{(0)}e^{i(m\omega_r t_0+\phi^{(1)})}\sum_{\mu=-1}^{1}\tilde{\omega}'^{\,\mathrm{rf}}_{1\mu}(t_0)\,T_{1\mu}\,\exp\left\{-\frac{i2\pi q}{N}(\mu\nu-mn)\right\}\end{aligned} \tag{3.70}$$

and the selection rule becomes

$$\mathcal{S}' = \begin{cases} 0 & \mu\nu - mn \neq NZ \\ 1 & \mu\nu - mn = NZ \end{cases} \qquad Z = \text{integer} \tag{3.71}$$

3.8.4 First Order Average Hamiltonian in a Model Case

Now that we have summarised the first order selection rules for the spin Hamiltonian and the rf transients, it is useful to consider a common sequence, like $\mathrm{R14}^6_2$,

and consider explicitly which terms will be present to first order. For instance, the sequence used for distance measurements, $R14_2^6$ with $R^0{=}90_0\ 270_{180}$, uses amplitude modulated rf fields. This is compensated *to first order* for all the transients described in the previous sections ($\pm 6 \neq 7{\times}Z$, with $Z \in \mathbb{N}$ and $\pm 6 - 2m \neq 14{\times}Z$).

Chapter 4

Homonuclear Dipolar Recoupling of $^{13}C_2$ Pairs and Applications

4.1 Introduction

One of the key goals of this work is to illustrate how to use rotor-synchronized sequences to measure distances between two nuclei of the same species with high precision. Paper II introduces a new approach for ^{13}C-^{13}C distance determination for directly bonded carbon atoms, as well as for medium-distance determination. The typical C-C distance range for different bond orders is shown in Fig. 4.1. From these figures, it is apparent that an accuracy of at least 5 pm is necessary in order to study bond conjugation. The precision of the diffraction measurement is related to the quality and the size of the crystals which can be obtained. For good crystals of small molecules, it is often possible to localize carbon atoms and other relatively heavy atoms with X-ray diffraction with a precision of about 1 pm or better. For larger molecules containing thousands or millions of atoms, the resolutions seldom gets below a threshold of 15 pm to 20 pm, it may be even difficult to distinguish small molecules like water from cations with a similar electron density. This is often the case in many structural determinations of biomolecules, where the common resolution is of the order of 10 pm to 30 pm. Under such conditions, it is possible to get a clear picture of the overall molecular structure and on how various fragments are related to each other, but nothing can be said about bond-lengths.

The precise estimation of distances between carefully-chosen pairs of nuclear spins allows the elucidation of important mechanistic details. Such applications require the construction of robust sequences for exciting DQ coherences. Other features, like the dependence upon CSA amplitude and orientation also determine achievable DQ efficiency as well as the long-term behaviour of the DQ build-up curve. The task of measuring distances is of central importance in NMR, both in

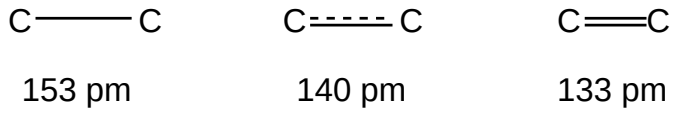

Figure 4.1: typical distances between directly bonded carbon atoms

homonuclear and heteronuclear spin systems. When dealing with solid-state NMR on rotating solids, it is essential to use methods which recouple the interaction which is normally suppressed completely or partly by the sample rotation at the magic angle. There is no unique answer to what is the best approach for measuring distances, since it depends on many parameters related both to the specific system under investigation and to the experimental setup.

For instance, when working with biological solids it is desirable to operate in "mild" conditions, both in terms of spinning speed and rf power, in order to minimize the physical and thermal stress on the sample, which might otherwise decompose. On the other hand, for many other organic and inorganic compounds there is no such constraint and the use of high spinning speeds is preferable, due to a better suppression of CSA and of all terms related to second-rank tensors.

For measuring distances between homonuclear pairs, some well established methods exploit: (i) ZQ-recoupling (rotational resonance[32,36]), (ii) transverse magnetization exchange between the two sites of interest (DRAWS[80–83] and RFDR[84,85]) and (iii) DQ recoupling methods.[9,65,86]

DRAWS, for instance, is widely used for medium and longe-range distance measurements and is therefore the most common method, together with rotational resonance, for homonuclear long-range distance measurements. The main limitation of DRAWS for short distance measurements is related to its limited time resolution, which limits the sampling of the fast dipolar oscillation. The method we propose here is intended for precise bond-length measurements and is not meant to compete with the techniques mentioned above for measuring internuclear distances above about 3Å, due to the unsatisfactory CSA compensation of the R sequences tested so far at long excitation times.[87] However, the situation may change as the understanding of supercycled sequences advances.

4.2 Pulse Sequence for Distance Measurement

The sequence used for homonuclear distance measurements is shown in Fig. 4.2 and is fully described in Paper II. Enhanced carbon magnetization is created via ramped-CP, then it is transferred into longitudinal magnetization by a $\pi/2$ pulse. At this point, an $\mathrm{R}N_n^\nu$ sequence for pure DQ dipolar recoupling is applied for an interval τ_{exc} to generate DQ coherences. The DQ state is then reconverted back in the following interval with an R sequence of duration τ_{rec}, phase shifted by 90° with respect to the excitation block. Finally, the DQ filtered spectrum is acquired after a $\pi/2$ reading pulse. Additionally, in order to avoid phase distortion in the DQF spectra, it is advisable to include a z-filter by introducing a short delay of free evolution, or an extra level of phase cycling.

In our case, the experiment aims at determining distances and so the sequence is repeated for different values of the excitation and/or reconversion intervals. The set of DQF efficiencies plotted against the duration of the $\mathrm{R}N_n^\nu$ sequence is called a "build-up" curve. There is no need for τ_{exc} and τ_{rec} to be equal. On the contrary, it is convenient to acquire a DQF build-up curves with the asymmetric scheme, resulting in a much wider dynamic range and in a shortening of the irradiation time. Fig. 4.3 gives the experimental comparison between the build-up curve for

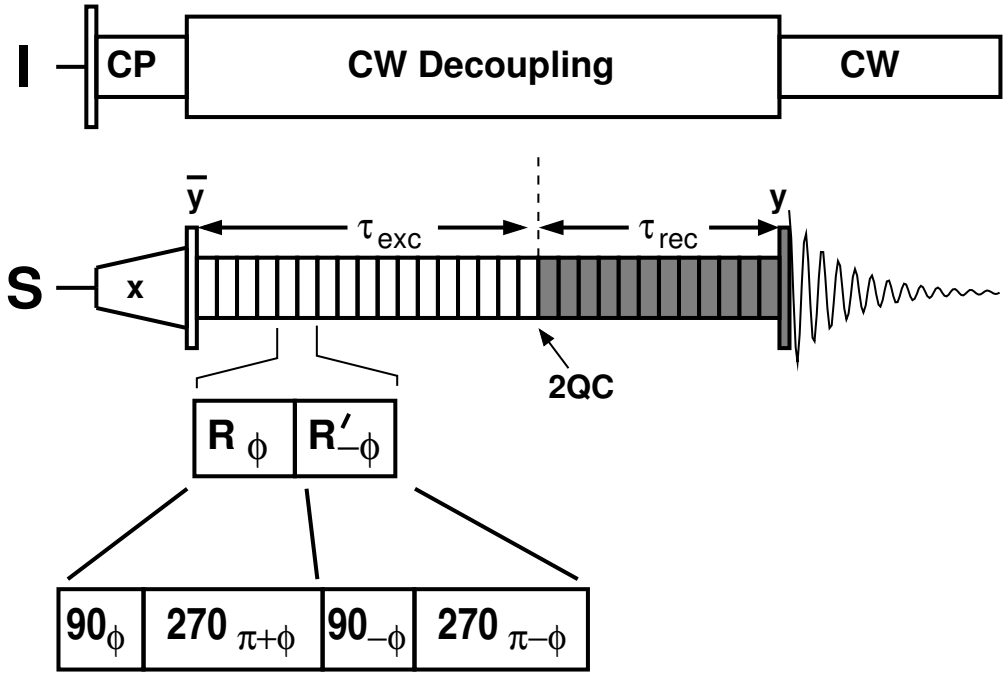

Figure 4.2: Pulse sequence for excitation of DQ coherences and for distance measurement. The duration of the excitation and reconversion periods (shaded block) are not necessarily equal. The shaded block is subjected to phase cycling in order to select the DQ coherence at the end of the excitation period and transfer it into longitudinal magnetization. CW decoupling is applied during the recoupling sequence and acquisition. In our experiment, the I channel denotes ^{1}H irradiation while the S channel denotes ^{13}C.

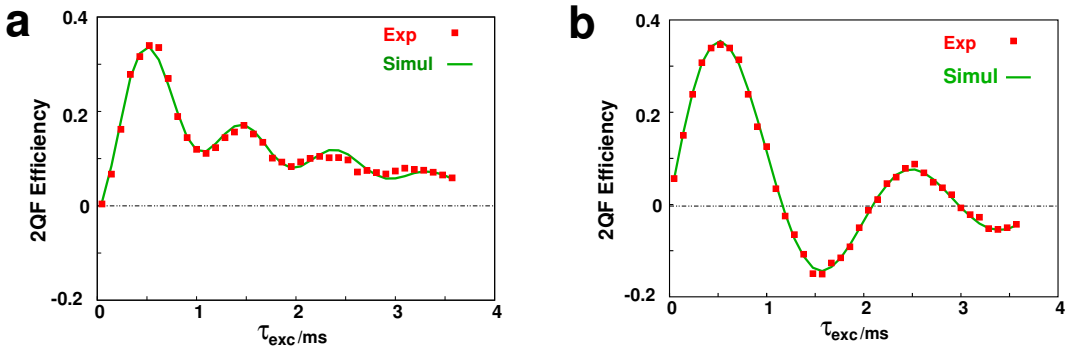

Figure 4.3: Experimental ^{13}C DQF efficiencies for [2,3-$^{13}C_2$]-*L*-alanine at 9.4 T and a spinning frequency $\omega_r/2\pi$=6.0 kHz, together with the best fit simulations, using $R14^6_2$ (a) Symmetric procedure ($\tau_{\text{exc}} = \tau_{\text{rec}}$). (b) Asymmetric procedure (τ_{rec}=523.8 μs).

the symmetric excitation and reconversion ($\tau_{\text{exc}} = \tau_{\text{rec}}$) and for the asymmetric case ($\tau_{\text{exc}} \neq \tau_{\text{rec}}$). In this respect, it is convenient to select symmetries which give rise to wide oscillations in the build-up curve. The symmetries which have been used for distance measurement correspond to the rotational numbers $(l, m, \lambda, \mu) = (2, -1, 2, 2)$ and $(2, 1, 2, -2)$. The resulting signal in the DQF spectrum for a pair of dipolar coupled spins is modulated as

$$\sin(\omega_D^{ij}\tau_{\text{exc}})\sin(\omega_D^{ij}\tau_{\text{rec}}) \tag{4.1}$$

using a first-order average Hamiltonian model and with ω_D^{ij} being the dipolar coupling constant between spins i and j, expressed in angular units.

$$\omega_D^{ij} = \sqrt{6}\, b_{ij}\, \kappa_{2-122}\, D^2_{0-1}(\Omega^{ij}_{PR})\, e^{i(\alpha^0_{RL}+\omega_r t^0)} \tag{4.2}$$

$$\kappa_{2-122} = d^2_{-10}\left(\beta^{RL}\right)\tau_R^{-1}\int_{t_0^0}^{t_0^0+\tau_R} D^2_{20}(\Omega_{\text{rf}}(t))e^{-i\omega_r t}dt \tag{4.3}$$

where b_{ij} is the dipolar coupling constant, defined in Eq. 2.58, while the scaling factor κ depends upon the selected symmetry and basic element.[72] Even though a simple π pulse corresponds to high scaling factor, most often the requirement for a broadband excitation makes it more convenient to use composite pulses.[9,65]

The same scheme presented in Fig. 4.2 can be used with a variety of sequences for pure dipolar DQ excitation other than RN^ν_n sequences but we found that choosing an RN^ν_n sequence is advantageous when dealing with strongly coupled ^{13}C-^{13}C systems due to their robustness for short recoupling times. Once the DQ state is generated, it can be manipulated for several purposes to study the local molecular environment. For instance, the DQ state can be exploited to measure a torsion angle around the dipolar vector by adding a period during which the DQC is allowed to evolve under the influence of its couplings to neighboring nuclei (see Sect. 4.5). It can be a part of a experiment designed in getting the proximities between active nuclei, to aid the assignment of complex spectra. It can be used as starting point towards the excitation of higher order coherences.[68]

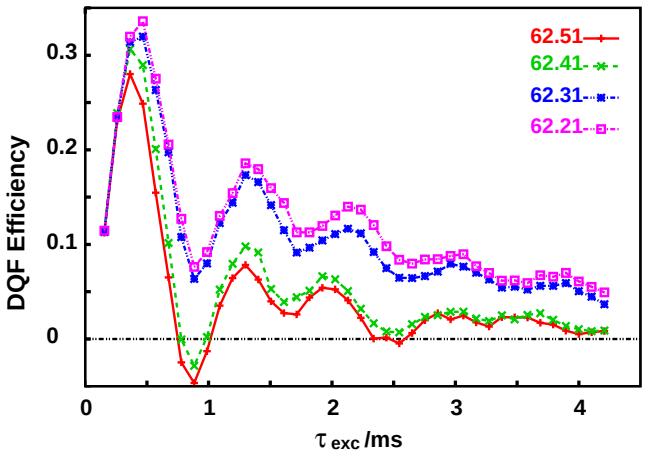

Figure 4.4: Diamonium-[2,3-$^{13}C_2$]-fumarate at 4.7 T and $\omega_r/2\pi$=11.85 kHz using $R26_8^9$. The phase is adjusted around the theoretical value $\phi_0 = 62.31°$. Note the extremely high sensitivity to the value of this phase shift. The rather irregular dependence on the phase shift may reflect the limited phase resolution of the hardware.

4.3 Distance Measurements on Model Systems

RN_n^ν sequences are rather robust with respect to variations in magnitude and orientation of the CSA tensor, when applied for bond-length measurements. This is an important feature because the exact details of the CSA tensor magnitude and orientation are not known in many interesting systems and it is desirable to get a distance estimate which does not depend much on unknown parameters.

To increase DQ efficiency and reduce the discrepancy between the theoretical 73% limit and the simulated efficiency, we compared the ideal first-order RN_n^ν Hamiltonian at the end of a full block of N contiguous R elements (ideally equal to $\mathbb{I}$) with the one obtained through numerical simulation on one- and two-spin systems. It emerged that one of the terms in the real Hamiltonian which affects the sequence performance is a z-rotation, or more generally a $T_{\lambda 0}$ tensor, which accumulates period after period. Many such terms can be identified as allowed in $\bar{\mathcal{H}}^{(2)}$. Since each R element gives rise to a π rotation *and* a z-rotation, an obvious way to partly compensate for this problem is to alter the phase of the R element in such a way as to cancel out the two terms. Tiny phase adjustments can improve the short and long-term behaviour of the DQ build-up curve. Experiments confirmed this effect, as shown in Fig. 4.4. In practice, a few curves are monitored in order to establish the optimal phases, all recorder with $\tau_{\rm exc}$=$\tau_{\rm rec}$ (see Fig. 4.5). The aim is to select the phase that makes the *entire* symmetric build-up curve positive, not simply to maximize the DQ-filtering efficiency at short times. Another approach for removing $T_{\lambda 0}$ terms from $\bar{\mathcal{H}}^{(2)}$ relies on a supercycle of the form $\mathcal{C}^\nu\mathcal{C}^{-\nu}$. Unfortunately, such a supercycle removes those terms at the expenses of the γ-encoding. The $\nu\ -\nu$ supercycle has been applied successfully in RN_n^ν sequences for ZQ recoupling,[76] which are not γ encoded in any case. This supercycle has also been used in DQ recoupling experiments for weakly coupled systems[88] without any significant loss in DQF efficiency.

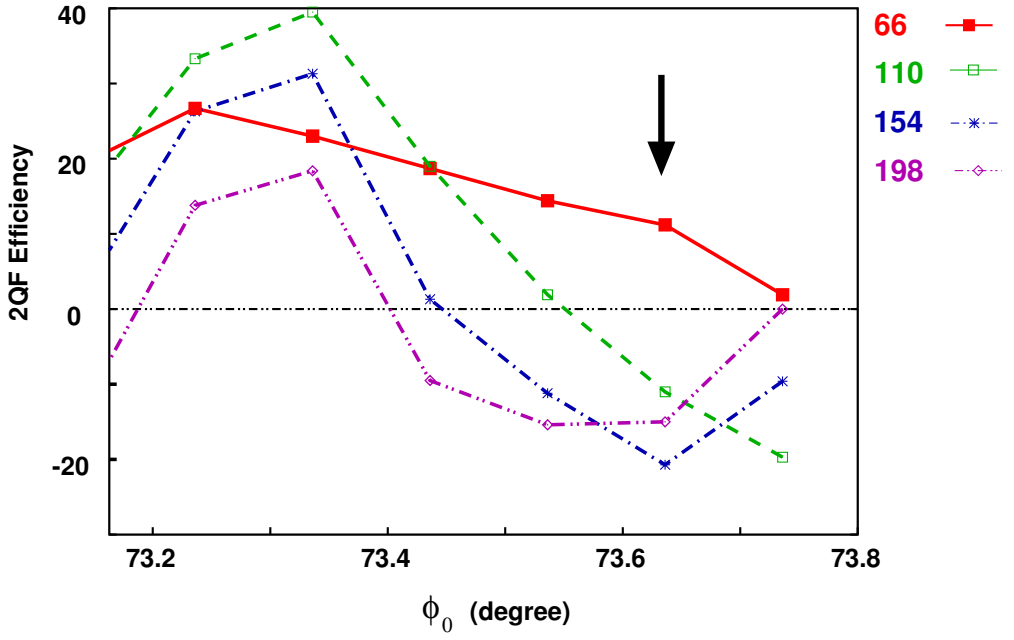

Figure 4.5: Experimental DQ-filtering efficiency using $R22_4^9$ on 11,2-[$^{13}C_2$]-all-*E*-retinal at 9.4 T and 5.5 kHz, as a function of the phase. Each curve corresponds to a different number of R elements (indicated in the legend) and the arrow marks the phase value corresponding to exact $R22_4^9$ symmetry. Note the extremely high phase sensitivity for large numbers of elements.

For ^{13}C-^{13}C distance measurements we use a symmetry-based sequence for excitation of pure double-quantum coherence between the two labelled nuclei, while averaging out all other interactions. By changing the duration of the DQ excitation and/or reconversion sequence, it is possible to relate the shape of the build-up curve to the dipolar coupling between the labelled pair. The selection of a specific interaction in the first-order average Hamiltonian is possible by a proper choice of the symmetry numbers, but the real performance of the sequence depends also on experimental imperfections and on the behaviour of higher order terms in the average Hamiltonian, as discussed in Sect. 3.6. The number of higher-order terms can be further reduced by supercycles, expecially for medium-range distances which involve more than just a few *ms* of DQ irratiation, but it is not sufficient by itself to establish the optimal sequence. Hence the necessity to compare simulations with the experimental performance. Additionally, the maximum DQ efficiency is only one of the parameters which needs to be taken into account. As shown in Paper I and II it is essential to have a well behaved sequence with respect to rf offset and amplitude missets. In Paper II the symmetries $R14_2^6$ and $R22_4^9$ are successfully used to estimate ^{13}C-^{13}C distances with an accuracy of 5 pm or better.

The results on bond-length and medium-range distance measurement are summarized in Fig. 4.6. These are the "pure" NMR data with the corresponding error bars, with the assumptions that the nuclei are fixed in space. In reality, the molecules undergo vibrational motions and the bond lengths estimated by NMR suffer of a systematic overestimate error of about 1 to 4 pm, as a result of motional averaging.[89] For the shorter distances, we observe a consistent 2.3 ± 1.1 pm dis-

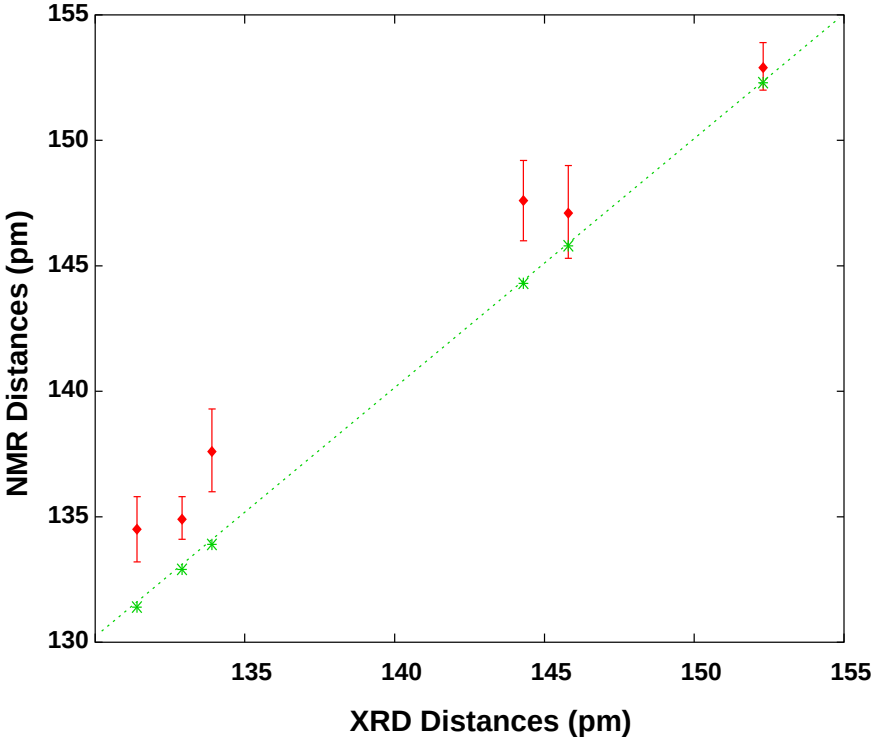

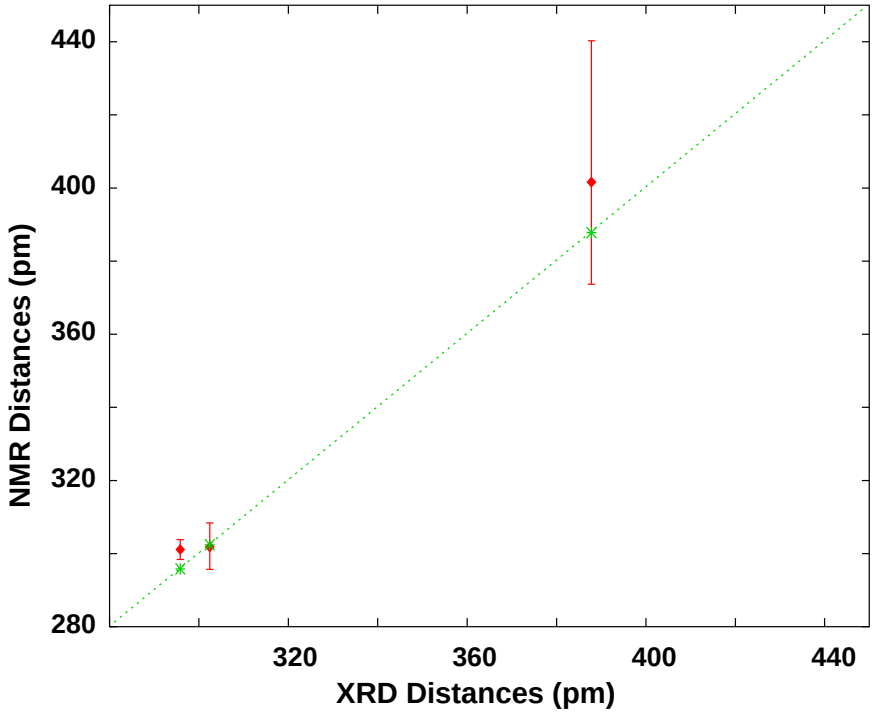

Figure 4.6: The NMR distances (filled diamonds) are plotted together with their error bars against the XRD data (asterisk). On the left hand side, we have the bond-length measurements on a set of 6 reference compounds (data from Paper II). As can be been, the NMR distance is always above the dotted line passing through the XRD data, indicating the presence of a systematic overestimate of the internuclear distances by 2.3 ± 1.1 pm. The right-hand side shows medium-range distance measurements. The precision of this method is poor for distances above 350 pm.

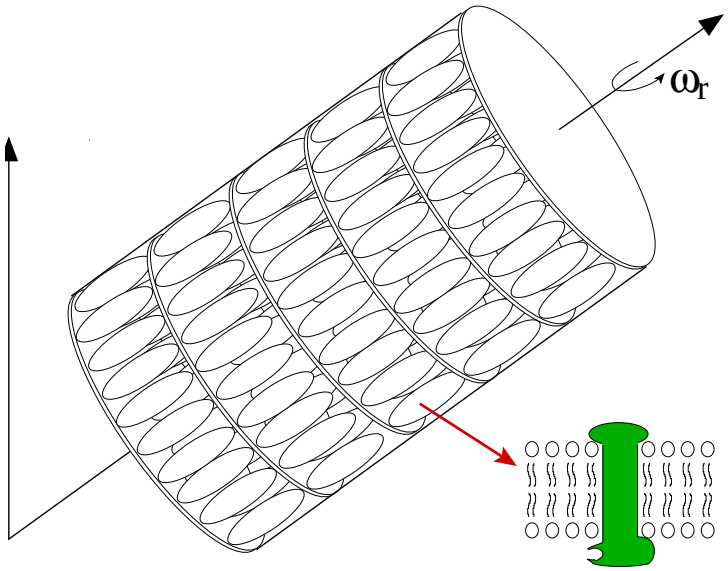

Figure 4.7: Scheme of the rotor with an alligned sample in it. The sample (typically a biomembrane) is allinged on disks within the rotor and spun at the magic angle

crepancy between the solid-state NMR estimate and the X-ray diffraction (XRD) distance, which is attributed mainly to vibrational effects and is consistent with Ref. 89. Part of the discrepancy may also be due to J-anisotropy, but this contribution is expected to be very small (< 5 Hz) for ^{13}C-^{13}C J interactions.[90]

4.4 Dipolar Recoupling on Oriented Samples

Most of the experiments discussed so far involve powder samples, i.e., the sample is made up of a myriad of crystallites with random relative orientations. Another interesting case occurs when dealing with samples which are aligned with respect to some direction. This is the case when dealing with liquid crystals, for example, where the magnetic field can induce the molecules to align in some special direction with respect to it. In other cases the alignment can be forced onto the sample by mechanical means. In the past few years a new methodology has been introduced by Glaubitz and Watts, named Magic-Angle-Oriented-Sample-Spinning (MAOSS),[91,92] in which the sample, made up of well ordered biomembranes, is aligned on thin glass dishes which are stacked on top of each other within the rotor. The membrane normal tends to be orthogonal to the glass plates and this gives macroscopically ordered samples, as depicted in Fig. 4.7. In general, the spinning of the sample is a disturbance for the molecular alignment and therefore only moderate spinning speeds can be used (i.e., below 6 kHz). The level of macroscopic order is estimated by monitoring the ^{31}P signal in the polar head group of the lipid bilayers. The shape and width of this ^{31}P signal reflects directly the alignment level and measures the mosaic spread is in the sample.

Once the orientation of the sample with respect to the rotor axis is known, the measurements of some well-chosen NMR interactions can give insight into the orientation of the selected molecular fragment with respect to the rest of the

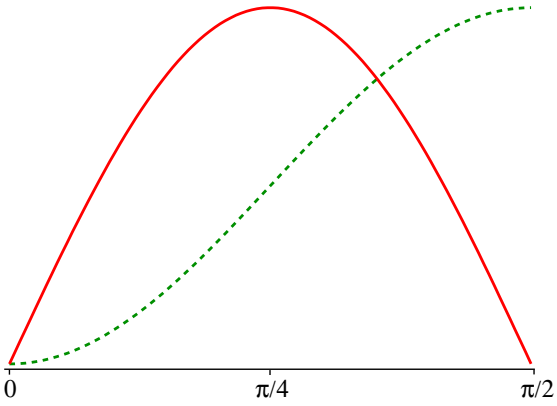

Figure 4.8: Angle dependence of the reduced Wigner matrix elements determining the behaviour of some DQ recoupling sequences, as $\sin 2\beta$ for $m = 1$ (solid line) and $\sin^2 \beta$ for $m = 2$ (dotted line).

molecules. This method has been applied to many interesting systems.[93–95] In particular, the quadrupolar interaction has been used in specifically labelled ^{2}H proteins to provide precise orientation information. Now several groups are implementing this technique and MAOSS is becoming a more common experiment.

In this context, it is possible to devise experiments that exploit dipolar recoupling to measure the orientation of molecular fragments. These experiments require a knowledge of the internuclear coupling, therefore it is convenient to use both unoriented and oriented samples, to get the precise internuclear distance from the first *and* orientational information from the second.

The recoupling sequence must be chosen so as to allow an unambiguous determination of the orientation. It is possible to use symmetry arguments to obtain a recoupling sequence with the derired first-order average Hamiltonian. All recoupling sequences listed in Paper II do *not* fulfil this requirement, since the pure dipolar DQ recoupling sequences which recouple $(l, m, \lambda, \mu) = (2, -1, 2, 2)$ and $(2, 1, 2, -2)$ involve the reduced Wigner matrix element $d^2_{21}(\beta)$ which has an angular dependence of the form $\sin(2\beta_{MR})$, according to the notation introduced in Sect. 2.6. This is not a monotonic function in the interval between 0 and $\pi/2$. On the other hand, symmetries which recouple terms $(l, m, \lambda, \mu) = (2, -2, 2, 2)$ and $(2, 2, 2, -2)$ depend on the β angle as $\sin^2 \beta_{MR}$. This is a good choice for pure DQ recoupling in oriented samples, as can be seen from Fig. 4.8.

There is no RN^ν_n sequence for pure DQ recoupling which involves the $m = \pm 2$ components, even though recoupling sequences for this particular DQ Hamiltonian *and* the CSA interaction are available. One possible way to get around this proplem would be to choose a sequence in this class and supercycle it to remove the CSA dependence (as shown in Sect. 3.7.1, this supercycle averages out interactions with odd spin components). Another approach is to look for a suitable solution within a different symmetry class: there are many CN^ν_n sequences with the desired transformation properties. Some preliminary results (see Paper III) have been achieved using the symmetry C8^3_1 and the element C=$90_0360_\pi270_0$ (see Paper III). The sequence performs well on the model compound and provides a reliable distance estimate. The method will be demonstrated on an oriented sam-

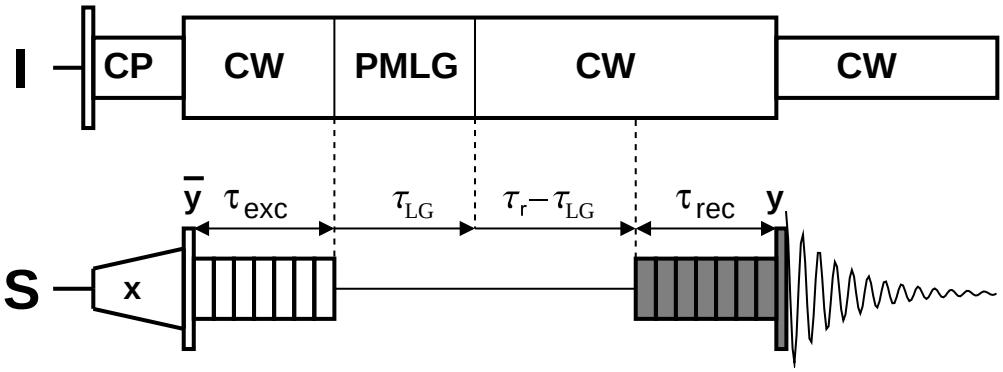

Figure 4.9: Pulse sequence for HCCH torsion angle determination

ple of bacteriorhodopsin, labelled with 10,11-$^{13}C_2$-all-*E*-retinal. This work is in progress.

4.5 Torsion Angle Measurements

The methodology for measuring one HCCH torsion angle using a correlated DQ state has been already described elsewhere[67] and here we just recall a few features to clarify the experimental results reported in the next chapter. The HCCH torsion angle determination consists of the following steps:

- create a DQ correlated state involving the two ^{13}C sites by DQ homonuclear dipolar recoupling
- let the DQ coherence evolve in presence of the heteronuclear CH couplings for a variable period of time
- convert back the DQ coherence into observable signal

The sequence is sketched in Fig. 4.9. For this application, τ_{exc}=τ_{rec} and they are kept fixed. In the DQ evolution period, we apply a homonuclear decoupling sequence, i.e., FSLG[44] or PMLG[49,50] for a time τ_{LG} and heteronuclear decoupling for $\tau_r - \tau_{LG}$. The choice of the most convenient homonuclear decoupling sequence depends on the spectrometer capabilities in terms of switching phase or frequency with sufficient speed. The signal corresponding to different t_{LG} values encodes the relative orientaion of the two heteronuclear dipolar vectors with respect to each other. The data set can be analysed to extract the HCCH torsion angle. This experiment has been applied to rhodopsin,[96] rhodopsin photointermediates[97] and bacteriorhodopsin.[98]

Chapter 5

NMR on Membrane Proteins

5.1 Membrane Proteins and G Protein Coupled Receptors

In nature, about 60% of the human genome is encoded via soluble proteins. The remaining are insoluble proteins and among them we have the prominent class of membrane protein, in which the protein is in contact with the cell membrane, either on the surface or more deeply. Thousands of structures of soluble proteins have been solved while only about 20 membrane protein structures are known. For membrane-bound proteins, the protein action and functions are strictly connected to their natural environment but unfortunately this makes the structure determination more complex, due to their limited solubility and to the difficulty of crystallizing the proteins without disruption of the plasma membrane. On the other hand, solution state NMR is not an appealing approach because the size of the protein limits the motions in solution, leading to very broad features which are difficult to interprete or exploit for structural investigation.

Membrane proteins are of great interest because they govern to a large extent the interaction of the cell with the outside-world, aiding the cell to perform all its functions. It is therefore important to get an idea of the position of the protein with respect to the membrane, as well as its structure, in order to understand how it works.

The cell membrane is made up of a lipid bilayer in which the apolar, hydrophobic tails of the phospholipids (one of the main components) converge towards the middle of the plasma membrane while the hydrophilic phosphate groups constitute the polar surface, as shown in Fig. 5.1. A protein can interact with the membrane while being fully outside (extrinsic), or it can be embedded into the membrane (intrinsic). Here we consider transmembrane proteins, i. e., the protein goes through the lipid bilayer and extends beyond it in both directions. There are two main arrangements of the polypeptide chain that constitute the transmembrane protein. In one, the portion of the chain the goes through the membrane is curled into one or more α helices which traverse the membrane, leaving the most hydrophilic segments outside of the lipid bilayer. Another arrangement is the so-called β-barrel, i.e., wide portions of the protein form β-sheets which curl to form the sides of a barrel. Deviations from this simplified model can be expected and no general structural description can be given for the protein portions outside the membrane,

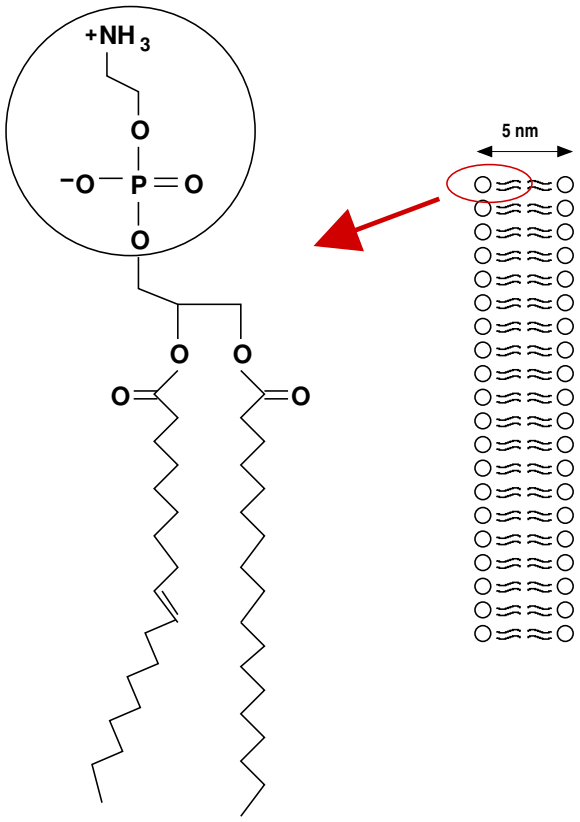

Figure 5.1: Scheme of a lipid bilayer. A typical phospholipid, the phosphatidyl ethanolamine (also known as cephalin), is shown on the left hand side. The long apolar aliphatic chains differ by the presence of one double bond, which affects their relative orientation. In the sketch of the cell membrane (right hand side), the wiggles represent the lipid chain pairs while the circles represent the polar end.

with highly variable structure. A first classification of membrane proteins is made in terms of their functions:

- the **transporters** aid the migration of ions or molecules through the lipid bilayer and in and out of the cell. The membrane on its own is impermeable to many molecules,
- the **linkers** work as an anchor, connecting the membrane to some specific molecule either inside or outside the membrane surface,
- the **enzymes** are highly selective catalysts for specific reactions,
- the **receptors** pass information to the cell about the outside world and regulate its response, by sending specific signals inside the cell.

There are many different kinds of membrane protein but we will only focus on the so-called G protein-coupled receptors (GPCRs). This means that the transmembrane protein is mechanistically coupled to another protein, called G protein, to carry messages across the cell membrane. The label "G" comes from the fact that the protein state is determined by the form of guanine nucleotide that it binds. In the pharmaceutical industry, many of the drugs being produced and developed have GPCRs as targets. Hence there is great interest not only in the general structure of GPCRs but also about the detailed structure of their active site. All GPCRs are seven-helix transmembrane bundles: the receptor protein forms α-helices, it passes through the cell membrane seven times and the helices

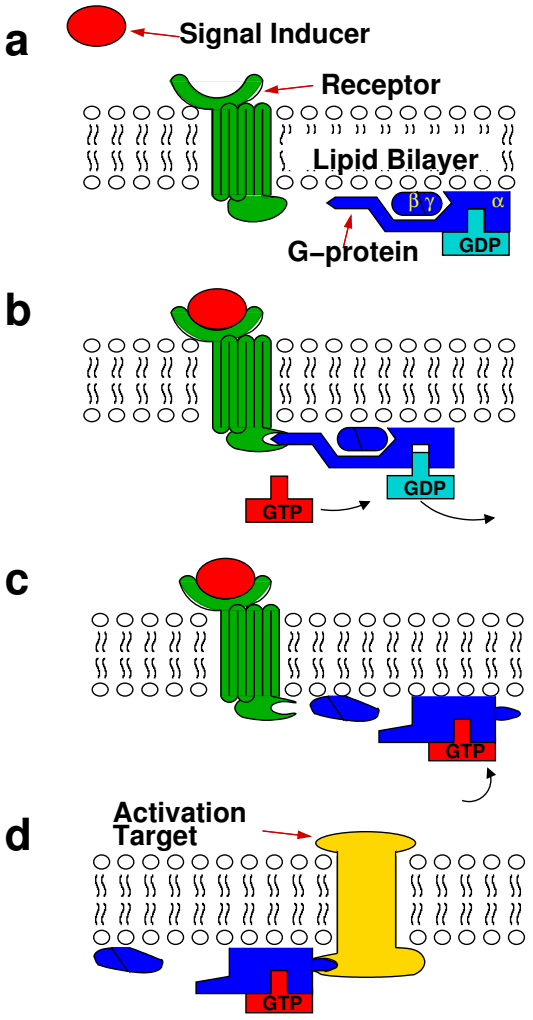

Figure 5.2: (a) Sketch of the protein receptor and of the G protein with respect to the lipid bilayer before activation (signalling molecule out of reach). The α, β and γ units of the G protein are labelled. (b) the signalling molecule reaches the receptor, which as a consequence modifies its shape (open mouth) and hence interacts selectively with the α complex of its own G protein, which starts releasing GDP. (c) GTP binds to the G protein, which dissociates and becomes active. (d) The activated G protein (in particular, the α subunit) interacts with the target protein, which sends further signals into the cell. After this step the GTP gets hydrolysed and the G protein returns to the state shown in (a). Each ativated receptor can activate hundreds of G protein molecules (Figure modified from Ref. 99).

coexist with non-helical regions (mostly outside the membrane). Within the cell, the corresponding G protein is inactive but it readily modifies its state when receiving a signal from its GPCR. All G proteins are characterized by two states, active and inactive. The G protein is made up of three units: an α unit, which is bound to the guanine complex, a β and γ unit.

The activation process of the G protein is sketched in Fig. 5.2. The G protein is drawn near the receptor in an inactive state (as it is bound to guanosinediphosphate, or GDP, Fig. 5.2a). When the receptor is activated (Fig. 5.2b), it is able to interact with the G protein. The G protein itself switches into an active state, by releasing GDP and binding guanosinetriphosphate (GTP), as shown in Fig. 5.2c. The activated G protein can now interact with the target protein (normally an ion transporter or an enzyme), which induces further reactions inside the cell. Both the activated α subunit or the activated $\beta\gamma$ complex can bind to the target protein, even though just the first case is shown in Fig. 5.2d. After this step, GTP gets hydrolyzed into GDP and the α subunit binds the $\beta\gamma$ complex, so that the G protein is finally deactivated and ceases stimulating intracellular signals. The GPCR is deactivated and set back to its initial form after some time, often due to the action of enzymes. For the sake of simplicity, Fig. 5.2 shows the interaction of the GPCR with just one G protein and one target protein. In reality, many G

proteins get activated after the signal enters the cell.

The activation mechanism involves three dimensional structural changes both in the receptor and in the G protein that induce biochemical signals inside the cell and initiates a cascade amplification, without the signalling molecule ever entering it. The activation of the target protein induces a chain of reactions inside the cell. The molecules moving within the cell to transfer the gathered information are conventionally called the second messengers and they can activate a wide variety of functions, by interacting with other proteins. We will look at the details of what happens for a specific case in the next section.

Given the importance of this kind of receptor for many cellular processes, a great interest in their structure is understandable. Normally the isolation of a transmembrane protein requires rather harsh methods and the disruption of the membrane. When the protein is membrane-free, its structure and 3D conformation may be different from the membrane-bound state, so the information content of this protein form is quite limited in the general case, unless otherwise proven. Unfortunately, it is often difficult to crystallize membrane proteins and only a handful of successful x-ray structure of membrane proteins are known. In most cases, the membrane protein structure is either unknown or known but with poor resolution. This background information can suffice as a basis for an NMR investigation of the protein's functions.

5.2 Rhodopsin

We now focus on a particular GPCR, rhodopsin, and describe its function in more detail. Rhodopsin is located in the retina, and consist of 348 amino acids that form seven α helices, for an overall size of 41 kDa (see Fig 5.3). The light receptor cells in the retina are of two kinds and are shaped as rods and cones. In both cases members of the rhodopsin family are responsible for the process controlling the light-absorption by the eye. Rhodopsin is formed from the opsin protein when this binds 11-Z-retinal. The conformational change in the receptor which is responsible for activating the G protein is due to a small conjugated molecule, the chromophore 11-Z-retinylidene, linked to the lysine residue Lys-296 as a protonated Schiff base (PSB).

Rhodopsin receives the signal by a photon (instead of a "signalling molecule") which is absorbed by the chromophore, with a quantum yield of 67%. The observed quantum yield is very high and also temperature independent. It corresponds to storage of about 60% of the photon energy, i.e., approximately 33 kcal/mol (or 146 kJ/mol) and the mechanism through which such a large amount of energy is stored in the photointermediates is not clear. The transmission of the signal further inside the membrane is initiated by a change of conformation in the chromophore from an 11-Z-retinal PSB to the all-*trans* isomer. Later in the cycle, the unprotonated Schiff base dissociates into opsin plus free all-trans-retinal, according to the cycle described in Fig. 5.4. The first step of vision takes place in 200 fs[101] and is one of the fastest known process in nature.

In the photoreceptor cell, the second messenger is a molecule called cyclic GMP (cGMP). The role of cGMP is to bind the Na^+ ion channels in the membrane in

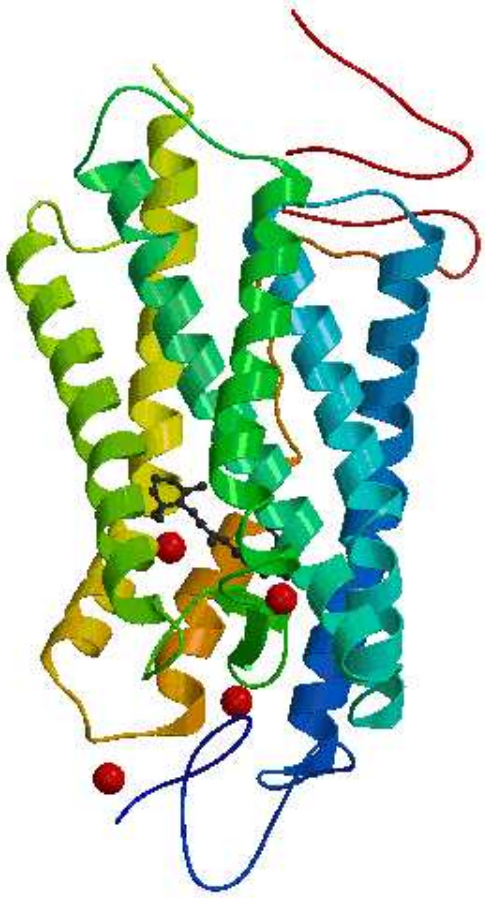

Figure 5.3: Ribbon representation of rhodopsin using the coordinates in the pdb file 1L9H based on XRD studies with 2.6 Å resolution.[100] Notice the position of the retinylidene chromophore (in black), attached to the seventh α-helix and the position of some water molecules (dark circles) in the neighbourhood of the chromophore.

order to keep them open. In the dark state, cGMP is generated continuously and the open channels guarantee an equilibrium between the cell and outside environment. After the light trigger, the metarhodopsin II receptor (M II) communicates with the heterotrimeric G protein transducin, which gets activated following the scheme discussed in the previous section. The activated α subunit sets into action another membrane protein, the cyclic nucleotide phosphodiesterase, which breaks cGMP into GMP. The decrease in the amount of cGMP in the photoreceptor cell shifts the internal equilibrium in a way that the cGMP bound to the ion channels dissociate and, as a consequence, the channels close. One rhodopsin can activate a few hundred molecules of transducin, and the level of amplification is higher at low light intensity. This generates a difference of potential between the cell and its environment of about 1 mV for one second, so that electrical impulses are sent to the brain along the optic nerves. This part of the visual process is well understood and more details can found in Refs. 102 and 103.

In the context of this thesis, further details on the intracellular reactions taking

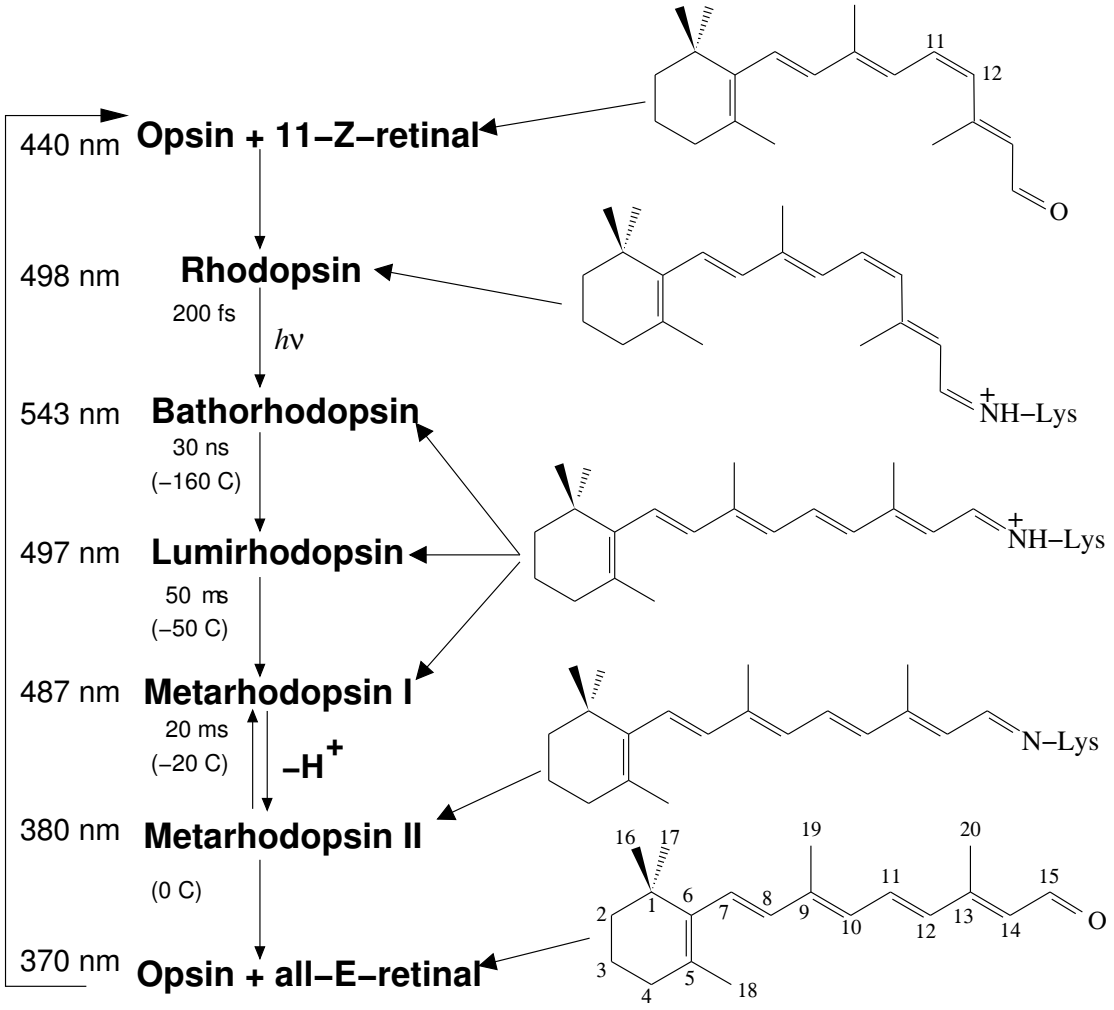

Figure 5.4: The photocycle for rhodopsin, from the moment of light absorption to the release of all-*E*-retinal, for several intermediates. At the end of the photocycle, the all-*E*-retinal is isomerized back to 11-*Z*-retinal by enzymatic action, to bind opsin and regenerate rhodopsin. The duration of each step at physiological temperature is given, together with the approximate temperatures below where each intermediate can be isolated, in parantheses. The maxima in the absorption spectra, $\lambda_{\max}$, for the retinal fragment are also indicated beside each intermediate.

place in the photoreceptor cell will not be given here. These are best investigated using other techniques than solid-state NMR. Instead, we will focus on the structure and conformational changes of the chromophore retinylidene and try to get an insight about the detailed structure of the conjugated chain.

5.3 Data about Rhodopsin

The precise geometrical changes in the chromophore that lead the GPCR to activate its G protein are not yet known in detail. What is known is that the activation is due to the absorption of a photon by rhodopsin, which is isomerized within 200 fs.[101] This first step is believed to be associated with the Z to E conformation change in the retinal fragment,[104–107] while the surrounding protein cavity stays approximately the same. The determination of the structure of rhodopsin and its photointermediates, together with the understanding of the energy storage mechanism, has been the motivation of many studies. Many researchers tried to justify the mechanism for energy storage in bathorhodopsin, but no clear mechanism for the energy storage is yet available. Possible hypotheses invoke energy storage through charge separation and geometrical strain.

The efficiency and speed of the first step of vision is deeply linked to the precise structure of the chromophore, as has been shown by incorporating modified retinals into rhodopsin . In all cases, the effect is to have a substrate which is less efficient than the natural one. The discussion which follows is related to one particular type of rhodopsin, i.e., bovine rhodopsin, on which we have performed some C-C distance measurements along the retinal chain. Before discussing our results, it is necessary to give at least a very short overview on what has been already done. The information come from several sources, i.e., diffraction, vibrational and optical studies, NMR spectroscopy and quantum-mechanical simulations.

5.3.1 Optical Studies and Identification of Photointermediates

Thanks to optical studies at variable temperature,[108] the main intermediate states of rhodopsin have been isolated and the temperature below which they can be trapped are listed in Fig. 5.4. Each intermediate of rhodopsin is clearly distinguishable in terms of a shift in absorbance band, $\lambda_{\max}$, in its UV-Vis spectrum.[101,108] The absorbance band in bovine rhodopsin has its maximum near 500 nm (in the yellow-green region) while only minimal absorption above 600 nm (red region) is observed. This implies that the samples can be safely handled under dim red light.

The frequencies of maximum absoption for several photointermediates are also reported in Fig. 5.4. This information is important not only because it specifies the regime under which different forms of rhodopsin, after illumination, can be selectively investigated, but also because it gives some insight over the energy content of the ground state and first excited state of each form. An estimate of the time-scales for the formation of the different photointermediates, as listed in Fig. 5.4, comes from optical measurements.

To be strict, bathorhodopsin is the first *stable* intermediate. Studies at physiological temperature using time-resolved resonance Raman spectroscopy indicate the existence of another species, called photorhodopsin, which is formed within 200 fs. It has not yet been possible to trap photorhodopsin by sample cooling. It is considered as a "hot" intermediate and relaxes to bathorhodopsin within 5 ps.

On this basis, there is some evidence that the C11=C12 double bond may already isomerize within 1 ps, maybe even in 200 fs.[106,107] Pioneering studies[108] showed that it is possible to convert lumirhodopsin back and forth to bathorhodopsin and rhodopsin at temperatures as low as liquid nitrogen temperature (-195°C), which suggests that opsin is only slightly affected in conformation during the two initial steps. The light-driven interconversion between metarhodopsin and the previous photointermediates is possible at -20°C but *not* -65°C, which suggests that the bulk protein structure undergoes major rearrangements when metarhodopsin is formed, i.e., the reconversion requires more thermal energy than is available at -65° C.

The next photointermetiate, metarhodopsin, exists in two forms: metarhodopsin I (M I) is the protonated form while M II is deprotonated, after hydrolysis. The proton migration is a key step in the activation of the G protein since only M II interacts with alpha transducin and starts the chain of reactions within the cell.

5.3.2 Diffraction Data

Rhodopsin has been the subject of much research for many years, not only to obtain the overall protein structure but also the retinylidene PSB structure. The knowledge of the precise structure of the chromophore has motivated the synthesis and XRD structure determination of many compounds in this family, with structural motifs similar to the rhodopsin chromophore. The available XRD structures include all-*E*-retinal,[109] 11-*Z*-retinal,[110] three all-*E*-retinal PSBs: N-methyl-N-phenylretinal iminium perchlorate[111] (labelled PSB_I in what follows), N-*tert*-butyl-retinal with perchlorate (PSB_{II}) and triflate (PSB_{III}) as counterions[112]). A comparison of bond-lengths between these compounds shows a strong bond-length alternation throughout the chain for the aldehydes and an alternation reduction close to the end of the tail in the PSB, due to the presence of the positive charge. The extent of bond-length alternation in the PSBs changes is significantly different, with bond-lengths differing up to 3 pm on some sites. The terminal imino groups strongly influence the local chain structure. The aliphatic PSBs are expected to be electronically closer to the state in the protein, but even there a variation of the counterion induces significant bond length variations on some positions. The large environment difference between the model PSBs and the 11-*Z*-retinal in the protein makes any extrapolation rather uncertain, even though a bond-alternation reduction is expected also there.

A crystal structure of bovine rhodopsin is now available[113,114] and the chromophore appears to have the configuration 6s-*cis*, 11-*cis*, 12s-*trans*, anti C=N. The latest structural refinement has a resolution of 2.6 Å.[100] This allows the identification of the protein fragments determining the size and shape of the binding pocket as well as functionally important water molecules within rhodopsin, also

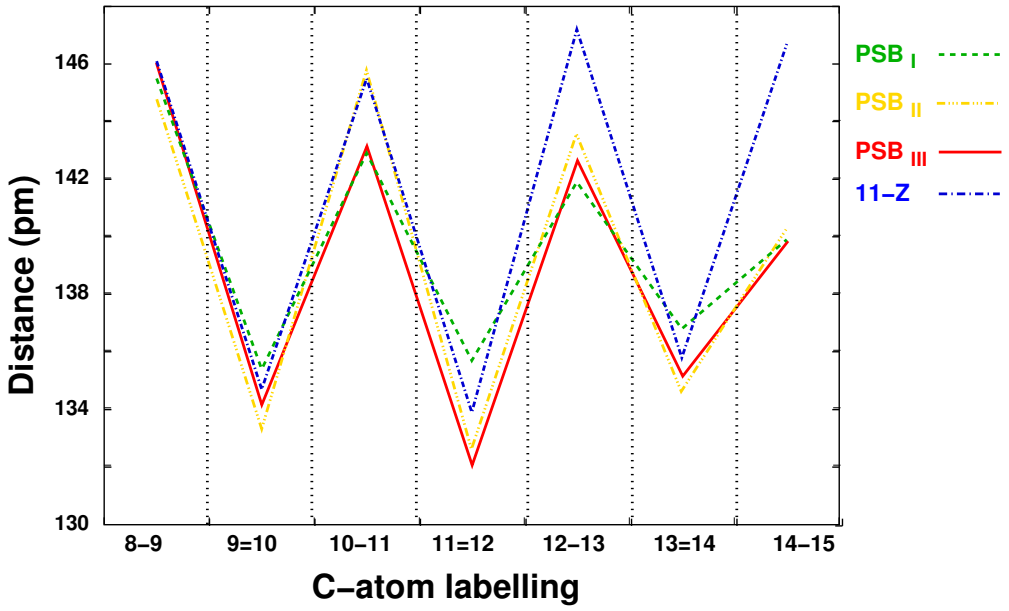

Figure 5.5: CC bond lengths from XRD data for three all-*E*-retinal PSB: N-methyl-N-phenylretinal iminium perchlorate[111] (PSB_I), N-*tert*-butyl-retinal perchlorate[112] (PSB_{II}), triflate[112] (PSB_{III}) and 11-*Z*-retinal.[110] Notice the wide structural changes between different PSBs, due to a modification of the imino group or even by a simple change in the counterion.

in the proximity of the chromophore. These structural data are of great importance for a deeper understanding of the chromophore structure, since they reveal which groups are in a range to affect the retinylidene, either directly or through a hydrogen-bonding network, and thereby allow for a better description of the electrostatic and steric interaction between the chromophore and the surroundings. A view of the binding pocket is given in Fig. 5.6, where the chromophore (black), the closest amino acid residues and some water molecules (all explicitly labelled) are drawn using the coordinates from the protein data-base (PDB) file[100] and the programs Rasmol and Xfig. One water molecule interacts closely with Glu-181 and Ser-186 and is expected to have some role in color regulation. The water closer to Glu-113 is not located between the carboxylate and the retinal PSB, but close to the Glu-113 chain. This indicates a more subtle influence on the Glu-113 pK_a value through side-chain interactions rather than the existence of a complex counterion, as postulated on the basis of NMR data. On the other hand, water can exchange fast and this may affect the XRD data.

In the case of rhodopsin, it is necessary to analyse carefully the constraints coming from XRD since its limited resolution (so far) is not always sufficient to completely prove or disprove some experimental evidences or models obtained with other techniques.

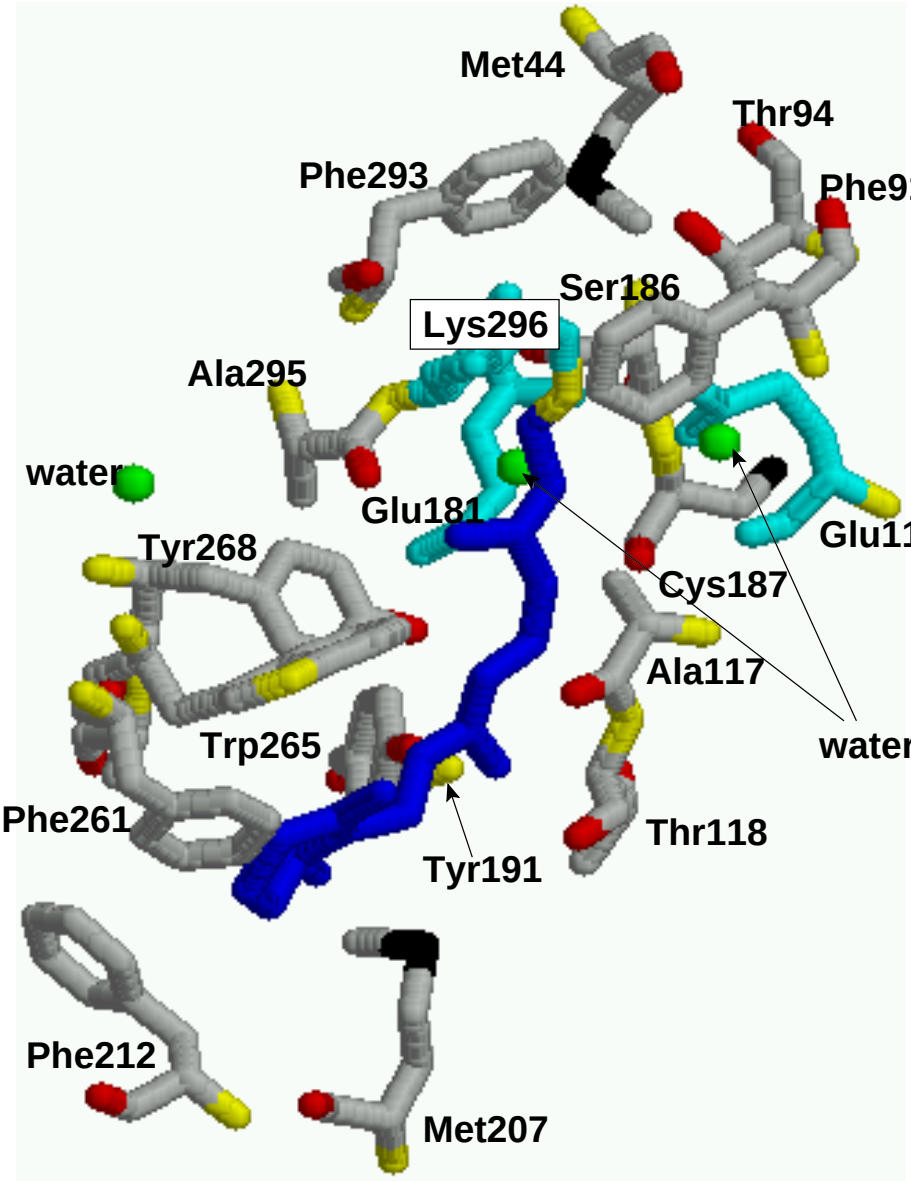

Figure 5.6: Retinal binding pocket,[100] with 11-*Z*-retinal (black) and the closest amino acids determining the main steric and electrostatic interactions with the protein

5.3.3 Vibrational Data

Vibrational studies of compounds belonging to the retinal family (vitamin A and retinal derivatives) by FT-IR and resonance Raman spectroscopy provide insight into the bond distribution and the general conformation of the observed molecule. The information on bond distances and angles is not quantitative, due to the complexity of the system and to the strength of the coupling between vibrational modes of similar frequency. On the other hand, the presence of methyl groups along the conjugated chain breaks up some normal modes into subsets which can be clearly associated with different portions of the chain.

One important feature of resonance Raman spectroscopy is that the frequency of the normal modes gives insight into the ground-state structure, while the intensities give information on the excited state. The intensities of the modes that get mostly shifted upon electronic excitation are highly enhanced and reflect the dynamics of the excited state. Many vibrational modes (especially the modes at high frequency) are well understood and assigned by comparing similar compounds and specifically labelled retinals (isotope enrichment shifts some modes with the help of small mass differences). In addition, it is also possible to perform theoretical *ab initio* calculation to match the observed pattern to the suggested theoretical model. A theoretical model properly describing the experimental data[115] is now available. Many lower frequency modes are not fully accounted for, even though the general trend is well-reproduced and the mode shifts due to structural modifications can be predicted to a good extent. For instance, torsional modes for the skeletal region and C11=C12 have been identified near 570 cm^{-1} and 260 cm^{-1} and are considered important coordinates in the photoreaction.

Resonance Raman spectroscopy gives a clear indication of the following facts:

- the fingerprint regions of 11-*Z*-PSB in solution and rhodopsin are quite similar, confirming a general similarity in conformation and bond orders.[116] The differences may be related to the protein environment and to the photoreaction pathway.

- there is a significant hydrogen out-of-plane (HOOP) distortion about the C11=C12 bond,[117] believed to be an important normal coordinate in the fast isomerization[115]

- there is a significant chain distortion out of the molecular plane in the C10...C13 region due to the steric interaction between C10 and the methyl group C20. This is of key importance for the efficient conversion to the first photointermediate[118]

- bathorhodopsin seems to have a highly twisted all-*E* structure (indicated by the large difference in HOOP and in C-C stretch frequencies with respect to all-*E*-retinal PSB).

- precise time measurements for the first steps in the photocycle show only minor differences in the vibrational spectra of photo- and bathorhodopsin, indicating high similarity of their interactions with the protein pocket and of their structures[106]

- indication of the skeletal and torsional normal motions involved in the photoreaction

5.3.4 Previous NMR Data

Many NMR experiments have been aimed at localizing the chromophore and orienting it within the protein pocket with respect to some relevant amino acids in the pocket. Some of the structural hypotheses based on NMR data have been confirmed by the high-quality XRD structure. Here we recall some of the previous NMR data, with particular attention towards the constraints on the chromophore structure:

- study of isotropic chemical shifts and CSA tensors in positions C5 and C14 provide evidence of an 6-s-*cis* conformation in rhodopsin and of a C=N anti configuration,[119]

- low-temperature determination of isotropic chemical shifts for selectively ^{13}C-labelled rhodopsin, bathorhodopsin and isorhodopsin[120,121] support a machanism of energy storage that does not involve significant charge separation.[122] Chemical shift differences between some labelled sites in rhodopsin and model compounds suggest electrostatic interactions within the protein pocket in the vicinity of C13,

- confirmation of the retinal PSB counterion as the residue Glu-113, about 3 Å away from C12 from ^{13}C chemical shift calculations,[123]

- HCCH torsion angle measurement around the C10-C11 bond,[96,97] $\psi = 160^{\circ} \pm 10^{\circ}$ in rhodopsin and $\psi = 180^{\circ}$ in M I,

- rotational resonance distance determinations between C20 and respectively C10 ($r_{ij} = 304 \pm 15$pm) and C11 ($r_{ij} = 293 \pm 15$pm). These data have been used to determine the torsion angle between the C6-C10 and C13-C15 conjugation planes to 44°. Corresponding measurements in M I indicate $r_{10,20} > 430$ pm, which is compatible with an all-E configuration of the chromophore.[40]

- Evidence of a complex counterion, possibly made up of Glu-113 and a structural water molecule based on the ^{15}N-lysine isotropic chemical shift and 430 pm from ^{15}N,[124,125]

- ^{2}H-NMR of aligned samples (Sect. 4.4), deuterated at specific methyl groups, provide the orientation of the C-CH_3 bond with respect to the membrane long axis.[95,126] The data indicate a 6s-*trans* conformation as more favourable.

- Studies on fully ^{13}C labelled retinylidene chain[127,128] and determination of isotropic ^{13}C (compatible with Ref. 120) and ^{1}H chemical shifts: insight on electronic distribution and intermolecular interactions through chemical shift comparisons with model retinals and calculations (complex counterion, unique 6s-*cis* configuration of β-ionone ring and interaction between the β-ionone ring and aromatic amino acid side chains).

While geometrical constraints can be of direct use for calculation and structural refinements, the isotropic chemical information have a less direct interpretation and can be compared to theoretical calculations. A simple comparison between the isotropic chemical shift of the PSB within the receptor and other retinal-like chains gives insight about the charge delocalization and the bond alternation for the different retinal-like compounds. On the other hand, these observations are often inconclusive due to the complexity of the system and do not directly lead to quantitative information about charge distribution, distances and conformations.[129]

This thesis adds a few more pieces of information to the knowledge of rhodopsin by adding some experimental data on bond lengths along the retinylidene chain by solid-state NMR.

5.3.5 Quantum Mechanical Calculations

The dark state of rhodopsin is expected to have delocalized electric charge within the conjugated chain. In this context, many theoretical models stress that this is the key role of the positive charge on the PSB and the presence of a neighbouring glutamate counterion. One of the main goal of theoretical calculation is to obtain the structure of the chromophore. This includes estimates of geometry (bond lengths, bond angles and so on). From these, models are provided which may justify the observed spectroscopic properties and the chemical shift distribution.

The ground state of rhodopsin was investigated by Buda *et al.* in 1996,[130] using density functional thery (DFT) and the Car-Parrinello *ab initio* approach. The counterion of the retinal PSB was modelled as a chlorine ion, 4 Å away from C12, approximately in the same region where Glu-113 was expected to be but much simpler to simulate. This model of rhodopsin came before the three-dimensional structure became available from diffraction studies. The calculation used distance constraints from solid-state NMR. Nevertheless, as can be seen from the bond-distance calculation on a model 11-*Z*-retinal compound (for which an accurate XRD is available[110]) the DFT calculations tend to overestimate the conjugation effect (underestimate the bond length alternation) and the computed bond-lengths do not faithfully reproduce the XRD data, as shown in Fig. 5.7. This issue is addressed in Ref. 129, where a comparison between distances in two different retinal PSBs from XRD and the corresponding DFT structures confirms this systematic calculation error, but also points out that the presence of a positive charge in the chain can be qualitatively accounted for. On the other hand, the increased conjugation towards the end of the chain is correctly predicted.

More recently, Sugihara *et al.* investigated the structure of the retinal PSB in rhodopsin using a molecular dynamics DFT calculation, starting from 11-*Z*-retinal PSB on which some strain mimicking the protein cavity is applied. He used a carboxylate anion and a water molecule to describe a more complex counterion[131,132] (instead of the chloride ion), which may have an important effect for stabilizing the positive charge, leading to a less pronounced delocalization along the chain and to a strong double-bond component for the C11=C12 bond. The resulting structure exibits a stronger bond-length alternation than in Ref. 130. This is confirmed

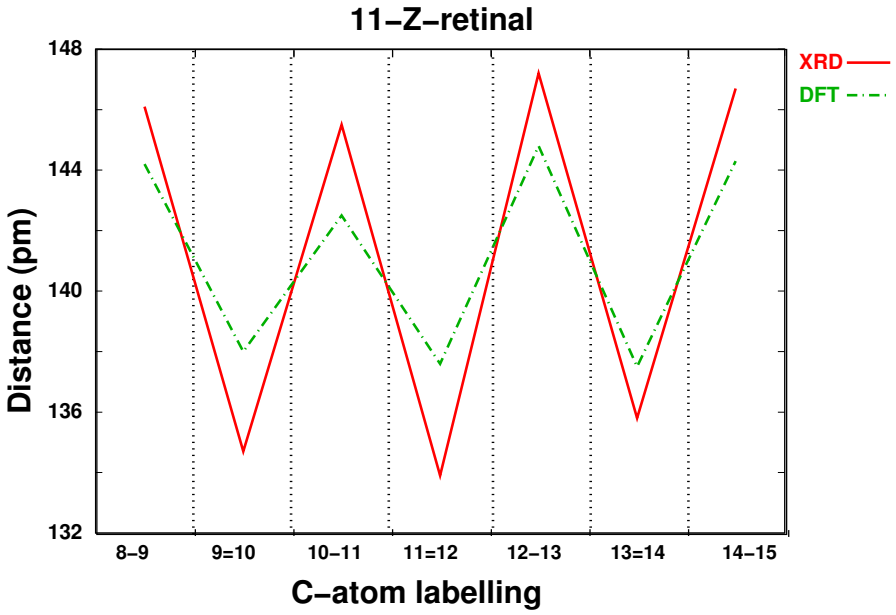

Figure 5.7: Comparison between experimental[110] and calculated[130] bond-lengths for 11-*Z*-retinal. The bond alternation is systematically underestimated by the DFT calculation with local density approximation (LDA)

in a more recent work,[133] where the known three-dimensional crystal structure of rhodopsin with 2.8 Å resolution is explicitly included in the calculation to refine the structure of the chromophore. The adopted calculation method in this case is the self-consistent charge (SCC) DFT. 27 amino acid fragments in a range of 4.5 Å from the retinylidene were included, using the coordinates from the PDB structure taken from Ref. 113.

As mentioned before, another target of theoretical calculation is the isotropic chemical shift distribution, which depends upon the electronic strucure *and* interactions between the chromophore and the residues within the protein pocket. This makes the data interpretation rather difficult. Theoretical ^{13}C isotropic chemical shift and CSA calculations have been used to predict conformation of specific fragments and charge delocalization,[129] but the authors themselves suggest caution in the data interpretation. For instance, it is found that the correlation between isotropic ^{13}C chemical shifts and partial charges along the chain is sample dependent.[129]

5.4 Distance Measurements on Rhodopsin by DQ Solid State NMR

A set of distance measurements on the conjugated chain of the retinylidene chromophore of bovine rhodopsin has been recently performed in our group. Although crystal structures of rhodopsin have been published, the resolution of 2.6Å is not sufficient to answer questions relative to the bond order within the chromophore chain. Our goal is to investigate the structure of the chain and obtain experimental

data on the amount of delocalization of the electron charge.

5.4.1 Sample Preparation and Technical Details

The labelled retinals were prepared by full organic synthesis according to the procedure described in Ref. 134. The labelled retinals were partly prepared in our laboratory and partly provided by Lugtenburg et al. The labelled all-*E*-retinals were converted to the desired isomer, in this case 11-*Z*-retinal by dissolving the compound in a solution of dry acetonitrile under controlled illumination conditions. The desired isomer was isolated from the mixture by using high-performance liquid chromatography (HPLC) using normal phase, i.e., polar column and apolar eluent.

Bovine opsin was isolated from cow eyes and the 11-*Z*-retinal inserted in its natural membrane protein. This part of the sample preparation was entirely performed in de Grip's group (Petra Bovee-Geurtz) and the details of the methodology can be found in Ref. 135. The protein/membrane ratio was typically ca. 50% (by mass).

The insertion of the chromophore in the protein opsin was verified by optical measurements, due to the difference in optical absorbance between rhodopsin and 11-*Z*-retinal (respectively 498 nm and 440 nm). The regenerated protein, centrifuged and frozen into small pellets, was transferred into a standard 4 mm zirconia rotor by centrifugation, increasing gradually the rotation frequency from 500 rpm to 16000 rpm at a temperature of $+2^{o}$ C, for a total time of ca. 40 minutes. To perform this operation, the zirconia rotor and the sample were placed inside a purpose built teflon holder.

The amount of labelled protein used in each 4 mm rotor was estimated to be between 15 mg and 20 mg, i.e., about 0.45 μmol of labelled rhodopsin per sample. The overall mass of sample transferred into the rotor was much larger, since each protein sits in its natural plasma membrane (about 60 mg).

It is important to stress that the handling of rhodopsin samples must be performed in the dark or in rooms equipped with dim red light at all times. The protein samples and the retinals are best stored in light-tight containers within the -80^{o} C freezer and in a nitrogen atmosphere. This is to minimise light-induced isomerization of the retinal chain, water absorption and side reactions with oxygen. One model all-*E*-retinal compound was used for the temperature calibration set-up. A small amount of lead nitrate was packed in the bottom and in the top of the 4 mm rotor, separated from the retinal by a thin layer of teflon tape. The sample was spun at 5.5 kHz at room temperature and the temperature of the air was established via a digital thermometer. This moderate spinning frequency regime was previously observed to induce a temperature discrepancy of less than one degree in the sample. Subsequent cooling of the spinning sample leads to a shift of the ^{207}Pb resonance which is dependent on the temperature shift[136] according to the equation

$$\Delta\delta^{\mathrm{iso}} = 0.753 \times \Delta T \quad \mathrm{ppm/K} \tag{5.1}$$

There are several models[137–139] for relating the shift in ^{207}Pb resonance to a temperature variation but they are in good agreement, within a few degrees.

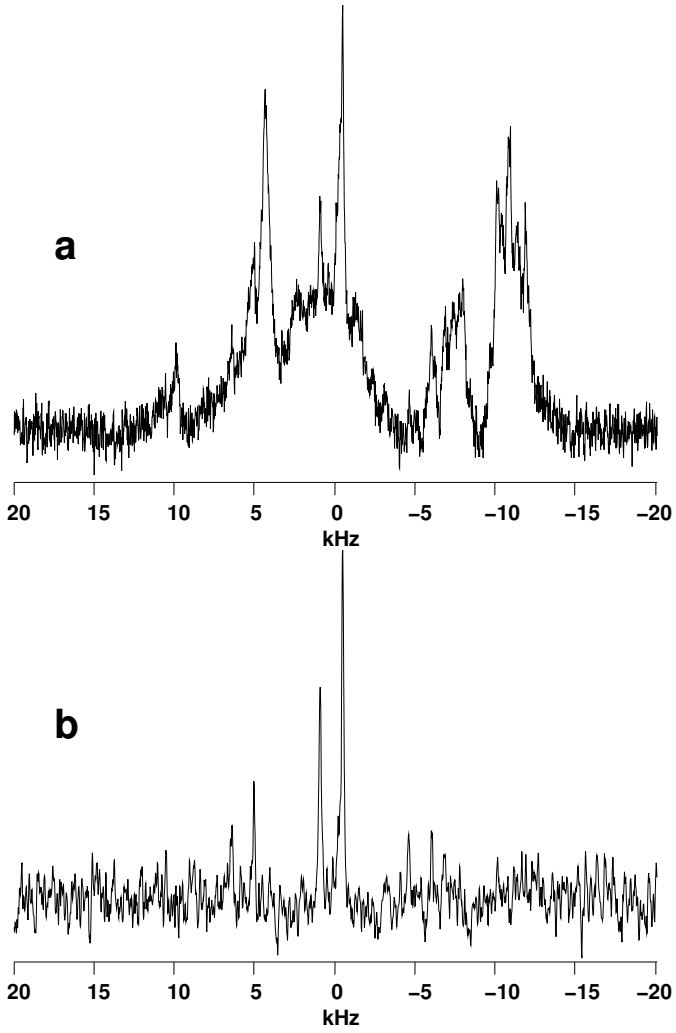

Figure 5.8: (a) 1408 scans CP spectrum of 10,11-$^{13}C_2$-labelled rhodopsin performed at -100°C and $\omega_r/2\pi = 5.5$ kHz (b) 5120 scans DQF spectrum acquired in the same conditions and using τ_{exc}=τ_{rec}=468 μs.

In this thesis, all temperatures refer to the true sample temperature, as calibrated by the ^{207}Pb resonance of $PbNO_3$, not to the spectrometer readings from the thermocouple, which were typically lower. The discrepancy between readings and real temperature increases at low temperature, due to frictional heating in the rotor bearings and to the use of room temperature nitrogen gas for bearings and drive.

5.4.2 NMR Measurements on Rhodopsins

For all dipolar recoupling experiment, the $R14_2^6$ sequence with R^0=90_0 270_π, already demonstrated for distance measurements in Paper II, was used for exciting DQ coherences at a spinning frequency of $\omega_r/2\pi$=5.5 kHz. The temperature was calibrated to 173 K for all experiments.

The pulse sequence parameters were first optimized on all-*E*-retinal samples as

model compounds, doubly-labelled in the same position as the protein. A reference build-up curve on the labelled retinal was acquired as part of the calibration procedure and followed by the distance measurement experiment on the protein. The resulting NMR measured distance for the retinals are compatible with the XRD data.[109] For each protein sample, the ramped CP spectrum and a build-up curve of 8 points were acquired, the points being chosen in a way to show at least a full dipolar oscillation. Fig. 5.8 compares the CP spectrum for 10,11-$^{13}C_2$-rhodopsin with the corresponding DQF spectrum, corresponding to the maximum DQF efficiency. The DQ filtered spectrum shows very clearly the signal coming from the labelled retinylidenes and the isotropic chemical shifts fully agree with values obtained in previous studies.[127] The build-up curve for this same sample is shown in Fig. 5.9, together with a possible fit of the data set. The bovine rhodopsin samples examined so far are labelled in positions (10,11), (11,12), (12,13), (13,14) and (14,15).

5.4.3 Vibrational Corrections

As discussed in Sect. 4.3, the internuclear distance estimated from solid state NMR suffer a systematic overestimate error, partly due to molecular vibration. We estimated the average discrepancy and the standard deviation in our ^{13}C-^{13}C bond-length measurements to be 3.0 ± 1.3 pm and in the data analysis of the measurements on rhodopsin we apply a correction of 3.0 pm to the NMR estimated distance,

$$r_{jk} = r_{jk}^{NMR} - 3.0 \text{ pm} \tag{5.2}$$

since the error on the NMR data analysis is statistically independent from the error on due to molecular vibrations, it is possible to recalculate the total error for the internuclear distances as

$$\Delta r_{jk} = \sqrt{(\Delta r_{jk}^{NMR})^2 + (\Delta r_{jk}^{Vib})^2} \tag{5.3}$$

where $\Delta r_{jk}^{Vib} = 1.3$ pm.

5.4.4 Data Analysis

The bond distances measured in the rhodopsins are summarised in Table 5.1, together with additional information.

For the error analysis, the signal is calculated by integrating the peaks in the same region in each spectrum (and is always clearly visible in most elements of the array), while the noise is estimated by integration over a comparable spectral range in signal-free regions to determine the uncertainty on each point in the build-up curve. For the analysis, a distribution of build-up curve functions is created around the integrated values, which is our signal, with an error bar given by the noise itself. Statistically, the noise is expected to be the same for all elements of the build-up curve, all corresponding to the same number of scans. The analysis program iterates to obtain the internuclear distance according to the procedure

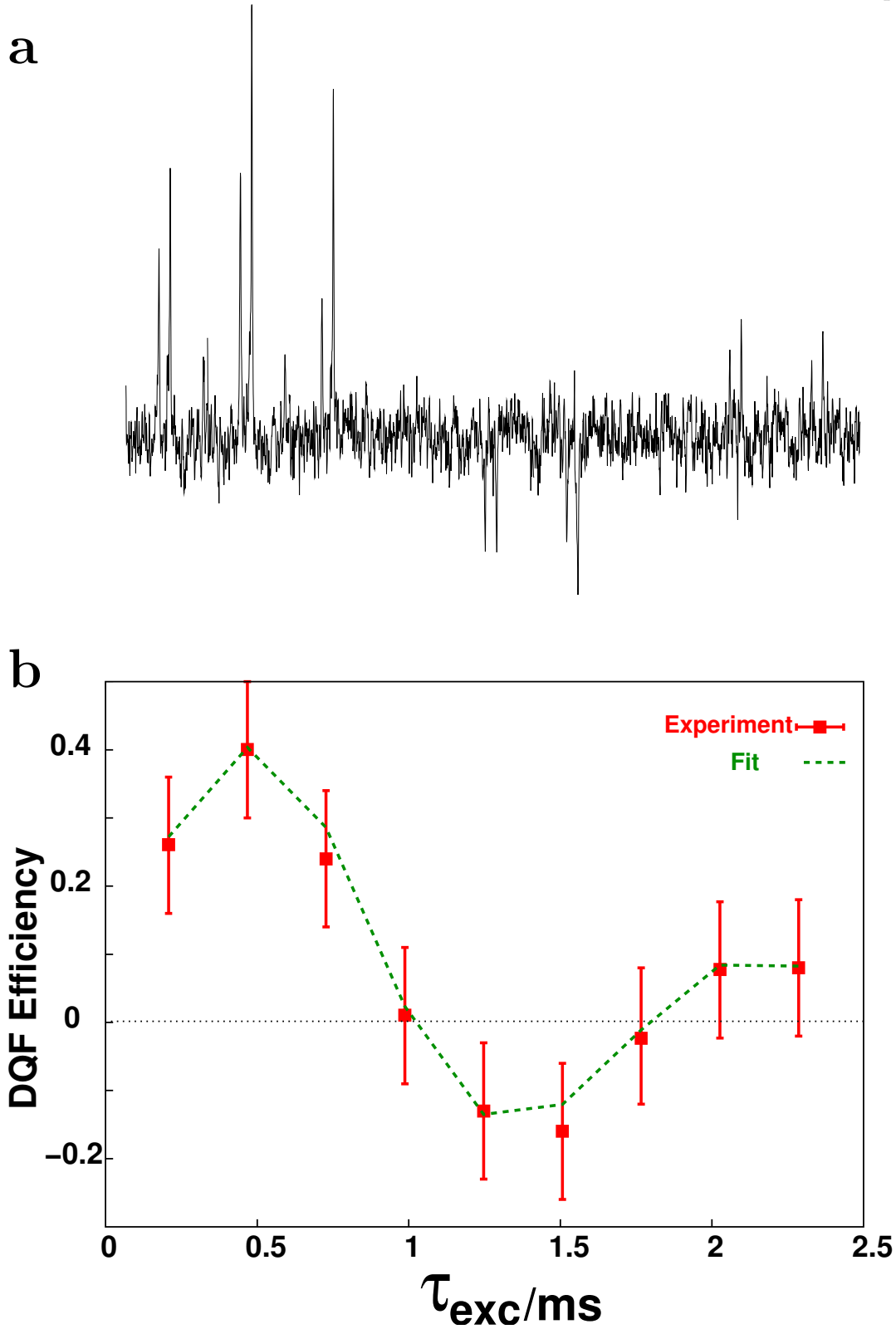

Figure 5.9: (a) experimental spectra from the distance measurement experiment on 10,11-$^{13}C_2$-labelled rhodopsin performed at -100°C. Each experiment correponds to 5120 transients. The reconversion time is fixed to τ_{rec}=468 μs while τ_{exc} is incremented from 208 μs to 2.29 ms in steps of 260 μs (b) integrated intensities with an error bar corresponding to the estimated noise uncertainty, together with the best simulation fit

Table 5.1: Some bond lengths within the retinylidene chain for different retinal-like compounds, as obtained from crystallography, quantum-mechanical simulations and solid-state NMR measurements on all-*E*-retinal and rhodopsin, using several models for the CSA for the latter (with vibrational correction).

	XRD data						DFT Calculations		Solid-State NMR			
	all-*E*	11-*Z*	PSB_I	PSB_{II}	PSB_{III}	rhodopsin	RPSB		retinal	rhodopsin		
Reference	109	110	111	111	111	100	130	133	*a*	*a*	*b*	*c*
C8—C9	146.7	146.1	145.5	144.7	146.0	148	144.2	144.3				
C9=C10	134.5	134.7	135.4	133.3	134.1	134	138.8	138.6				
C10—C11	144.2	145.5	142.9	145.7	143.0	148	142.2	142.6	$143.9^{1.6}_{1.6}$	$143.7^{2.9}_{2.7}$	$143.5^{2.5}_{2.4}$	
C11=C12	133.8	133.9	135.7	132.6	132.0	136	138.9	137.8	$134.4^{2.1}_{2.0}$	$135.8^{2.5}_{2.4}$		$136.0^{2.6}_{2.6}$
C12—C13	145.2	147.2	141.9	143.5	142.6	148	142.3	143.5				$141.5^{2.9}_{2.8}$
C13=C14	134.4	135.8	136.8	134.6	135.1	135	140.6	139.2	$136.2^{2.2}_{2.2}$			$137.0^{2.4}_{2.3}$
C14—C15	145.5	146.7	139.9	140.2	139.8	150	139.1	142.0	$146.1^{2.3}_{2.2}$	$144.2^{3.0}_{3.0}$	$142.5^{2.6}_{2.5}$	$142.8^{2.6}_{2.4}$

[a] Solid-state NMR using the known CSA parameters for all-*E*-retinal

[b] Solid-state NMR using CSA parameters estimated from the spectrum

[c] Solid-state NMR using CSA parameters estimated from 2D PASS at 16.7 T

Table 5.2: Chemical shift anisotropy (in ppm units) used in simulation as reported in Ref. 77 for all-*E*-retinal; the rhodopsin CSA values at 9.4 T are estimated from the spinning sideband pattern in the DQF spectrum with no explicit correction for the effect of dipolar couplings; the parameters at 17.6 T are determined from 2D PASS on the fully ^{13}C-labelled chromophore (private communication from Suzanne Kiihne).

^{13}C-position	all-*E*-retinal	rhodopsin (9.4 T)	rhodopsin (17.6 T)
δ_{10}^{aniso}	80.8	78.7 ± 11.8	
η_{10}	0.98	1.0 ± 0.25	
δ_{11}^{aniso}	-101.5	-107.5 ± 16.1	-105 ± 9.5
η_{11}	0.77	0.5 ± 0.25	0.82 ± 0.16
δ_{12}^{aniso}	81.7	106.1 ± 15.9	
η_{12}	0.93	0.65 ± 0.25	
δ_{13}^{aniso}	-125.0		131 ± 10.5
η_{13}	0.50		0.44 ± 0.18
δ_{14}^{aniso}	-70.0	88.3 ± 13.2	-80 ± 2.9
η_{14}	0.99	1.0 ± 0.25	0.63 ± 0.19
δ_{15}^{aniso}	-92.5	-118.5 ± 17.8	-112 ± 9.5
η_{15}	0.51	1.0 ± 0.25	0.33 ± 0.27

described in detail in Paper II. The error margins in the determination come from a set of distance optimizations for a distribution over the Euler angles defining the orientation of the CSA tensors (fully randomized) *and* over the rf field, with a standard deviation of 3%. This approach is used to analyse the data acquired on our standard all-*E*-retinal compounds and is expected to be a reliable upper bound to the error.

For the analysis of rhodopsin, we introduce two additional distributions, i.e., a rather large distribution over the CSA principal values, with a standard deviation of 15%, and a distribution over the asymmetry parameter, with standard deviation 0.25. These distributions are very broad, given that the two CSA sets used in the data analysis as origin of the Gaussian distribution are likely to be not too accurate: (i) all-*E*-retinal may well have different CSA values than the corresponding 11-*Z*-PSB; (ii) the CSA estimated from the DQF spectra from doubly-labelled proteins by analysing the sideband pattern, using the procedure described in Ref.,[140] suffer from the presence of a strong dipolar interaction, which is not included in the analysis but is known to affect the spinning sideband intensities, thereby introducing an error. (iii) CSA estimated by 2D PASS[140] on rhodopsin with U-^{13}Clabelled retinylidene at 17.6 T and 6.0 kHz. These last data are expected to be more accurate since the relative error due to the presence of homonuclear couplings decreases with increasing field. The corresponding datasets for all-*E*-retinal, rhodopsin at 9.4 T and 16.7 T are listed in Table 5.2

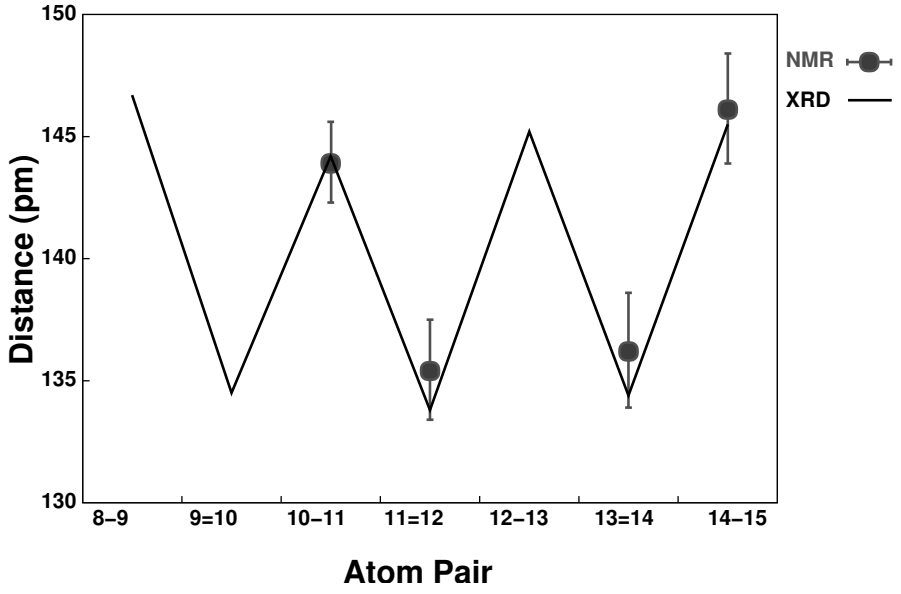

Figure 5.10: Distance measurements on all-*E*-retinals used as model compounds for the protein meausrements. The NMR results agree very well with the XRD data[109] after vibrational correction.

5.4.5 NMR-Based Model

A summary of the distances determined by solid-state NMR is in Table 5.1. Fig. 5.10 shows a good agreement between the NMR data and the XRD data on all of the model compounds used to set up the measurements in the protein. The results for the distance estimate are plotted in Fig. 5.11 and 5.12, compared with the distances for other retinal-like samples coming from XRD and theoretical calculations (described in Sect. 5.3.5). As can be seen, our measurements indicate that the retinylidene chromophore maintains clear single bond-double bond alternation. The bond lengths show the conjugation effect to a similar extent as in 11-*E*-retinal but with a slightly higher delocalization towards the very end of the chain. Due to the great geometrical variations among PSBs as a function of the counterion and of the imino group, the comparison between these and rhodopsin can only suggest some similarities but with a remarkable bond length difference for C14–C15. To date, there is no XRD structure of unprotonated SB due to the difficulty of crystallizing it, but it would be certainly interesting to obtain its structure. The conjugation level within rhodopsin is much less than predicted by the theoretical models (see Sect. 5.3), but it is compatible with the recent model in Ref. 133.

A comparison between the bond distances determined so far is sufficiently precise to allow for discrimination between different theoretical models and allow for a reasonable comparison between the bond length distribution in rhodopsin and in other retinals. This results are preliminary, as the data refinement is in progress. The reduction of the error bars on the largest CSAs would allow to reduce the error bars in our measurements to some extent.

The presence of bonds with a clear single bond order can give some insight on the structure of the ground state molecule which undergoes a conformation

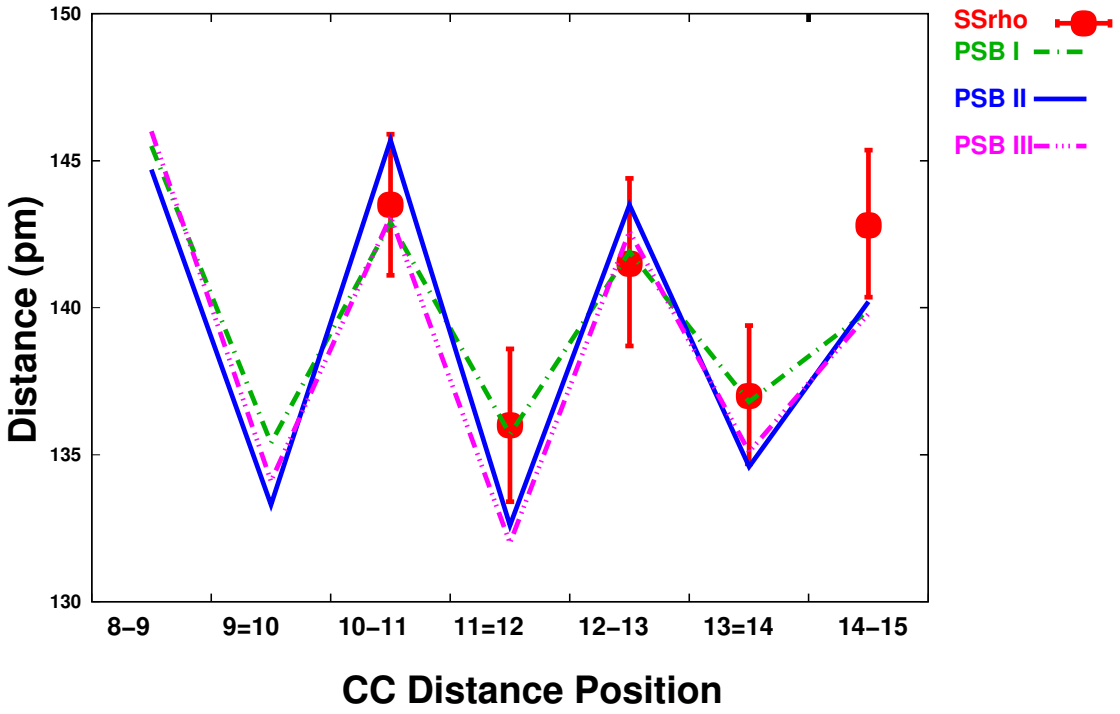

Figure 5.11: Selected C-C bond lengths in rhodopsin, as obtained from solid-state NMR and from diffraction studies on three model compounds, the all-*E*-PSB model compounds from Refs. 111 and 112

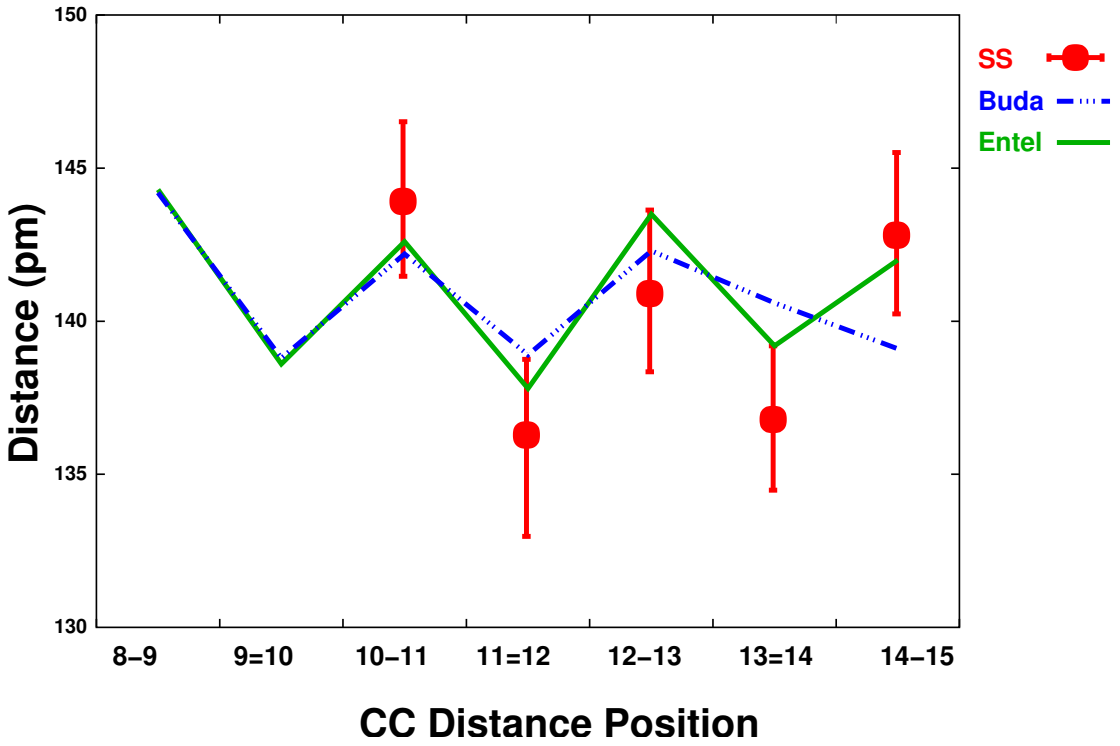

Figure 5.12: Selected C-C bond lengths in rhodopsin from solid-state NMR plotted against two theoretical models, from Refs. 130 and 133 and the retinilydene data from XRD at 2.6 Å resolution[100]

change within 200 fs. Any model to describe the isomerization of rhodopsin needs to justify some important experimental facts, i.e., how the energy is stored, why is the conversion so fast and efficient as well as data coming from other studies. The work is still in progress, but the presence of bonds with a strong alternation may suggest that torsions around the single bonds is facilitated, leading to a chain which is highly twisted and trans about the C11=C12. This would not necessarily correspond to structure as highly strained as the one modelled assuming strong electron delocalization all over the chain, due to the flexibility of single bonds. We anticipate the importance of these experimental results for future theoretical attempts to predict the transformation of a well-characterized rhodopsin into bathorhodopsin. A deeper understanding of the chromophore structure may also give more insight in the observed isotropic chemical shift distribution and in the CSAs.

Chapter 6

Triple-Quantum ^{13}C Coherence

6.1 Introduction

In the previous chapters we discussed some examples of the importance of multiple quantum filtration for extracting specific information on the system, in particular by using double-quantum coherences. A natural extension to higher order coherence orders is obvious, not only for the good suppression of signals coming from the so-called natural abundance background but also for providing an alternative route to a more precise definition of molecular properties. On the other hand, the amount of signal passing through a MQ filter decreases with increasing MQ order. This limitation affects both spin 1/2 systems and quadrupolar nuclei, but many methods for increasing efficiency and resolution for half-integer quadrupolar nuclei have been developed in the last few years and the field is in continuous development. Many demonstrations of MQC in abundant, high-γ spins, like protons[141–144] and on static solids[145,146] or liquid crystals[147–149] are available too. Not so much has been done on low-γ nuclei under MAS, the main contribution being due to Edén et al.[68,150] and Oyler et al.[151] The TQ-filtering efficiency achieved so far is approximately 4% in the first case and not quoted in the second, maybe too low to be conveniently extended to biomolecules. It is therefore important to make the high-order MQ more efficient to increase the applicability of the MQ excitation to real systems. Here we describe a new technique to excite triple-quantum coherences (TQC) under MAS with improved efficiency. The proposed method is very selective to certain spin systems: it is not meant to excite all possible TQC in a fully labelled sample, but rather to select TQC from a subset of spins with a specific relative arrangement. While this can sometimes be a drawback, it can be advantageous in other cases because it allows to look in detail at a specific portions of a fully labelled molecule, for instance. The experiment is performed on fully-^{13}C-labelled model compounds and it is not likely to be applicable to natural abundance ^{13}C compounds due to the low natural abundance of ^{13}C nuclei and to the steep decrease in efficiency for excitation of high MQ orders.

6.2 Pulse Sequence for TQ Excitation

In Paper IV, we present a new pulse sequence for TQ coherence excitation, demonstrated on a fully ^{13}C labelled model three-spin system, [U-^{13}C]-*L*-alanine. The

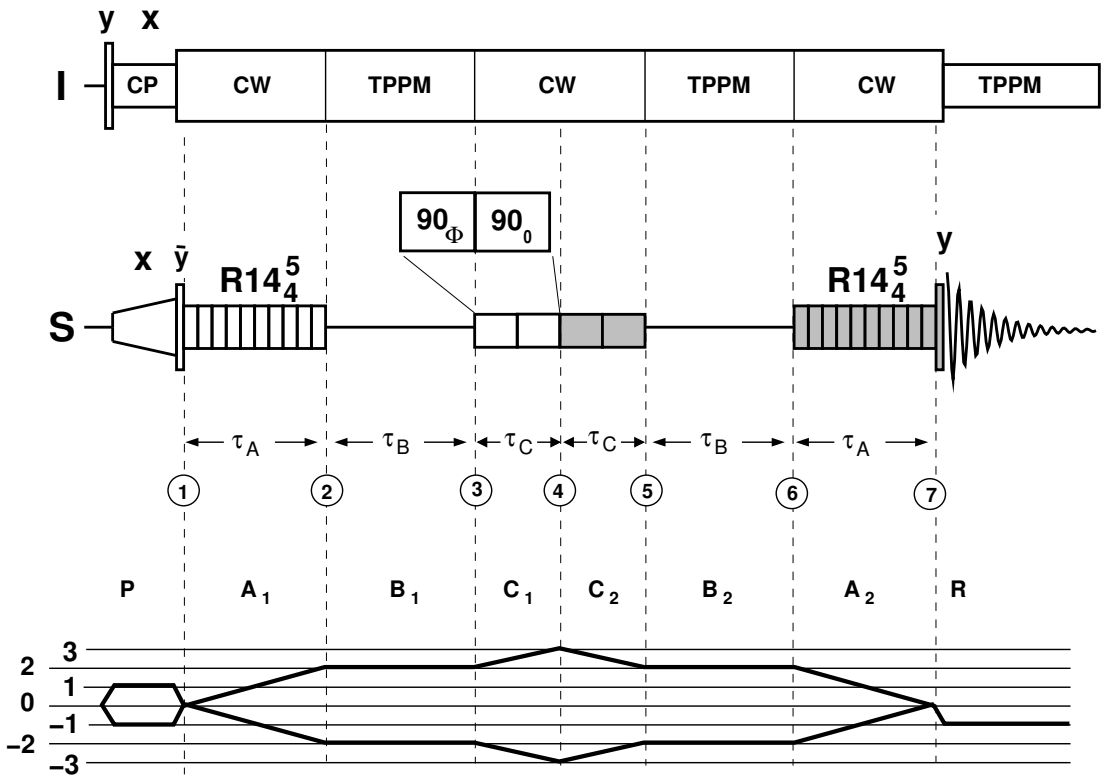

Figure 6.1: Pulse sequence for exciting TQ coherences: enhanced ^{13}C longitudinal magnetization (point ①) is transferred into selective DQ coherence for two of the three spins (point ②), followed by a period of free evolution under rotational resonance during which the two-spin coherence in transformed into three spin coherence, in ③; the selective pulse generates TQC in ④ and then the sequence is reverted in a symmetric fashion, leading to observable signal.

pulse sequence for TQ coherence excitation is shown in Fig. 6.1. This can be divided into a series of block whose action can be explained separately. To each block we associate explicitly a reference offset frequency, $\omega^{\rm ref}_{\rm block}$ and a phase $\phi_{\rm block}$. The pulse sequence works as follows:

- Step **P**: preparation of enhanced longitudinal magnetization with $\omega^{\rm ref}_P = (\omega^{\rm iso}_1 + \omega^{\rm iso}_3)/2$, i.e., approximately in the center of the spectrum.

- Step $\mathbf{A}_1$: selective excitation of DQC between spin 1 and 2, with $\omega^{\rm ref}_A = (\omega^{\rm iso}_2 + \omega^{\rm iso}_3)/2$.

- Step $\mathbf{B}_1$: Rotational Resonance (RR) evolution with a spinning frequency matching the $n = 1$ condition for spin 1 and 2, ω_r=$\Delta\omega^{\rm iso}_{12}$ and $\omega^{\rm ref}_B = \omega^{\rm ref}_P$ to generate a correlated spin state of the form

$$a\, I_{1+} I_{2z} I_{3+} + a^*\, I_{1-} I_{2z} I_{3-}$$

- Step $\mathbf{C}_1$: selective pulse on resonance with $\omega^{\rm ref}_C = \omega^{\rm iso}_2$ to generate TQC by rotating spin 2 by $\pi/2$ while leaving the states of spins 1 and 3 unmodified.

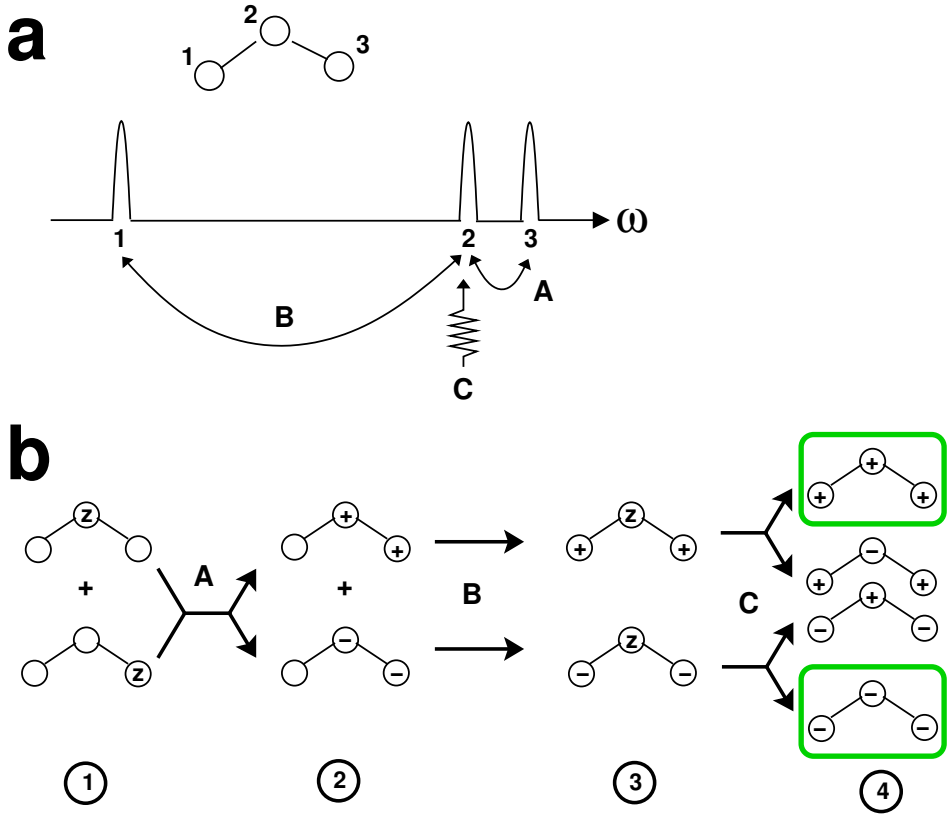

Figure 6.2: Spin state during the pulse sequence, using the time-point labelling specified in Fig. 6.1

- Step **E**: the TQ coherence is evolved with $\omega_E^{\text{ref}} = \omega_P^{\text{ref}}$ by adding a period $\tau_E = t_1$ of free evolution between blocks $\mathbf{C}_1$ and $\mathbf{C}_2$ to obtain a correlation between the TQ spectrum (indirect dimension) and TQ-filtered spectrum (not shown in Fig. 6.1.

- The TQ coherence is converted back in steps $\mathbf{C}_2$, $\mathbf{B}_2$ and $\mathbf{A}_2$ by reversing the order of the above blocks and applying the necessary phase corrections

- Step **R**: read pulse and acquisition, with $\omega_R^{\text{ref}} = \omega_P^{\text{ref}}$

The pulse sequence is graphically explained in Fig. 6.2, where we show the typical spin system for which such sequence is designed, together with the status of the density operator after each block. The presence of well resolved chamical shifts is a stringent requirement for this scheme to apply.

This block-wise scheme is very advantageous in that each block can be optimized individually. The optimal condition for the individual terms nearly correspon to the optimal condition for the whole experiments. It may be possible to improve the TQ efficiency slightly by refining the individual parameters on the TQ-filtered spectrum.

6.2.1 Phase Cycling

Blocks **P** to $\mathbf{C}_1$ are phase cycled in six steps to select TQ-coherences. Block **R** undergoes a 4-step phase cycle to achieve a z-filter. The duration of the rotational resonance evolution locks $\mathbf{B}_1$ and $\mathbf{B}_2$ were both contrained to be equal to a half integer multiple of the rotor period, τ_r. The phase cycle can be written as

$$\begin{aligned} \phi_P = \phi_{A_1} = \phi_{B_1} = \phi_{C_1} &= \frac{2\pi k_2}{6} + \frac{\pi}{6}k_1 + \frac{2}{3}\omega_r t_1, \\ \phi_{A_2} = \phi_{B_2} = \phi_{C_2} &= 0, \\ \phi_R &= \frac{\pi}{2}\text{floor}\left(\frac{k_2}{6}\right), \\ \phi_{rec} &= 0, \\ \phi_{dig} &= k_2\pi + \frac{\pi}{2}\text{floor}\left(\frac{k_2}{6}\right), \end{aligned} \tag{6.1}$$

were the k_2 is the transient counter, $k_2 = 0, \ldots, 23$, k_1 is the transient counter in the indirect dimension for 2D experiments ($t_1 = k_{t_1}$=0 in the 1D case) and the function floor(x) returns the largest integer not greater than x, as defined in Ref. 52. In the TQ excitation block (**P** to $\mathbf{C}_1$) the phase dependence upon t_1 includes a $\pi k_1/6$ term for TPPI[13] to obtain 2D data sets with pure absorption lineshape. The additional term, $2\omega_r t_1/3$, compensates the incremental phase shift in blocks $\mathbf{A}_2$ and $\mathbf{B}_2$ due to the time-phase relationship already discussed in Sect 3.5.

Step A: Selective DQ excitation

Block $\mathbf{A}_1$ of the pulse sequence consists of a recoupling sequence for converting sum longitudinal magnetization of spins 2 and 3 into DQ coherence between spins 2 and 3. This task is achieved using an R-sequence for pure dipolar DQ recoupling, with suppression of CSA and rf inhomogeneities to first order. In the experiments shown here, we chose the symmetry $\text{R}14_4^5$ because it allows efficient DQ dipolar recoupling at the spinning frequency imposed by the $n = 1$ RR condition and moderate rf field on the ^{13}C channel. The use of the basic element R= 180_0 guarantees DQ excitation within a narrow band-width around the carrier frequency and only excites spins 2 and 3, leaving spin 1 untouched. This is demonstrated by simulations in Fig 6.3 and experimentally in Fig. 6.5c for the symmetry $\text{R}14_4^5$ on rotational resonance, ω_r=$\Delta\omega_{12}^{\text{iso}} = |\omega_1 - \omega_2|/2\pi$. The DQ coherence is excited between two of the three spins with a low power, non-compensated R sequence (see Sect. 3.4, Papers I and II) with an experimental efficiency of 39% with respect to the three-spin system. This is very close to the maximum theoretical efficiency for selective DQ excitation over a three-spin system, which is $73\% \times 2/3 = 48.7\%$. An additional advantage of the simple π pulse is that it gives a very fast DQ build-up, as can be seen by a direct comparison of the scaling factor for the $\text{R}N_n^\nu$ sequences with a straight 180_x and 90_0270_π, thereby minimizing losses related to relaxation of the spin system. Given the high-selectivity of the DQ excitation, only two of the three spins are involved at this stage and, using the notation from Figs. 6.1 and 6.2a and Paper IV, we can write the density operator the end of the interval

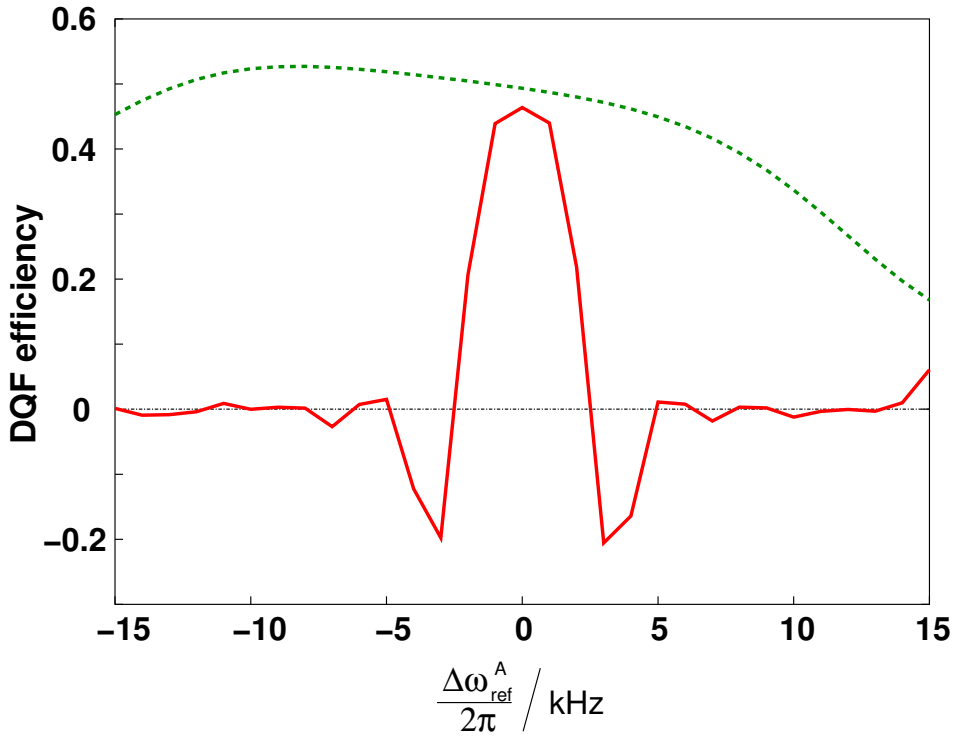

Figure 6.3: DQ excitation profile for [U-^{13}C]-*L*-alanine at 9.4 T, $\omega_r/2\pi = 12.750$ Hz as a function of the carrier frequency offset $\Delta\omega^A_{\mathrm{ref}} = \omega^A_{\mathrm{ref}} - (\omega^{\mathrm{iso}}_2 + \omega^{\mathrm{iso}}_3)/2$, using the R symmetry $\mathrm{R}14^5_4$ and two different R elements, $\mathrm{R}^0 = 180_0$ (solid line) and $\mathrm{R}^0 = 90_0270_{180}$ (dotted line). In order to maintain the same spinning frequency in the two simulations, the nutation frequency of the rf field equals $|\omega^S_{\mathrm{nut}}/2\pi|$ =22.3 kHz for the simple 180_0 pulse and 44.6 kHz for the sequence using the composite pulse 90_0270_{180}. The DQF efficiency is defined with respect to the total longitudinal magnetization for the three-spin system

A_1

$$\rho_{②} \approx (S_{2z} + S_{3z}) \cos|\omega_A \tau_A| + S_2^+ S_3^+ i e^{i\phi_A} \sin|\omega_A \tau_A| - S_2^- S_3^- i e^{-i\phi_A} \sin|\omega_A \tau_A| \ldots (6.2)$$

where the effective dipolar recoupling amplitude ω_A depends upon the orientational angles, the dipolar coupling constant as

$$\omega_A = b_{23}\kappa_{2-122} \sum_{m=-2}^{2} d^2_{0m}(\theta) D^2_{m-1}(\Omega_{MR}) \exp\left\{ i(\alpha^0_{RL} - \omega_r t_{①}) \right\} \quad (6.3)$$

and

$$\omega_A = |\omega_A| e^{i\phi_A} \quad (6.4)$$

$$\phi_A(\gamma_{MR}) = \phi^0_A + \gamma_{MR} \quad (6.5)$$

since the $\{l, m, \lambda, \mu\} = \{2, -1, 2, 2\}$ and $\{2, 1, 2, -2\}$ space-spin components are selected by $R14^5_4$, then

Step B: Rotational Resonance three-spin Evolution

The two-spin DQ coherence is transformed into a correlated three-spin state using free evolution under $n = 1$ rotational resonance between spins 1 and 2. This constrains the spinning frequency for the experiment to match the chemical shift difference of the sites to be recoupled, $\omega_r = \Delta\omega_{12}$.

Rotational resonance is known to possess a pure, narrow-band, zero-quantum (ZQ) Hamiltonian. This is confirmed by full numerical simulation, measuring the selectivity of the zero-quantum Hamiltonian by monitoring the ZQ transfer efficiency for a transfer of polarization from spin 1 of *L*-alanine to the other two spins, as shown in Fig. .

This selectivity semplifies the calculation of the evolution of the three-spin density operator during the interval **B**. The propagation operator for the spin system over the interval τ_B may be written as follows:

$$U_B \approx U^0_B(t_{③}) \exp\{-i\bar{\mathcal{H}}_B \tau_B\} U^0_B(t_{②}) \quad (6.6)$$

where the recoupled ZQ Hamiltonian during the RR interval **B** is

$$\bar{\mathcal{H}}_B \approx \frac{1}{2} \left(\omega_B S_1^+ S_2^- + \omega_B^* S_1^- S_2^+ \right) \quad (6.7)$$

and, as in step **A**, we can express the ZQ amplitude and its phase as

$$\omega_B = |\omega_B| e^{i\phi_B} \quad (6.8)$$

$$\phi_B(\gamma_{MR}) = \phi^0_B + \gamma_{MR} \quad (6.9)$$

This is of great advantage, as both sequences in blocks **A** and **B** have the same orientational dependence and that guarantees that no destructive interference takes place between the two blocks. It is possible to derive some commutation relationships which help dealing with the evolution of the density operator analytically (see Paper IV), leading to

$$\rho_{③} \approx -2\, e^{i(\phi_A + \phi_B)} \sin|\omega_A \tau_A| \sin|\omega_B \tau_B| \left(S_1^+ S_{2z} S_3^+ + S_1^- S_{2z} S_3^- \right) + \ldots \quad (6.10)$$

The DQ coherence between spins 2 and 3 are converted into DQ coherences between spins 1 and 3, antiphase with respect to 2.

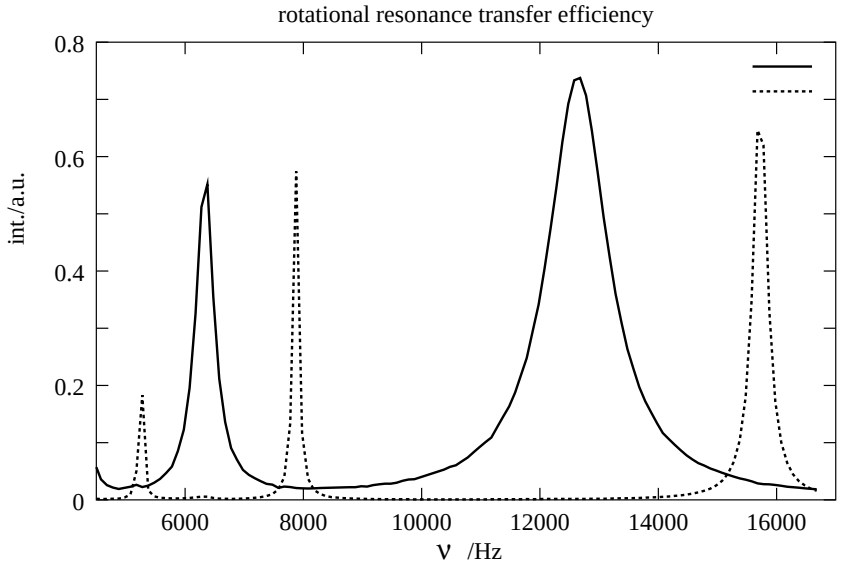

Figure 6.4: Polarization transfer curve at 9.4 T from S_1 to S_2 (solid line) and S_3 (dotted line), in arbitrary units. In particular, the solid curve shows a peak at ω_r=$\Delta\omega_{12}$ which indicates a good transfer efficiency within a bandwidth of about $\pm$100 Hz from the resonance conditions.

Step 3 : Selective Pulse

Robust selective pulses are available for inversion and selective excitation (by destroying the signal from the non-selected spins). We need a selective pulse such that the state of spin 2 is rotated by 90° while the other spins are unaffected.

A simple sequence that can achieve this task is $90_\Phi 90_0$. Each 90° pulse has the duration of one rotor period and this is the shortest (non-shaped) frequency selective pulse we found in our numerical search. To understand this pulse sequence, it is convenient to consider the off-resonance Hamiltonian (made up by the rf terms and the isotropic chemical shifts for each of the three spins) for three one-spin systems separately and calculate the corresponding Euler angles, $\Omega_{C(j)}$. In this framework, spin 2 is subjected to a perfect 90°rotation. Spin 1 ($\Omega_C^{(1)} = \{124.3^o, 4.1^o, -145.7^o\}$) and spin 3 ($\Omega_C^{(3)} = \{53.4^o, 16.3^o, 143.4^o\}$) experience a small transverse rotation and their propagators mainly induce a z rotation of the spin state. When acting on the anti-phase DQ coherence,

$$\begin{aligned} U_C S_1^+ S_{2z} S_3^+ U_C^\dagger &= \frac{1}{8}(1+\cos\beta_C^{(1)})(1+\cos\beta_C^{(3)})\sin\beta_C^{(2)} S_1^+ S_2^+ S_3^+ \\ &\quad \exp\{-i*(\alpha_C^{(1)}+\gamma_C^{(1)}+\alpha_C^{(3)}+\gamma_C^{(3)}+\alpha_C^{(2)})\}+\ldots \quad (6.11) \end{aligned}$$

The selective pulse is demonstrated on a state of longitudinal magnetization in Fig. 6.5b. Here the selective pulse sequence is applied over a state of enhanced longitudinal magnetization (created by ramped-CP followed by a strong 90°pulse) and the ratio between the integrated signal in the spectra Fig. 6.5b and Fig. 6.5a results a 97% efficiency of the pulse sequence. The performance of this pulse sequence on the full three-spin system has also been inferred by simulation, monitoring the transfer efficiency between the TQ state and the DQ antiphase state

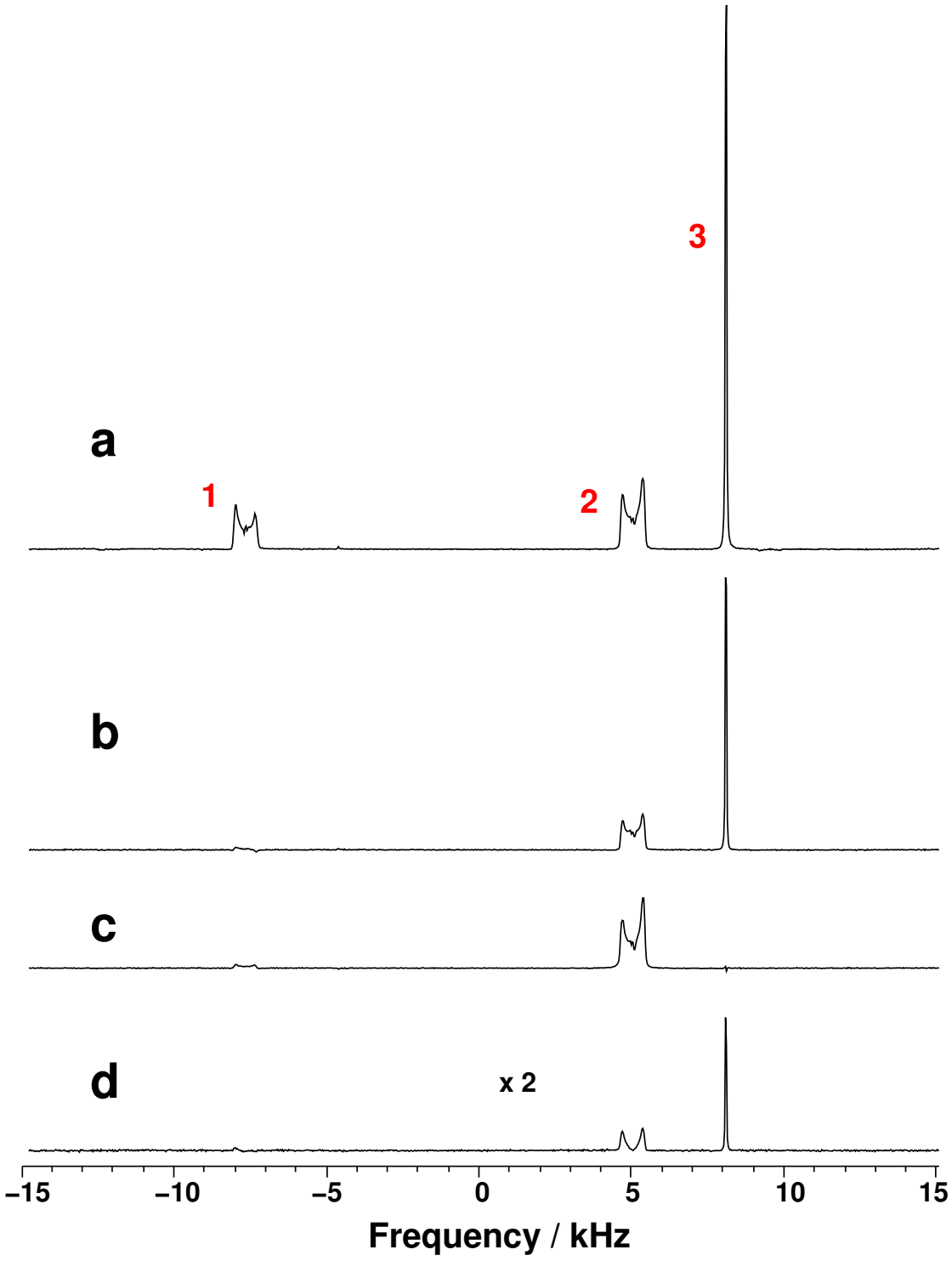

Figure 6.5: Experimental spectra for U-^{13}C-*L*-alanine at 9.4 T, $\omega_r/2\pi$=12.750 kHz, 24 transients each: (a) ramped-CP; (b) DQF spectrum, corresponding to 39% efficiency; (c) Selective pulse demonstration; (d) TQF spectrum, corresponding to 8.7% efficiency with respect to the total longitudinal magnetization

created immediately after period **C**.

As also verified experimentally, the composite pulses used for TQ excitation and reconversion are sensitive to the sign of the phase, on the contrary of many other sequences. This requires a knowledge of the rf hardware in order to know how the phases are generated. If this is not known by the user, it is convenient to use a trial-and-error approach to the problem, comparing the performance of the pulse sequences using both positive and a negative sign of the input phases within the TQ sequence. Only one set of phases will perform well.

6.3 Triple-Quantum Coherence on Model Systems

The TQ-filtered spectrum of alaline is shown in Fig. 6.5. A two-dimensional experiment comparing the indirect TQ dimendion and the direct SQ dimension has been acquired with TPPI[13] on U-^{13}C-*L*-alanine, 98%, as shown in Fig. 6.6. The TQ coherence is allowed to evolve under continuous ^{1}H spin decoupling. As can be seen, the indirect dimension contains one single peak, the unique TQ peak for the TQ coherence is visible. The peak is at the sum of the isotropic chemical shifts, as expected. There is no evidence of other possible TQ peaks deriving from intermolecular contacts, due to the high specificity of the sequence and the short duration of each block, i.e., only short range interaction are reintroduced. The phases in the reconversion block of the R sequence are affected by the presence of the TQ evolution interval. As pointed out many times, the R sequences give rise to a z rotation modulating the interaction Hamiltonian in the interaction frame. The presence of a time delay for t_1 incrementation needs to be compensated by shifting the relative phase of the reconversion block[66] by a quantity which depends on the time interval t_1 and on the recoupled spin-space component. A similar effect is observed in the RR period ($\mu = 0$). The total phase correction in Eq. 6.1 includes both effects.

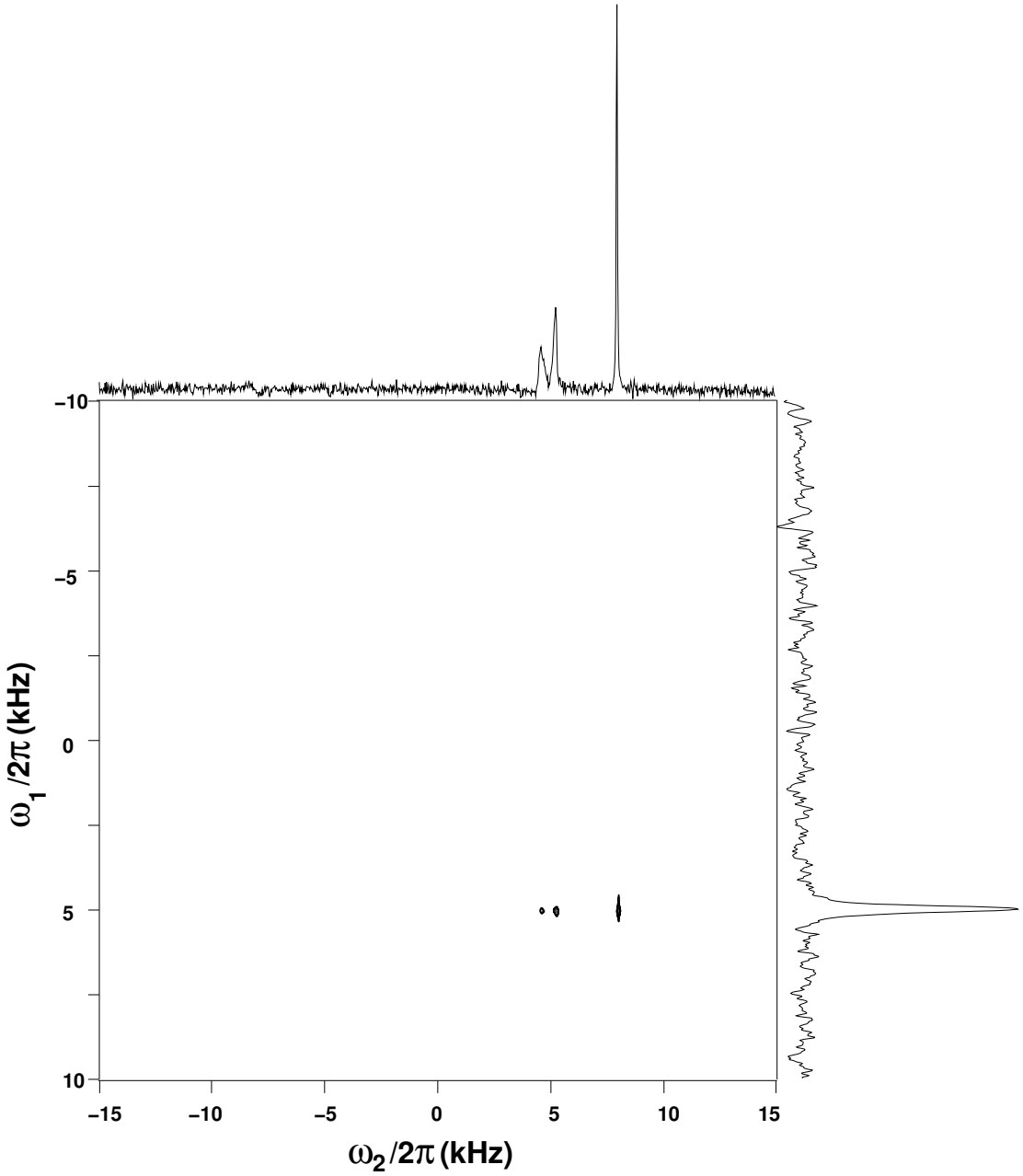

Figure 6.6: Experimental 2D correlation spectrum correlationg between triple-quantum and siggle-quantum dimensions. The unique TQ peak using 1024 t_1 increments with a step of 25 μs and 6 transients per t_2 slice.

Chapter 7

Concluding Remarks

7.1 Conclusions

The theory presented here is a summary of general NMR concepts and of how they can be applied for developing new experiments in solid-state NMR. The work here exploits multiple-quantum filtration over ^{13}C spin systems and therefore sample labelling is an unavoidable requirement. Extension to other spin-1/2 systems is possible.

Some of the tricks to improve the performance of symmetry-based pulse sequences are discussed, with particular attention towards high-order terms and supercycling. The improvement in double-quantum efficiency is of great importance as this correlated spin state is a key step in many NMR experiment that lead to structural information.

We introduce a roboust method for measuring bond lengths on ^{13}C-^{13}C spin pairs and demonstrate it on a series of model compounds. The NMR data are in good agreement with diffraction data.

The technique for distance measurement is demonstrated on the dark state of the photoreceptor rhodopsin to determine the bond lengths within the conjugated chain of the chromophore. These data are expected to have a big impact on the understanding of the protein functions. Future work on this system will help clarifying the mechanism of the primary photoreaction and the way that the energy of the incident photon is stored so efficiently.

This stresses the importance of solid state NMR for precise determination of structural details in biomolecules, where the precision of diffraction studies is normally much worse.

An extension to excitation of multiple-quantum coherences of order 3 is undertaken, with an improvement in the triple-quantum filtering efficiency for coupled ^{13}C systems under magic-angle spinning. Applications on proteins are in progress but no data are yet available.

7.2 Acknowledgements

First of all, I want to thank my supervisor Malcolm Levitt, for the new solid-state world he made me discover, for being a continuos source of scientific curiosity, for helping me with his guidance and always with a friendly attitude.

Thanks to the old group members and to the new ones. We had a very good time together, both at work and not ... as you can guess from these images below!

A big thanks to my office-mates in Stockholm: Mattias, Xin and Colan, for being understanding and for not complaining too much about the "background noise" coming from my working place. Thanks to Mattias, for being so supportive in the first period of my PhD. Xin, for being always ready to listen and for being so nice to work with, as I had a chance to really appreciate in the last year. Colan, for being my "spell-checker" in drafts and conversation, for being always willing to have a chat or a beer and for trying to make my work methodology a little more organized.

Thanks to Andreas, for nice chats, for the experimental crash course in which he showed me how to set up some the experiments that I used so much later on and also for being the first target for tickling. Luckily, we have Madhu in the group now...

Thanks to Ole, for fixing all sorts of technical problems with instruments and computer, for his friendship through the years, the sport discussions and for watching with me so many football matches.

I need to acknowledge people who supported me with their friendship, in particular Pratima for being such a dear friend and for all the good times we shared in Stockholm. Maria and David, for lovely evenings out, midsommar trips and for maintaining this friendship alive also now that I am not in Sweden anymore.

Thanks to Jörn for the nice cooperation we had lately, for cheering me up in some bad times and for some lovely day I spent in his home town for a very special occasion.

Thanks to Henrik for showing me that working in an organic chemistry lab can be enjoyable when you are in good company.

It is a great pleasure to have Linda and Natala in the group since it really needed more of a female side. Natala brought in the group the youngest group member, Stefan!

Apart from my group, there are many people in the depertment of Physical

Chemistry who have been helpful and supportive through the years. Thanks to Arvid and Henrik for helping me learn some swedish. Thanks to the morning-coffee group, in particluar Jonas, Per-Erik, Arnold, Dick, Jozef and Ann-Britt. Thanks to Mattias, Per-Erik, Ann-Britt and Jozef, for helping me sorting out things for my thesis.

Grazie alla mia famiglia, per avermi dato un enorme appoggio morale durante tutti questi anni lontana da casa e per la vostra capacità di darmi un bel sorriso in risposta anche quando non ne avete molta voglia. Il mio pensiero è rivolto in particolare verso papà, mamma e nonna (giú).

La lontananza è compensata in parte da frequenti telefonate e viaggetti verso la mia città.

Grazie a tutti i miei amici e parenti per aver mantenuto un profondo legame con me nonostante la distanza ed i pochi incontri: la lontananza non demolisce relazioni con delle forti basi.

Grazie a Longeri per avermi fatto apprezare la disciplina che studio tuttora, per l'appoggio, la comprensione, l'essenziale spinta iniziale per farmi muovere da Cosenza (altrimenti sarei di certo lì) e per una lettura molto attenta e critica della tesi.

Appendix A

Operators

A.1 Definitions

In mathematical terms, an operator is a mapping. Most of the operators we will be working with are also linear. If T is a linear operator and $\mathcal{D}(T)$ is the space on which it is defined, then

$$\begin{aligned} T(x+y) &= Tx + Ty & \text{(A.1)} \\ T(\alpha x) &= \alpha T x \qquad \forall x, y \in \mathcal{D}(T) & \text{(A.2)} \end{aligned}$$

where α is a scalar. All the treatment that follows is intended to be for linear vector spaces. Without being too formal, it is useful to introduce some definitions, i.e.,

- $\mathbb{I}$ is the identity operator
- the adjoint of an operator A is defined as the transpose of the complex conjugate of A, and indicated as

$$A^\dagger = (A^*)^T = (A^T)^* \tag{A.3}$$

- a linear operator A is called Hermitian, or self-adjoint, if

$$A = A^\dagger \tag{A.4}$$

- a operator is unitary if

$$U^{-1} = U^\dagger \tag{A.5}$$

- the commutator between two operators A and B is defined as

$$[A, B] = AB - BA \tag{A.6}$$

  Two operators are said to commute if their commutator vanishes

- the anticommutator between two operators A and B is defined as

$$\{A, B\} = AB + BA \tag{A.7}$$

It is possible to build functions of operators and their definition is usually related to the Taylor series expansion of the function itself. For instance, the exponential of an operator e^A can be defined as

$$e^A = \sum_{n=0}^{\infty} A^n/(n!) \tag{A.8}$$

Operators are often expressed in matrix form and, as matrices, they do not generally commute. In order to express an operator in matrix form, it is essential to have a complete set spanning the whole space $\mathcal{D}(A)$. This form is particularly useful when this complete basis set, $\{f_n\}$, is finite in size, or at least countable. The matrix representation of A is then

$$A_{mn} = \int_{\mathcal{D}(A)} f_m^* A f_n d\tau \tag{A.9}$$

where $d\tau$ is a volume element of $\mathcal{D}(A)$.

A.2 Dirac Notation

The Dirac notation leads to a great simplification of the formulae. In this formalism, we have

$$\langle m|n\rangle = \int f_m^* f_n d\tau \tag{A.10}$$

$$\langle m| A |n\rangle = \int f_m^* A\, f_n d\tau \tag{A.11}$$

where $\langle m|$ is called "bra" and is the complex conjugate (or adjoint, if using matrix notation) of the function, $|n\rangle$ is called "ket" and is the function itself, and the two bra-ket terms together imply the computation of the scalar product according to the metric of the space, in this case the integration, by hypothesis.

A.3 Eigenvalue Problems and Observables

It is often convenient to work in a basis which makes the operator A diagonal. The basis set in this case is given by the (complete) set of eigenfunctions of the operator

$$A\,|n\rangle = a_n\,|n\rangle \tag{A.12}$$

If the operator A is expressed in a matrix form with respect to a basis different from its eigenbasis, then the eigenvalues and eigenvectors are obtained by solving the problem

$$(A - \Lambda\mathbb{I})X = 0 \tag{A.13}$$

where Λ is a diagonal matrix whose diagonal elements are the eigenvalues, while X is made up of the eigenvectors. For Hermitian operators, all eigenvalues are real and the eigenvectors are orthogonal (or can be made such). All physical property which are observables are described by Hermitian operators, by hypothesis, and the only possible results of a measurement of the observable associated with A is one of its eigenvalues. If the function describing the state of the system is not an eigenfunction, there is no certain prediction of the measurement result in an individual case, but is still possible to compute the average value $< A >$ of the property in many identical observations, namely

$$< A >= \frac{\langle\psi| A |\psi\rangle}{\langle\psi|\psi\rangle} \tag{A.14}$$

All these formulae are extensively used throughout this thesis to compute NMR observables.

A.4 Single-Transition Operators

Single-transition operators[152] are spin operators connecting specific energy eigenstates and they are labelled according to what transitions they refer to. For instance, the single transition shift operators connecting states r and s are defined as

$$I_{+}^{(rs)} = I_{x}^{(rs)} + i\, I_{y}^{(rs)} = |r\rangle \langle s| \tag{A.15}$$

$$I_{-}^{(rs)} = I_{x}^{(rs)} - i\, I_{y}^{(rs)} = |s\rangle \langle r| \tag{A.16}$$

On the other hand, the diagonal terms correspond to populations and are represented by projection operators of the form

$$I^{rr} = |r\rangle \langle r| \tag{A.17}$$

The easiest way to build the single transition operators is usually to start from the ket-bra multiplication of the basis functions in their vector form, and then derive all relevant operators from these. In general, it is possible to represent MQ coherences of any order with this formalism. The single transition shift operator $I_{\pm}^{rs}$ connects states with $\Delta M = \pm(M_r - M_s)$. This formalism is of great help when dealing with spin pairs, allowing one to simplify a real two-spin system into a ficticious spin-1/2 system. For instance, if we label the states as $\{|\alpha\alpha\rangle, |\alpha\beta\rangle, |\beta\alpha\rangle, |\beta\beta\rangle\} = \{|1\rangle, |2\rangle, |3\rangle, |4\rangle\}$ we can describe many of the properties of ZQ coherences by just considering states $|2\rangle$ and $|3\rangle$, while DQ coherences involve a correlation between states $|1\rangle$ and $|4\rangle$.

Appendix B

More on tensors and rotations

B.1 Wigner Matrices

The general form of Wigner matrices of rank l is

$$D^l_{mm'}(\Omega) = e^{-im\alpha} d^l_{mm'}(\beta) e^{-im'\gamma} \tag{B.1}$$

The explicit forms of the reduced Wigner matries are given below, using a short notation "c" and "s" to indicate cosine and sine functions:

$$d^1 = \begin{pmatrix} (1+\mathrm{c}\beta)/2 & -\mathrm{s}\beta/\sqrt{2} & (1-\mathrm{c}\beta)/2 \\ \mathrm{s}\beta/\sqrt{2} & \mathrm{c}\beta & -\mathrm{s}\beta/\sqrt{2} \\ (1-\mathrm{c}\beta)/2 & \mathrm{s}\beta/\sqrt{2} & (1+\mathrm{c}\beta)/2 \end{pmatrix} \tag{B.2}$$

$$d^2 = \begin{pmatrix} \frac{(1+\mathrm{c}\beta)^2}{4} & -(1+\mathrm{c}\beta)\mathrm{s}\beta/2 & \sqrt{\frac{3}{8}}\mathrm{s}^2\beta & (1-\mathrm{c}\beta)\mathrm{s}\beta/2 & \frac{(1-\mathrm{c}\beta)^2}{4} \\ (1+\mathrm{c}\beta)\frac{\mathrm{s}\beta}{2} & \frac{-1+\mathrm{c}\beta}{2} + \mathrm{c}^2\beta & -\sqrt{\frac{3}{8}}\mathrm{s}2\beta & \frac{1+\mathrm{c}\beta}{2} - \mathrm{c}^2\beta & -(1-\mathrm{c}\beta)\frac{\mathrm{s}\beta}{2} \\ \sqrt{\frac{3}{8}}\mathrm{s}^2\beta & \sqrt{\frac{3}{8}}\mathrm{s}2\beta & (3\mathrm{c}^2\beta - 1)/2 & \sqrt{\frac{3}{8}}\mathrm{s}2\beta & \sqrt{\frac{3}{8}}\mathrm{s}^2 \\ (1-\mathrm{c}\beta)\frac{\mathrm{s}\beta}{2} & \frac{1+\mathrm{c}\beta}{2} - \mathrm{c}^2\beta & \sqrt{\frac{3}{8}}\mathrm{s}2\beta & \frac{-1+\mathrm{c}\beta}{2} + \mathrm{c}^2\beta & -(1+\mathrm{c}\beta)\frac{\mathrm{s}\beta}{2} \\ \frac{(1-\mathrm{c}\beta)^2}{4} & (1-\mathrm{c}\beta)\mathrm{s}\beta/2 & \sqrt{\frac{3}{8}}\mathrm{s}^2\beta & (1+\mathrm{c}\beta)\mathrm{s}\beta/2 & \frac{(1+\mathrm{c}\beta)^2}{4} \end{pmatrix} \tag{B.3}$$

The useful properties of Wigner matrices include

$$d^l_{m0} = (-)^m d^l_{-m0} \tag{B.4}$$

B.2 Spherical Representation of Tensors

When dealing with vecrors and tensors in this thesis, we often assume that they are expressed as column vectors, or in Dirac's notation as Kets. The matrix defining the transormation from the spherical basis $\{\langle +1|, \langle 0|, \langle -1|\}$ to the cartesian basis

$\{\langle e_x|, \langle e_y|, \langle e_z|\}$ can be obtained directly from the basis definition

$$\langle +1| = -\frac{1}{\sqrt{2}}(\langle e_x| - i\langle e_y|) \tag{B.5}$$

$$\langle 0| = \langle e_z| \tag{B.6}$$

$$\langle -1| = \frac{1}{\sqrt{2}}(\langle e_x| + i\langle e_y|) \tag{B.7}$$

$$\tag{B.8}$$

by taking the scalar product between elements of different bases and exploiting the completeness of each set, leading to

$$\mathbb{T} = \begin{pmatrix} -\frac{1}{\sqrt{2}} & \frac{i}{\sqrt{2}} & 0 \\ 0 & 0 & 1 \\ \frac{1}{\sqrt{2}} & \frac{i}{\sqrt{2}} & 0 \end{pmatrix} \tag{B.9}$$

All transformation are always intended within the same reference frame, if not otherwise specified. Some useful properties of spherical tensors are recalled here, together with the explicit form of the irreducible spherical tensors with respect to the Cartesian components:

$$|A\rangle_{lm} = (-1)^{l-m}|A\rangle^*_{l\,-m} \tag{B.10}$$

$$\left|A^{(0)}\right\rangle = -\frac{1}{\sqrt{3}}(a_{xx} + a_{yy} + a_{zz}) \tag{B.11}$$

$$\left|A^{(1)}\right\rangle = \begin{pmatrix} \frac{1}{2}(a_{xz} - a_{zx} + ia_{yz} - ia_{zy}) \\ \frac{i}{\sqrt{2}}(a_{yx} - a_{xy}) \\ \frac{1}{2}(a_{xz} - a_{zx} - ia_{yz} + ia_{zy}) \end{pmatrix} \tag{B.12}$$

$$\left|A^{(2)}\right\rangle = \begin{pmatrix} \frac{1}{2}(a_{xx} - a_{yy} + ia_{xy} + ia_{yx}) \\ -\frac{1}{2}(a_{xz} + a_{zx} + ia_{yz} + ia_{zy}) \\ -\frac{1}{\sqrt{6}}(a_{xx} + a_{yy}) + \sqrt{\frac{2}{3}}a_{zz} \\ \frac{1}{2}(a_{xz} + a_{zx} - ia_{yz} - ia_{zy}) \\ \frac{1}{2}(a_{xx} - a_{yy} - ia_{xy} - ia_{yx}) \end{pmatrix} \tag{B.13}$$

When it comes to rotations, it is conventional to notate rotation matrices in a Cartesian basis by $R(\theta, \mathbf{n})$, while the corresponding rotation in a spherical basis are the Wigner matrices. If the rank-J tensor A is in its irreducible spherical form, then it transforms from frame F to F' as

$$\left\langle A^{(J)}\right|^{F'} = \left\langle A^{(J)}\right|^{F} D^J(\Omega_{FF'}) \tag{B.14}$$

For further information, see for instance Refs.[25]

B.3 Spin-1/2 Angular Momentum Operators

The spin-1/2 angular momentum operators are proportional to the Pauli matrices, which are an important tool in modern quantum physics and they constitute the

basis for the matrix representation of the wavefunction and Hamiltonian in NMR.[52] Below are listed the matrix representations for single spin-1/2 operators

$$I_x = \frac{1}{2}\begin{pmatrix} 0 & 1 \\ 1 & 0 \end{pmatrix} = \frac{1}{2}\left(|\alpha\rangle\langle\beta| + |\beta\rangle\langle\alpha|\right) \tag{B.15}$$

$$I_y = \frac{1}{2i}\begin{pmatrix} 0 & 1 \\ -1 & 0 \end{pmatrix} = \frac{1}{2i}\left(|\alpha\rangle\langle\beta| - |\beta\rangle\langle\alpha|\right) \tag{B.16}$$

$$I_z = \frac{1}{2}\begin{pmatrix} 1 & 0 \\ 0 & -1 \end{pmatrix} = \frac{1}{2}\left(|\alpha\rangle\langle\alpha| - |\beta\rangle\langle\beta|\right) \tag{B.17}$$

$$I_+ = \begin{pmatrix} 0 & 1 \\ 0 & 0 \end{pmatrix} = |\alpha\rangle\langle\beta| \tag{B.18}$$

$$I_- = \begin{pmatrix} 0 & 0 \\ 1 & 0 \end{pmatrix} = |\beta\rangle\langle\alpha| \tag{B.19}$$

Bibliography

[1] M. E. Peskin and D. V. Schroeder, *An introduction to quantum field theory*, Addison-Wesley Pub, (1995).

[2] W. S. C. Williams, *Nuclear and Particle Physics*, Oxford University Press, (1991).

[3] M. Mehring, *Principles of High Resolution NMR in Solids*, Springer, Berlin, (1983).

[4] C. P. Slichter, *Principles of Magnetic Resonance*, Springer-Verlag, Berlin, (1992).

[5] I. J. Lowe, *Phys. Rev. Lett.* **2**(7), 285–287 (1959).

[6] A. E. Bennett, R. G. Griffin and S. Vega, *NMR Basic Princ. and Progr.* **33**, 1–77 (1994).

[7] S. Dusold and A. Sebald, *Ann. Rep. NMR Spectrosc.* **41**, 185–264 (2000).

[8] Y. K. Lee, N. D. Kurur, M. Helmle, O. G. Johannessen, N. C. Nielsen and M. H. Levitt, *Chem. Phys. Lett.* **242**(3), 304–309 (1995).

[9] M. Carravetta, M. Edén, A. Brinkmann, X. Zhao and M. H. Levitt, *Chem. Phys. Lett.* **321**, 205–215 (2000).

[10] C. M. Rienstra, M. E. Hatcher, L. J. Mueller, B. Sun, S. W. Fesik and R. G. Griffin, *J. Am. Chem. Soc.* **120**(41), 10602–10612 (1998).

[11] T. Gullion and J. Schaefer, *J. Magn. Reson.* **81**, 196–200 (1989).

[12] J. D. Gross, P. R. Costa and R. G. Griffin, *J. Chem. Phys.* **108**, 7286–7293 (1998).

[13] R. R. Ernst, G. Bodenhausen and A. Wokaun, *Principles of Nuclear Magnetic Resonance in One and Two Dimensions*, Clarendon Press, Oxford, (1988).

[14] S. R. Hartmann and E. L. Hahn, *Phys. Rev.* **128**, 2042–2053 (1962).

[15] G. Metz, X. Wu and S. O. Smith, *J. Magn. Reson. A* **110**, 219–227 (1994).

[16] J. H. Davis and M. Auger, *Progr. Nucl. Magn. Res. Spectr.* **35**, 1–84 (1999).

[17] R. G. Griffin, *Nat. Struct. Biol.* **5**, 508–512 (1998).

[18] N. Tjandra and Bax, *Science* **278**, 1111 (1997).

[19] C. A. Fowler, F. Tian, H. M. Al-Hashimi and J. H. Prestegard, *J. Mol. Biol.* **304**, 447 (2000).

[20] K. Nomura, K. Takegoshi, T. Terao, K. Uchida and M. Kainosho, *J. Biomol. NMR* **17**, 111–123 (2000).

[21] C. M. Rienstra, L. Tucker-Kellogg, C. P. Jaroniec, M. Hohwy, B. Reif, M. T. McMahon, B. Tidor, T. Lozano-Perez and R. G. Griffin, *P. Natl. Acad. Sci. USA* **99**, 10260 (2002).

[22] B. J. van Rossum, E. A. M. Schulten, J. Raap, H. Oschkinat H and H. J. M. de Groot, *J. Magn. Reson.* **155**, 1–14 (2002).

[23] F. M. Marassi and S. J. Opella, *J. Magn. Reson.* **144**, 150–155 (2000).

[24] M. Hong, *J. Am. Chem. Soc.* **122**, 3762–3770 (2000).

[25] M. E. Rose, *Elementary Theory of Angular Momentum*, John Wiley & Sons, Inc, (1957).

[26] L. Frappat, A. Sciarrino and P. Sorba, *A dictionary on Lie algebras and superalgebras*, Academic Press, London, (2001).

[27] R. Slansky, *Physc. Rep.* **79**, 1 (1981).

[28] I. N. Levine, *Quantum Chemistry*, Prentice-Hall, (1991).

[29] U. Haeberlen, *High Resolution NMR in Solids, Adv. Magn. Res.*, Suppl. 1, (1976).

[30] K. Schmidt-Rohr and H. W. Spiess, *Multidimensional Solid-State NMR and Polymers*, Academic Press, London, (1996).

[31] M. M. Maricq and J. S. Waugh, *J. Chem. Phys.* **70**, 3300–3316 (1979).

[32] M. H. Levitt, D. P. Raleigh, F. Creuzet and R. G. Griffin, *J. Chem. Phys.* **92**, 6347–6364 (1990).

[33] E. P. Wigner, *Group Theory & Application to the Quantum Mechanics of Atomic Spectra*, Academic Press, New York, (1988).

[34] W. S. Veeman, *Progr. Nucl. Magn. Res. Spectr.* **16**, 193 (1984).

[35] S. P. Brown, M. Perez-Torralba, D. Sanz, R. M. Claramunt and L. Emsley, *J. Am. Chem. Soc.* **124**, 1152–1153 (2002).

[36] D. P. Raleigh, M. H. Levitt and R. G. Griffin, *Chem. Phys. Lett.* **146**, 71–76 (1988).

[37] P. R. Costa, B. Q. Sun and R. G. Griffin, *J. Am. Chem. Soc.* **119**, 10821 (1997).

[38] M. Bechmann, X. Helluy and A. Sebald, *J. Magn. Reson.* **152**, 14 (2001).

[39] S. Dusold, H. Maisel and A. Sebald, *J. Magn. Reson.* **141**, 78 (1999).

[40] P. J. E. Verdegem, P. H. M. Bovee-Geurts, W. J. de Grip, J. Lugtenburg and H. J. M. de Groot, *Biochem.* **38**, 11316–11324 (1999).

[41] A. E. McDermott, F. Creuzet, R. Gebhard, K. van der Hoef, M. L. Levitt, J. Herzfeld, J. Lugtenburg and R. G. Griffin, *Biochem.* **33**, 6129 (1994).

[42] M. Ernst, A. Verhoeven and B. H. Meier, *J. Magn. Reson.* **130**, 176 (1998).

[43] A. E. Bennett, C. M. Rienstra, M. Auger, K. V. Lakshmi and R. G. Griffin, *J. Chem. Phys.* **103**, 6951–6958 (1998).

[44] A. Bielecki, A. C. Kolbert, H. J. M. de Groot, R. G. Griffin and M. H. Levitt, *Adv. Magn. Res.* **14**, 111 (1990).

[45] M. Edén and M. H. Levitt, *J. Chem. Phys.* **111**, 1511–1519 (1999).

[46] A. Detken, E. H. Hardy, M. Ernst and B. H. Meier, *Chem. Phys. Lett.* **356**, 298–304 (2002).

[47] M. Lee and W. I. Goldburg, *Phys. Rev. A* **140**, 1261–1271 (1965).

[48] W. K. Rhim, D. D. Elleman and R. W. Vaughan, *J. Chem. Phys.* **59**, 3740–3749 (1973).

[49] E. Vinogradov, P. K. Madhu and S. Vega, *Chem. Phys. Lett.* **314**, 443 (1999).

[50] E. Vinogradov, P. K. Madhu and S. Vega, *Chem. Phys. Lett.* **354**, 193 (2002).

[51] P. K. Madhu, X. Zhao and M. H. Levitt, *Chem. Phys. Lett.* **346**, 142–148 (2001).

[52] M. H. Levitt, *Spin Dynamics. Basics of Nuclear Magnetic Resonance*, Wiley, (2001).

[53] J. Jeener, *Adv. Magn. Res.* **10**, 1 (1982).

[54] U. Haeberlen and J. S. Waugh, *Phys. Rev.* **175**, 453–467 (1968).

[55] W. Magnus, *Commun. Pure Appl. Math.* **7**, 649–673 (1954).

[56] A. D. Bain and R. S. Dumont, *Conc. Magn. Res.* **13**, 159 (2001).

[57] T. S. Untidt and N. C. Nielsen, *Phys. Rev. E* **65**, 021108–1–17 (2002).

[58] Zaremba, *Ann. Mat. Pura Appl.* **4-54**, 325 (1966).

[59] H. Conroy, *J. Chem. Phys.* **47**, 5307 (1967).

[60] M. Bak and N. C. Nielsen, *J. Magn. Reson.* **125**, 132–139 (1997).

[61] M. Edén, Y. K. Lee and M. H. Levitt, *J. Magn. Reson. A* **120**, 56–71 (1996).

[62] M. Hohwy, H. Bildsøe, H. J. Jakobsen and N. C. Nielsen, *J. Magn. Reson.* **136**, 6–14 (1999).

[63] M. Bak, J. T. Rasmussen and N. C. Nielsen, *J. Magn. Reson.* **147**, 296–330 (2000).

[64] M. H. Levitt, *Encyclopedia of Nuclear Magnetic Resonance: Supplementary Volume* pages 165–196 (2002).

[65] M. Hohwy, H. J. Jakobsen, M. Edén, M. H. Levitt and N. C. Nielsen, *J. Chem. Phys.* **108**, 2686–2694 (1998).

[66] A. Brinkmann and M. H. Levitt, *J. Chem. Phys.* **115**, 357–384 (2001).

[67] X. Feng, M. Edén, A. Brinkmann, H. Luthman, L. Eriksson, A. Gräslund, O. N. Antzutkin and M. H. Levitt, *J. Am. Chem. Soc.* **119**, 12006–12007 (1997).

[68] M. Edén and M. H. Levitt, *Chem. Phys. Lett.* **293**, 173–179 (1998).

[69] T. Karlsson, A. Brinkmann, P. J. E. Verdegem, J. Lugtenburg and M. H. Levitt, *Solid State NMR* **14**, 43–58 (1998).

[70] J. C. C. Chan, *J. Magn. Reson. A* **335**, 289–297 (2001).

[71] A. S. D. Heindrichs, H. Geen, C. Giordani and J. J. Titman, *Chem. Phys. Lett.* **335**, 89–96 (2001).

[72] A. Brinkmann, M. Edén and M. H. Levitt, *J. Chem. Phys.* **112**(19), 8539–8554 (2000).

[73] A. Brinkmann, unpublished results.

[74] X. Zhao, M. Edén and M. H. Levitt, *Chem. Phys. Lett.* **342**, 353–361 (2001).

[75] X. Zhao, J. L. Sudmeier and W. W. Bachovchin et al., *J. Am. Chem. Soc.* **123**, 11097–11098 (2001).

[76] A. Brinkmann, J. Schmedt auf der Günne and M. H. Levitt, *J. Magn. Reson.* **156**, 79–96 (2002).

[77] M. Carravetta, M. Edén, O. G. Johannessen, H. Luthman, P. J. E. Verdegem, J. Lugtenburg, A. Sebald and M. H. Levitt, *J. Am. Chem. Soc.* **123**, 10628–10638 (2001).

[78] J. C. C. Chan and G. Brunklaus, *Chem. Phys. Lett.* **349**, 104 (2001).

[79] M. H. Levitt, T. G. Oas and R. G. Griffin, *Isr. J. Chem.* **28**, 271–282 (1988).

[80] D. M. Gregory, D. J. Mitchell, J. A. Stringer, S. Kiihne, J. C. Shiels, J. Callahan, M. A. Mehta and G. P. Drobny, *Chem. Phys. Lett.* **246**, 654–663 (1995).

[81] M. A. Mehta, D. M. Gregory, S. Kiihne, D. J. Mitchell, M. E. Hatcher and J. C. Shiels, *Solid State Nucl. Magn. Res.* **7**, 211 (1996).

[82] S. Kiihne, M. A. Mehta, J. A. Stringer, D. M. Gregory, J. C. Shiels and G. P. Drobny, *J. Phys. Chem. A* **102**, 2274–2282 (1998).

[83] S. Kiihne, K. B. Geahigan, N. A. Oyler, H. Zebroski, M. A. Mehta and G. P. Drobny, *J. Phys. Chem. A* **103**, 3890–3903 (1998).

[84] Y. Ishii, *J. Chem. Phys.* **114**, 8473–8483 (2001).

[85] A. E. Bennett, C. M. Rienstra, J. M. Griffiths, W. Zhen, P. T. Lansbury and R. G. Griffin, *J. Chem. Phys.* **108**, 9463–9479 (1998).

[86] M. Hohwy, C. M. Rientra, C. P. Jaroniec and R. G. Griffin, *J. Chem. Phys.* **110**, 7983–7992 (1999).

[87] J. R. Long, N. Oyler, J. Popham, P. S. Stayton and G. P. Drobny, Double Quantum Spectroscopy of weakly coupled spins, in *43rd Experimental Nuclear Magnetic Resonance Conference*, 2002.

[88] J. Schmedt auf der Günne, unpublished results.

[89] Y. Ishii, T. Terao and S. Hayashi, *J. Chem. Phys.* **107**, 2760–2774 (1997).

[90] J. Kaski, P. Lantto, J. Vaara and J. Jokisaari, *J. Phys. Chem.* **120**, 3993–4005 (1998).

[91] C. Glaubitz and A. Watts, *J. Magn. Reson.* **130**, 305–316 (1998).

[92] C. Glaubitz, *Conc. Magn. Res.* **12**, 137–151 (2000).

[93] G. Gröbner, G. Choi, I. Burnett, P. Verdegem, J. Lugtenburg, C. Glaubitz and A. Watts, *Biophys. J.* **72**, TUAM3–TUAM3 Part (1997).

[94] G. Gröbner, I. Burnett, C. Glaubitz, J. Mason and A. Watts, *Biophys. J.* **74**, A249 Part 2 (1998).

[95] G. Gröbner, I. J. Burnett, C. Glaubitz, G. Choi, A. J. Mason and A. Watts, *Nature* **405**, 810–813 (2000).

[96] X. Feng, P. J. E. Verdegem, Y. K. Lee, D. Sandström, M. Edén, P. Bovee-Geurts, W. J. de Grip, J. Lugtenburg, H. J. M. de Groot and M. H. Levitt, *J. Am. Chem. Soc.* **119**, 6853–6857 (1997).

[97] X. Feng, P. J. E. Verdegem, M. Eden, D. Sandström, Y. K. Lee, P. H. M Bovee-Geurts, W. J. de Grip, J. Lugtenburg, H. J. M. de Groot and M. H. Levitt, *J. Biomol. NMR* **16**, 1–8 (2000).

[98] J. C. Lansing, M. Hohwy, C. P. Jaroniec, A. F. L. Creemers, J. Lugtenburg, J. Herzfeld and R. G. Griffin, *Biochem.* **41**, 431 (2002).

[99] B. Alberts, D. Bray, A. Johnson, J. Lewis, M. Raff, K. Roberts and P. Walter, *Essential cell biology*, Garland Publishing, Inc. (New York & London), (1997).

[100] T. Okada, Y. Fujiyoshi, M. Silow, J. Navarro, E. M. Landau and Y. Shichida, *Proc. Nat. Acad. Sci. USA* **99**, 5982–5987 (2002).

[101] R. W. Schoenlein, L. A. Peteanu, R. A. Mathies and C. V. Shank, *Science* **254**, 412 (1991).

[102] L. Stryer, *Sci. Amer.* **257**, 42 (1987).

[103] R. W. Rodieck, *The first steps in seeing*, Sinauer Associates, Inc., (1998).

[104] R. Hubbard, P. K. Brown and A. Kropf, *Nature* **183**, 442 (1959).

[105] G. Wald, *Science* **162**, 230 (1968).

[106] J. E. Kim, D. W. McCamant, L. Zhu and R. A. Mathies, *J. Phys. Chem. B* **105**, 1240–1249 (2001).

[107] D. Pan, Z. Ganim, J. E. Kim, M. A. Verhoeven, J. Lugtenburg and R. A. Mathies, *J. Am. Chem. Soc.* **124**, 4857–4864 (2002).

[108] T. Yoshizawa and G. Wald, *Nature* **4874**, 1279 (1963).

[109] T. Hamanaka, T. Mitsui, T. Ashida and M. Kakudo, *Acta Cryst. B* **28**, 214–222 (1972).

[110] R. D. Gilardi, I. L. Karle and J. Karle, *Acta Cryst. B* **28**, 2605–2612 (1972).

[111] B. D. Santarsiero, M. N. G. James, M. Mahendran and R. F. Childs, *J. Am. Chem. Soc.* **112**, 9416–9418 (1990).

[112] G. R. Elia, R. F. Childs, J. F. Britten, D. S. C. Yang and B. D. Santarsiero, *Can. J. Chem.* **74**, 591–601 (1996).

[113] K. Palczewski, T. Kumasaka, T. Hori, C. A. Behnke, H. Motoshima, B. A. Fox, I. Le Trong, D. C. Teller, T. Okada, R. E. Stenkamp, M. Yamamoto and M. Miyano, *Science* **289**, 739–745 (2000).

[114] K. Palczewski, T. Kumasaka, T. Hori, C. A. Behnke, H. Motoshima, B. A. Fox, I. Le Trong, D. C. Teller, T. Okada, R. E. Stenkamp, M. Yamamoto and M. Miyano, *Biophys. J.* **80**, 1465 (2001).

[115] M. Garavelli, F. Negri and M. Olivucci, *J. Am. Chem. Soc.* **121**, 1023–1029 (1999).

[116] I. Palings, J. A. Pardoen, E. Van den Berg, C. Winkel, J. Lugtenburg and R. A. Mathies, *Biochem.* **26**, 2544–2556 (1987).

[117] S. W. Lin, M. Groesbeek, I. van der Hoef, P. Verdegem, J. Lugtenburg and R. A. Mathies, *J. Phys. Chem. B* **102**, 2787–2806 (1998).

[118] G. G. Kochendoerfer, P. J. E. Verdegem, I. van der Hoef ad J. Lugtenburg and R. A. Mathies, *Biochem.* **35**, 16230 (1996).

[119] S. O. Smith, I. Palings, V. Copie, D. P. Raleigh, J. Courtin, J. A. Pardoen, J. Lugtenburg, R. A. Mathies and R. G. Griffin, *Biochem.* **26**, 1606 (1987).

[120] S. O. Smith, I. Palings, M. E. Miley, J. Courtin, H. De Groot, J. Lugtenburg, R. A. Mathies and R. G. Griffin, *Biochem.* **29**, 8158 (1990).

[121] S. O. Smith, J. Courtin, H. De Groot, R. Gebhard and J. Lugtenburg, *Biochem.* **30**, 7409 (1991).

[122] M. Han and S. O. Smith, *Biochem.* **34**, 1425–1432 (1995).

[123] M. Han, B. S. DeDecker and S. O. Smith, *Biophys. J.* **65**, 899 (1993).

[124] A. F. L. Creemers, C. H. W. Klaassen, P. H. M. Bovee-Geurts, R. Kelle, U. Kragl, J. Raap, W. J. de Grip and J. Lugtenburgand H. J. M. de Groot, *Biochem.* **38**, 7195–7199 (1999).

[125] M. Eilers, P. J. Reeves, W. Ying, H. G. Khorana and S. O. Smith, *Proc. Natl. Acad. Sci., USA* **96**, 487 (1999).

[126] G. Gröbner, I. Burnett, C. Glaubitz, J. Mason and A. Watts, *FEBS Lett.* **422**, 201 (1998).

[127] M. A. Verhoeven, A. F. L. Creemers, P. H. M. Bovee-Geurts, W. J. de Grip, J. Lugtenburg and H. J. M. de Groot, *Biochem.* **40**, 3282–3288 (2001).

[128] A. F. L. Creemers, S. Kiihne, P. H. M. Bovee-Geurts, W. J. De Grip, J. Lugtenburg and H. J. M. de Groot, *Proc. Natl. Acad. Sci.* **99**, 9101–9106 (2002).

[129] F. Buda, P. Giannozzi and F. Mauri, *J. Phys. Chem. B* **104**, 9048–9053 (2000).

[130] F. Buda, H. J. M. de Groot and A. Bifone, *Phys. Rev. Lett.* **77**, 4474–4477 (1996).

[131] M. Sugihara, P. Entel, H. Meyer, V. Buss and J. Hafner, *Prog. Theor. Phys. Suppl.* **138**, 107 (2000).

[132] M. Sugihara, P. Entel and V. Buss, *Phase Transit.* **75**, 11 (2002).

[133] P. Entel, M. Sugihara, V. Buss, M. Elstner and T. Frauenheim, *Proceedings of the Second International Conference on Computational Nanoscience and Nanotechnology* 77 (2002).

[134] M. Groesbeek and J. Lugtenburg, *J. Photochem. Photobiol.* **56**, 903–908 (1992).

[135] W. J. de Grip, F. J. M. Daemen and S. L. Bonting, *Methods in Enzym.* **67**, 301–320 (1980).

[136] J. F. Haw, R. A. Crook and R. C. Crosby, *J. Magn. Reson.* **66**, 551 (1986).

[137] A. Bielecki and D. P. Burum, *J. Magn. Reson. A* **116**, 215–220 (1995).

[138] G. Neue and C. Dybowski, *Solid State NMR* **7**, 333–336 (1997).

[139] P. A. Beckmann and C. Dybowski, *J. Magn. Reson.* **146**, 379–380 (2000).

[140] O. N. Antzutkin, Y. K. Lee and M. H. Levitt, *J. Magn. Reson.* **135**, 144–155 (1998).

[141] H. Geen, J. J. Titman, J. Gottwald and H. W. Spiess, *Chem. Phys. Lett.* **227**, 79–86 (1994).

[142] I. Schnell, A. Lupulescu, S. Hafner, D. E. Demco and H. W. Spiess, *J. Magn. Reson.* **133**, 61–69 (1998).

[143] M. Schneider, L. Gasper, D. E. Demco and B. Bl umich, *J. Chem. Phys.* **111**, 402–415 (1999).

[144] I. Schnell and H. W. Spiess, *J. Magn. Reson.* **151**, 153–227 (2001).

[145] O. N. Antzutkin and R. Tycko, *J. Chem. Phys.* **110**, 2749–2752 (1999).

[146] O. N. Antzutkin, J. J. Balbach, R. D. Leapman, N. W. Rizzo, J. Reed and R. Tycko, *Proc. Natl. Acad. Sci.* **97**, 13045–13050 (2000).

[147] D. Suter, S. B. Liu, J. Baum and A. Pines, *Chem. Phys.* **114**, 103–109 (1987).

[148] H. Geen, R. Graf, A. S. D. Heindrichs, B. S. Hickman, I. Schnell, H. W. Spiess and J. J. Titman, *J. Magn. Reson.* **138**, 167–172 (1999).

[149] J. Baum and A. Pines, *J. Am. Chem. Soc.* **108**, 7447–7454 (1986).

[150] M. Edén, A. Brinkmann, H. Luthman, L. Eriksson and M. H. Levitt, *J. Magn. Reson.* **144**, 266–279 (2000).

[151] N. Oyler and R. Tycko, *J. Phys. Chem. B* **106**, 8382–8389 (2002).

[152] S. Vega, *J. Chem. Phys.* **68**, 5518–5527 (1978).

Appendix C

Included Papers

Paper I

Symmetry Principles for the Design of Radiofrequency Pulse Sequences in the Nuclear Magnetic Resonance of Rotating Solids,

M. Carravetta, M. Edén, A. Brinkmann, X. Zhao and M. H. Levitt

Chem. Phys. Lett. **321**, 205 (2000)

Paper II

Estimation of Carbon-Carbon Bond Lengths and Medium-Range Internuclear Distances by Solid-State Nuclear Magnetic Resonance

M. Carravetta, M. Edén, O. G. Johannessen, H. Luthman, P. J. E. Verdegem, J. Lugtenburg, A. Sebald and M. H. Levitt

J. Am. Chem. Soc. **123**, 10628 (2001)

Paper III

Towards dipolar recoupling in macroscopically oriented samples of membrane proteins rotating at the magic angle

C. Glaubitz, **M. Carravetta**, M. Edén and M. H. Levitt

in "Perspectives on Solid State NMR in Biology",

S. Kiihne and H. J. M. de Groot, eds., Kluwer, Dordrecht, The Netherlands, pages 83-92 (2001).

Paper IV

Enhanced Triple-Quantum Excitation in Solid-State MAS NMR

M. Carravetta, J. Schmedt auf der Günne and M. H. Levitt

Submitted to *J. Magn. Res.*

Paper V

Rhodopsin draft on distances

M. Carravetta, X. Zhao, S. Kiihne, M. Verhoeven, P. J. E. Verdegem, H. Luthman, P. Bovee-Geurts, J. Lugtenburg, H. J. M. de Groot and M. H. Levitt

in manuscript